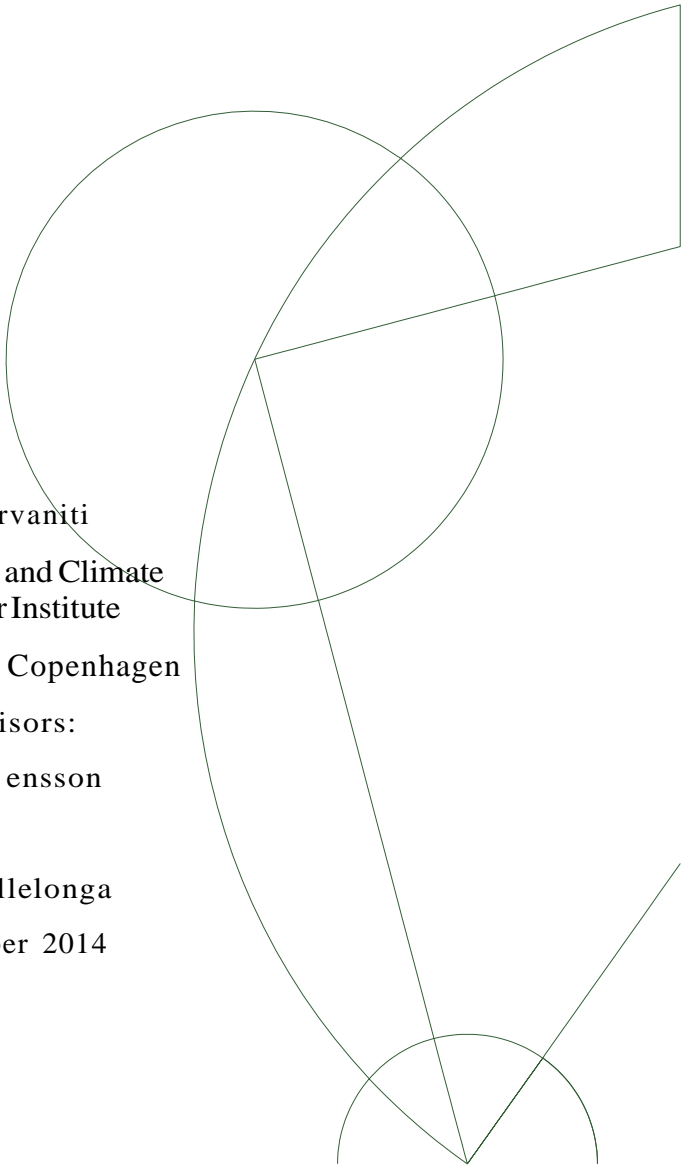




Master's thesis in Physics

Application of Contactless Conductivity Detection to Ice Core Analysis



Maria Arvaniti
Centre for Ice and Climate
Niels Bohr Institute
University of Copenhagen

Supervisors:
Anders Svensson

&

Paul Vallelonga

December 2014

Master's Thesis

Title: Application of contactless conductivity detection to ice core analysis

ECTS-points: 60

Supervisors: Anders Svensson & Paul Vallelonga

Name of department: Centre for Ice and Climate
Niels Bohr Institute
University of Copenhagen

Signature:

Author:

Submitted:

Maria Arvaniti

December, 2014

Abstract

Ice cores enclose a variety climate proxies that are extremely valuable for understanding the past climate of our planet. These proxies include trace gases, salts, dust, stable isotopes and acids. Salts, dust and acids can originate from many different sources, and each one of them indicates a certain atmospheric and environmental condition. Continuous Flow Analysis (CFA) is a method of measuring these chemical impurities by analyzing the meltwater that derives from melting a certain piece cut from the ice core. The CFA system includes a dust detector, for measuring the dust that is incorporated into the ice, the absorption and fluorescence detective methods that measure the concentration of certain ionic species and a conductivity meter that measures the conductivity of the meltwater, which is the bulk of its ionic constituents.

In this project, the EDAQ C4D conductivity detector was tested for discrete and continuous measurements of conductivity standards in the range of the conductivity values typically found in the ice cores. The output of the instrument is voltage, which depends on the frequency of the input AC voltage. For discrete measurements the response of the instrument is dominated by a high peak matching with the 859kHz frequency and a broad maximum, whose location in the frequency range depends on the value of conductivity measured, and the type of tube used. The wide range maximum lies in the interval 8-48kHz and shifts towards the lower frequencies as the value of conductivity decreases. For continuous measurements the instrument is set to measure in the frequency, which gives a linear relation between the voltage output and the conductivity value of the standard. This is found to be $f = 19219\text{Hz}$ for clear PFA tube of I.D. = 0.03''.

Then the EDAQ C4D system was applied to analyze the conductivity of the shallow South Dome ice core from Greenland. The results are compared with the Model Series 380, a standard instrument for electrical conductivity detection, and with other detection methods of the CFA system as well. The comparison of the measurements of the two instruments, EDAQ C4D and Model 382 Series showed that there is a linear relation of high correlation, between them for the certain voltage interval of 0.1V to 0.5V. This upper limit is apparent in the discrete measurements too. Moreover the EDAQ C4D exhibits a faster response in conductivity changes.

The dust and conductivity profiles obtained from the shallow South Dome ice core are compared to the dust and conductivity profiles of the upper part of the NEGIS shallow ice core. Conductivity and dust lie within a certain range respectively, however there are some notable differences that could be due attributed to the different precipitation rates of the geographical areas of origination for the two ice cores.

Acknowledgement

I want to thank first of all my supervisors Anders Svensson and Paul Vallelonga for teaching me and supporting me during this last year of my studying. I feel that I have learned a lot; doing a master thesis is certainly a unique experience, and my supervisors' teaching and talks, have really helped me to progress. I would also like to thank Helle Kjær for discussing with me in the lab. Then I would like to thank Yongbiao Weng and Iben Koldtoft for proofreading, and for the good times we had together while studying at CIC. Finally I want to thank everyone who works or studies at CIC, for our nice discussions and the nice working environment.

Table of Contents

Chapter 1 Introduction	1
Chapter 2 Background Theory	5
2.1 Ice Core Archives.....	5
2.1.1 How ice sheets are formed	6
2.1.2 Dating the Ice Cores	8
2.1.3 Water Stable Isotopes	8
2.2 Ice Core Impurities	10
2.2.1 Sea Salt	10
2.2.2 Continental dust	12
2.2.3 Biogenic Emissions	14
2.2.4 Anthropogenic Emissions	16
2.2.5 Volcanic Emissions	17
2.2.6 Conductivity in ice cores	19
Chapter 3 Materials and Methods	
3.1 Continuous Flow Analysis	21
3.2 Essential Constituents of the CFA System.....	21
3.3 Detection methods for CFA system	24
3.4 Conductivity in Solutions	27
3.4.1 Measuring the Conductivity of a Solution	28
3.4.2 Conductivity Detection Methods used in this thesis	29
3.4.2.1 Capacitively Coupled Contactless Conductivity Detection	30
3.4.2.1.1 The Functioning Principle	30
3.4.2.1.2 The capacitively-coupled contactless conductivity detection system	33
3.4.2.1.3 The ER225 C4D Data System.....	36

3.4.2.2 Conductivity meter Model 3082 Series	37
3.5 Testing the EDAQ C4D	39
3.6 Cutting the Ice Core.....	41
Chapter 4 Results	45
4.1 Testing the C4D ER225 System.....	45
4.1.1 The Voltage Response.....	45
4.1.2 Sample and Reference Circuit.....	47
4.1.3 Testing different tubes	
4.1.4 Frequency Response.....	55
4.1.4 Time Resolution	57
4.2 Measuring Conductivity – South Dome Data	60
Chapter 5 Discussion	65
5.1 Operation of the EDAQ C4D instrument	65
5.2 Comparison of the two instruments	67
5.3 Comparison of the EDAQ C4D data with data of other detection methods of the CFA system.....	69
5.4 Comparison of the South Dome and NEGIS Shallow Ice Cores	74
Chapter 6 Conclusions and Outlook	79
6.1 Conclusions	79
6.2 Future Work	80
References	82

Chapter 1 Introduction

The Earth's climate is a complex system that has a great impact on the life of humans. This is one of the reasons we are so eager to understand and describe it. Its beauty and complexity triggers our native curiosity. The past climate of the Earth has been very different from the present, and the future climate will possibly be much different as well. Internal mechanisms of the Earth-Atmosphere system along with external mechanisms that affect it, have an impact on the climate of our planet, shifting it from old to new equilibrium states, from cold to warm and vice versa.

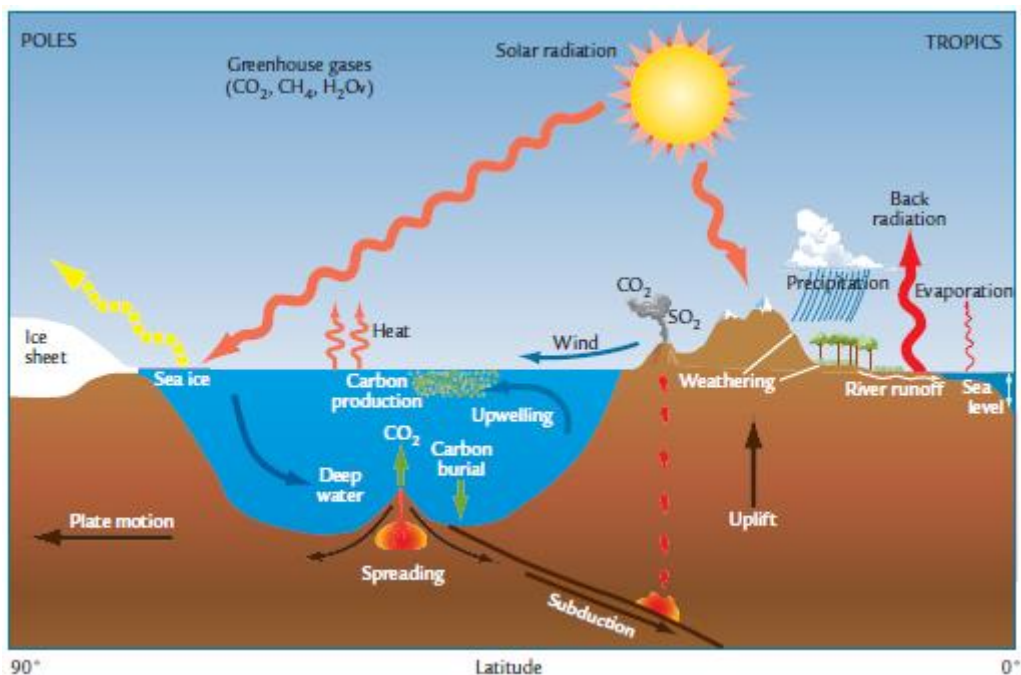


Figure 1.1 The complexity of the climate system (Ruddiman, 2008)

Air, water, land, ice, vegetation, ocean and processes such as evaporation, wind, precipitation, radiation absorbance and emission, are the major components of the climate system. Changes in plate tectonics, in the Sun's strength and in the Earth's orbit can alter the complicated interactions between the components of the climate system and shift it from its previous state. The system responds with internal variations in the interactions between the atmosphere, ocean, ice, vegetation and land surface that redistribute the energy and in the long term shift it to a new equilibrium state.

Some of these changes occur in cycles, like the changes in the Earth's orbit, which alter the amount of solar radiation that reaches the Earth's atmosphere and surface, and thus decrease or increase the temperature respectively. Milankovitch (1920), first proposed that an orbital configuration with low summer insolation in the Northern Hemisphere, triggers the initiation of a glacial period, with continental sized ice sheets building up gradually; as the low summer insolation reduces the warmth and rate of melting during the summer season, allowing the snow to accumulate and the ice sheets to grow. Conversely, in an orbital configuration in favor of strong summer insolation in the Northern Hemisphere, temperature increases, accelerating the melting and shrinking of the ice sheets. Milankovitch theory explains certain cycles of the ice sheet grow and retreat, but cannot explain all the cycles (Ruddiman, 2008). This indicates the complexity of the climate system, as other factors and their interactions may have postponed or accelerated the formation of the ice sheets in the past.

As our instrumental records extend back no more than approximately 150 years, and are extremely limited in their spatial cover, researchers have found ways to extract climatic data from natural sources in order to reconstruct past climates. Climate archives are natural records that contain information about Earth's past climate. Some of these sources include ice cores, ocean and lake sediments, tree rings, corals and others. The technological bloom of the last decades allowed scientists to perform extremely sensitive measurements on them, and examine the recorded history of the past climate. The major climate archives are sediments, ice, corals, and trees. Sediment archives date further back in time, up to hundreds of millions of years, whereas tree rings date back up to few hundred years (Ruddiman, 2008).

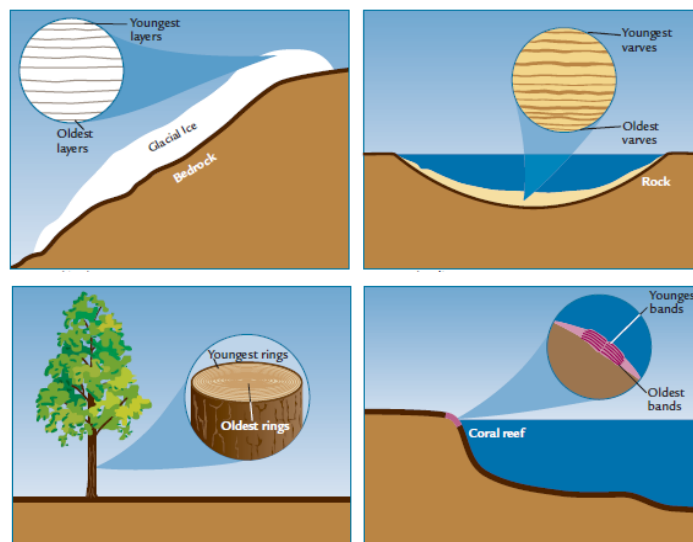


Figure 1.2 Climate archives (Ruddiman, 2008)

Sediments are created when wind, precipitation etc erode rocks exposed on the surface of the planet. The eroded debris is transported in streams and rivers to lakes and oceans, where it is finally deposited at the bottom, producing a succession of layers. Likewise, fine grains from distant dust storms, ash from volcanoes, and pollen can be blown over water, sink to the bottom, and join the deposition process. Organic materials from creatures living within the water also fell down to join the sediment layers. Sediments delivered to the seafloor may be preserved for tens of millions of years until the tectonic processes finally destroys them.

Trees can be also used as climate proxies because trees produce annual layers called tree rings. These rings are alternations between thick layers of lighter wood tissue formed by rapid growth in spring; and thin, dark layers marking cessation of growth in autumn and winter. Their width depends on climate conditions and especially on precipitation. Trees usually live up to tens hundreds of years.

In tropical oceans, corals record seasonal changes in calcite (CaCO_3), which is incorporated in their skeletons creating bands of darker and lighter color. The lighter parts of the coral bands are laid down in summer, during intervals of fast growth, while the darker layers are laid down during winter. Paleoclimate reconstructions from corals generally rely on geochemical characteristics of the coral skeleton such as variations in trace elements or stable isotopes. (Ruddiman, 2008)

Glaciers and ice sheets are formed in areas with very low temperatures; when layers of snow that fell during winter season, do not melt in summer, pile up, and gradually build big masses of snow and ice. Ice sheets are continental sized layered formations of ice, whereas glaciers are smaller ice formations usually deposited on mountains. The annual layers of ice contain a variety of information relevant to the composition and prevailing climatic conditions of the atmosphere at the time they were formed. Ice sheets and glaciers provide high resolution climatic reconstructions, which make them particularly precious for studying the past climate of our planet.

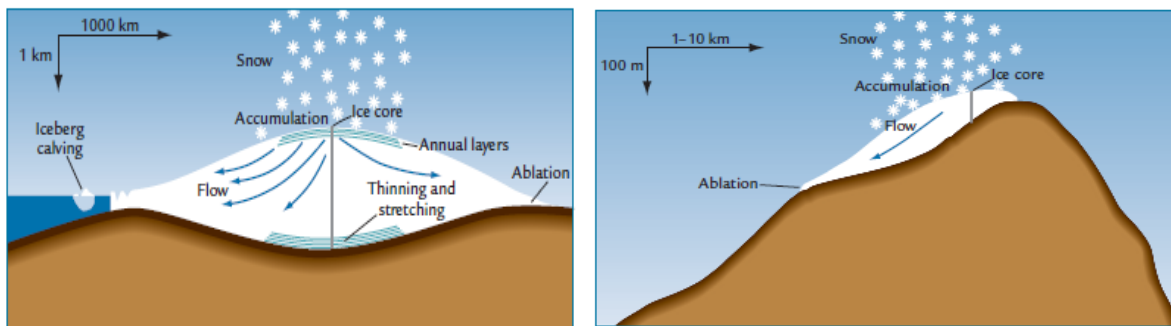


Figure 1.3 Ice archives; Ice sheet on the left and glacier on the right side (Ruddiman, 2008).

Chapter 2 Background Theory

2.1 Ice Core Archives

An ice core sample is typically removed from an ice sheet or a glacier. In polar regions, the Antarctic and Greenland ice sheets contain 99% of the Earth's glacial ice, while high mountain ranges in high, mid and low latitudes contain approximately 1% (Post and LaChapelle, 2000). In Figure 2.1, a several meters long ice core is presented, from the North Greenland Eemian Ice Drilling (NEEM).



Figure 2.1 Several meters long ice core from NEEM (Kenji Kawamura, NEEM ice core drilling project, <http://www.neem.ku.dk>)

Climate information is obtained in a great extent by ice cores. Inclusions like dust and ash from volcanic eruptions are deposited over the ice during snowfall. Common climate indicators are stable isotopes, the content of salts and acids, and traces gases such as CH_4 and CO_2 (IPCC, 2013). They are proxies of temperature, chemistry and gas composition of the lower atmosphere, of volcanic eruptions, wind direction, forest fires etc.

The main advantage of the ice cores is that they provide a detailed record (Boutron et al., 1995), of multiple variables from the same physical location. The main disadvantage of ice core data is

that they are mostly present in the poles and high mountains, and thus provide few information about mid and low-latitudes.

2.1.1 How ice sheets are formed

An ice sheet begins to form when temperature is below 0°C and the high precipitation that falls remains in the same area and accumulates over many years, often centuries. As year after year new snow falls in the region, an ice record of climate and environmental conditions is created. At first, snow falls on the ice surface and gradually, under the weight of new layers, it turns into firn and finally into ice.

The transformation of snow begins if the accumulated snow survives one summer season. This year-old snow forms a denser, more compressed layer called firn. The density of firn at the surface is approximately 350kgm⁻³. As density increases with depth, ice crystals change their shape and size, as molecules are moving both within the ice lattice and over the crystal surface; the net direction of movement of molecules is in the direction where the surface area and free energy tend to a minimum. In this way firn grains become denser. As density increases further, firn becomes less porous, and the area of contact between crystals is increasing. Recrystallization and deformation become the dominant processes: molecular diffusion changes the shape and size of crystals in such a way as to reduce the stresses on them. The area of contact between ice crystals is increasing, and when the density reaches about 830kgm⁻³ the air spaces between crystals close off, and firn becomes ice. The remainder air that did not escape to the surface is now present only as bubbles (Cuffey and Patterson; 2010).

Although ice cores contain a variety of information, their interpretation is not trivial, because an ice sheet is not a static formation – but a dynamic one - that evolves with time. Hence, the layers of the ice are moving from the accumulation to the ablation zone due to the mass imbalance between these two areas. This imbalance increases the shear stress on the ice sheet until it begins to flow. The flow is mostly affected by the slope of the ice, the ice thickness and temperature. The topography of the bedrock may affect the flow as well, causing it to fold and to mix layers of different depth and thus of different age. Additionally, there are many factors that may affect the flow. Such factors can be the basal melting, that depends on the rate of geothermal heat flux of the bedrock, the thickness of annual layers, the physical properties and impurity content of the ice and others.

Moreover, the new layers that are formed compress the layers underneath them. The pressure of the layers above them and the stretching due to the motion of the ice sheet make the deeper layers turn thinner and thinner as the depth increases. This results in the decreasing of resolution of an ice core with depth. The time resolution of the shortest time period which can be distinguished depends on the amount of annual snowfall, and reduces with depth as the ice compacts under the

weight of new layers accumulating on top. Deeper into the ice, the layers thin further and annual layers become indistinguishable.

Other factors that affect the body of the ice sheet - and hence the ice core extracted from it - are the climate conditions. During ice ages, the ice sheets expand, whereas during the interglacial retreat. This changes the position of the accumulation and ablation zones with time, and alters the ice flow regime. Finding the spot to drill an ice core with the least disturbed ice is very important because an ice core will be used to reconstruct a detailed climate record extending over hundreds of thousands of years, providing information on a wide variety of aspects of climate at each point in time.

Ice divide is the ideal place for ice core extraction because it is the area where ice does not flow horizontally. If there is not horizontal flow, all the ice at depth is formed from the same location at surface. In Fig 2.2 the statement of ice in the surface and its movement downward is shown. In the vertical direction the layer is thinner and in horizontal direction is extended. This extension is the result of horizontal motion according to distance from the divide.

Radar measurements are used to find and follow layers in the ice and for investigating bed features. Further flow models are used in the process of finding the best position for the desired resolution and time span. (Kjær, 2010).

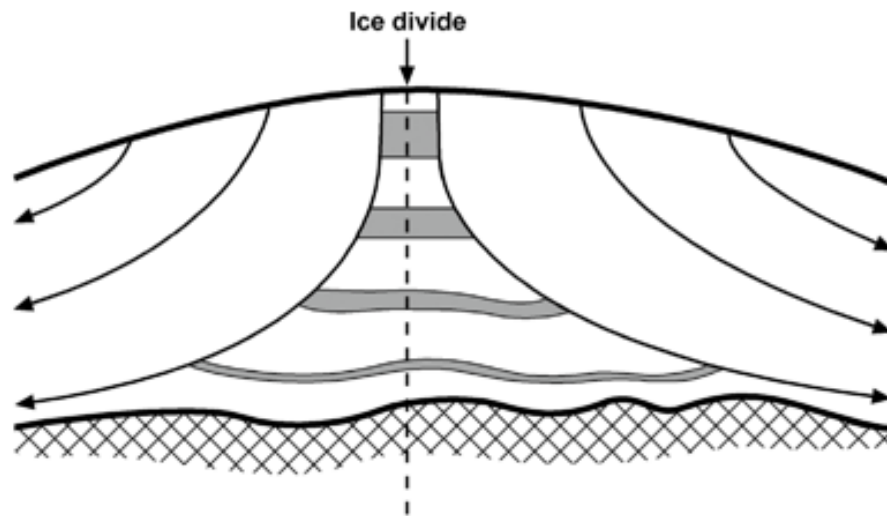


Figure 2.2 Schematic cross section through an ice divide with flow paths (Cuffey and Patterson, 2010)

The first ice cores were drilled in Antarctica and Greenland because in these regions ice sheets present large size and thickness and the ice is not disturbed. Long cores are possibly extracted due to their thickness and their age is calculated at approximately 100ka and 800ka years for Greenland and Antarctica respectively (IPCC, 2013).

2.1.2 Dating the Ice Cores

Dating an ice core is a significant aspect of the past climate reconstruction, as it allows us to compare the climate signal to other cores or other climate archives such as sediment cores or tree rings.

If the annual layers are still distinguishable, then we can date the ice core by annual layer counting and each depositional event can be clearly seen as a distinct layer. Moreover, summer and winter snow can sometimes be distinguished by a melt layer. However, as the snow is transformed into ice, the annual layer thickness decreases and the annual stratification becomes obscure. To distinguish the layers, analysis of the core is needed.

Measurements of annual signals such as $\delta^{18}\text{O}$, electrical conductivity, dust and variations in the concentration of chemical species are performed to count the annual layers. However, as layers get thinner and thinner with depth, time resolution diminishes further, and confirmation is required. Notable acid or ash layers coming from massive volcanic eruptions of known age, or even ice flow computer models can be used for this purpose.

In regions with little precipitation such as the inland region of Antarctica, the method of detecting annual signals is not very effective; and the dating methods applied are flow computer models and atmospheric gases with known long lifetimes, such as methane, diatomic oxygen and argon (Paterson and Cuffey, 2010).

2.1.3 Water Stable Isotopes

In the field of paleoclimatology, a very important tool for reconstructing the past climates are the stable isotopes of water, which can be found in a variety of climate archives, such as ice cores, corals, tree rings, oceanic and lake sediments, and others. The isotopes of oxygen are the ^{16}O , ^{17}O , and ^{18}O , with ^{16}O being the most abundant of three, having 99.76% of total, while the heavier ^{17}O and ^{18}O have a small percentage of 0.04% and 0.2% respectively. Hydrogen has two isotopes, the ^1H and ^2H (deuterium); likewise the lighter isotope is the most abundant with a percentage of 99.984%, while the other has an abundance of 0.016% (Bradley, 2014). In general only three isotopes of water molecules are significant and used in paleoclimatology: H_2^{16}O , H_2^{18}O and HD^{16}O , with relative abundances in marine water of 0.9977:0.0020:0.0003 (Cuffey and Patterson, 2010).

This fraction between the lighter and the heavier water isotopes and especially between the concentration of ^{18}O and ^{16}O in a water sample is given by the $\delta^{18}\text{O}$ value:

$$\delta^{18}\text{O} = \left(\frac{\left(\frac{^{18}\text{O}}{^{16}\text{O}} \right)_{\text{sample}}}{\left(\frac{^{18}\text{O}}{^{16}\text{O}} \right)_{\text{SMOW}}} - 1 \right) * 10^3 \text{‰}$$

where SMOW stands for Standard Mean Ocean Water which has a known isotopic composition. The more negative the $\delta^{18}\text{O}$, the more the depletion of the ^{18}O from the water sample. On a global scale the atmospheric circulation moves water from subtropical oceans to poles; the cooling of the air mass drives condensation and precipitation of the water vapor, which further depletes it from the heavy isotopes along its path. Therefore $\delta^{18}\text{O}$ values decline at higher latitudes as a consequence of the fractionation procedure (Bradley, 2014).

The greater fall in temperature, the more condensation will occur and the lower will be the heavy isotope concentration, relative to the original water source but the depletion depends on both the height above the sea level and how far to the north the ice core is placed. The water vapor that reaches the poles is isotopically lighter than the primary subtropical source; thus the snow that it forms carries the signal onto the ice sheet when it is deposited. This signal mainly depends on the condensation temperature, and as the climate turns colder, the ice sheet contains less heavy isotopes (more negative $\delta^{18}\text{O}$ value). Other factors can influence the isotopic composition, but as they tend to fluctuate together, the isotopes maintain the strong correlation with temperature. This strong correlation of the $\delta^{18}\text{O}$ value to temperature, gives a good picture of the past climate. (Dansgaard, 1964).

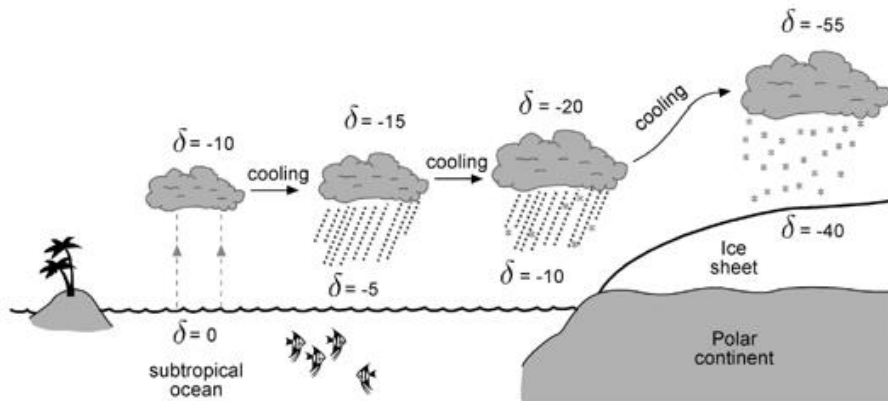


Figure 2.3 The value of $\delta^{18}\text{O}$ decreases as water mass moves towards polar regions (Cuffey and Patterson, 2010).

2.2 Ice Core Impurities

Substances held inside the falling precipitation are accumulated into the ice sheets, thus produce a long-term record of atmospheric conditions inside the ice. By studying these substances we can better understand the past climate.

2.2.1 Sea Salt

Many aerosols, especially those containing Na^+ , Mg^{2+} , Cl^- , Ca^{2+} and SO_4^{-2} originate from sea salts, with the most important being the Na^+ (Cuffey and Patterson, 2010). Sea salt aerosols are among the major sources of impurities in polar ice cores (Kreutz and Koffman, 2010). Sea salt aerosols coming to coastal and mainland areas, are mainly produced when small water bubbles from wave crests come out into the atmosphere and create aerosol particles by drying. The ion species that are connected with sea salt usually reach maximum concentration in winter time, as we may notice in Figure 2.4, which shows the result of a snow/firn study in an area located 2600m east of the NEEM drilling site. The vertical profile of sodium exhibits seasonal variations and peaks in winter to early spring (Kuramoto, et al; 2011). Moreover, sea salt aerosols exhibit high concentrations in the glacial periods too. During the glacial periods, the sea ice is in great extent and the access of aerosols produced above sea regions into mainland and coastal areas cannot be as easy as during the interglacials. Their high depositional concentrations indicate increased

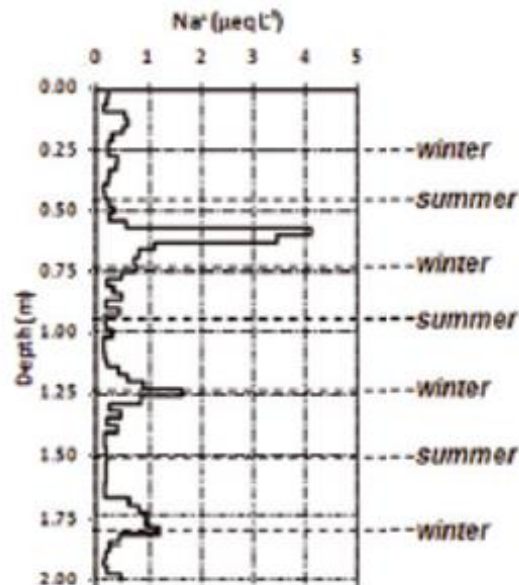


Figure 2.4 Depth profile for sodium (Kuramoto, 2011)

storminess over the ocean that enhances their transport inland during glacial periods and winter. Additionally, on newly formed sea ice a brine layer accumulates on its top surface and is scattered in various ways (Cuffey and Patterson, 2010).

In sea salt records from Greenland, notable concentration increases during glacial periods are observed. In the high elevation regions of the low-latitude mainland, sea salt aerosol concentration depends on how far the ice core site is located from the ocean (Kreutz K.J. and Koffman, 2010). Figure 2.5 depicts the time variation of marine originated sodium ($ssNa^+$) and dust originated calcium ($nssCa^{+2}$) for the last 110ka from the GISP2 ice core. The last glacial period lasted from approximately 110ka to 12ka, and in Figure 2.5 during this period both ionic concentrations are notably higher than during the warm contemporary period (Holocene) that follows the last glacial (Mayewski et al.; 1997).

As mentioned above Na^+ , Mg^{+2} , Cl^- , Ca^{+2} and SO_4^{-2} are the major contributors of the marine aerosols, with Na^+ being the most important. However, Na^+ can have a crustal origin too. Additionally, Ca^{+2} usually originates from the continents and only some Ca^{+2} concentrations emanate from the ocean (Fischer et al; 2007). Therefore, it is important to distinguish between the sea-salt (ss) and non-sea salt (nss) impurity constituents (Kreutz K.J. and Koffman, 2010), especially in ice core sites like the East Antarctic plateau, where the seawater contribution to Ca^{+2} can be quite important during the Holocene (around 50%) (Fischer et al; 2007).

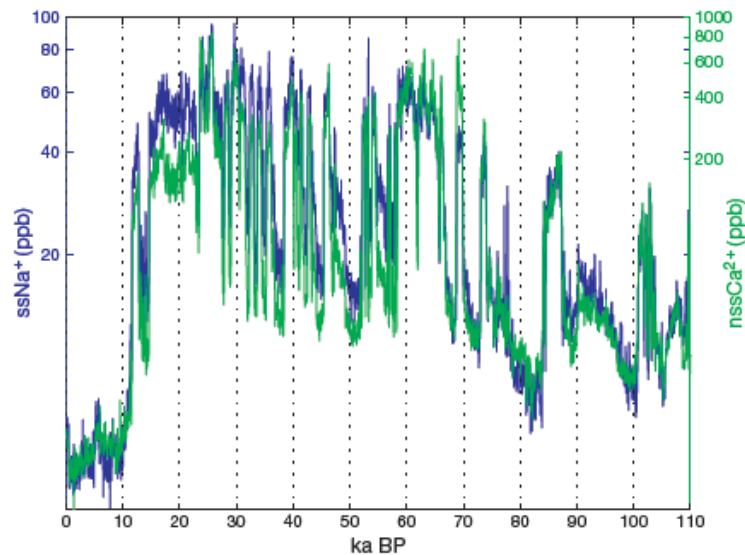


Figure 2.5 Time series of marine originated sodium and dust for the 110ka (Mayewski et al.; 1997).

One simple calculation for the non-sea salt Ca^{+2} constituent and the sea-salt Na^+ constituent would be:

$$nssCa^{2+} = \frac{R_t}{R_t - R_m} (Ca^{2+} - R_m Na^+)$$

$$ssNa^+ = Na^+ - \frac{1}{R_t - R_m} (Ca^{2+} - R_m Na^+)$$

Where R_m is the Ca^{+2}/Na^+ seawater ratio, and is equal to 0.038. R_t is the crustal ratio and is approximately equal to 1.78 depending on the composition of the crust (Fischer et al; 2007).

2.2.2 Continental Dust

Chemical and physical weathering of the crust surface generate dust microparticles that high surface winds may carry into the atmosphere (Fischer et al; 2007). Larger particles may enter the troposphere by both strong wind and colliding with other particles, a process that is called saltation (Fischer et al; 2007). Generally the composition of the dust particles reflects the types of rocks found on continents. The continental dust is a considerable constituent of the climate system because it acts as a cloud condensation nuclei and it also scatters and absorbs the incoming solar radiation. (Kreutz and Koffman, 2010). At present the primary dust source regions of the atmosphere in the Northern Hemisphere, are the Sahara Desert, the deserts in the Middle East, in central and eastern Asia and the desert in the United States (Svensson and Biscaye, 2000). The most significant dust sources for Greenland today are the deserts in Asia and in particular the Taklamakan and the Gobi desert. Their high-altitude position, enhances the rise of dust into the troposphere, while the dominant west wind enhances the dust transportation to Greenland (Svensson and Biscaye, 2000). In the Southern Hemisphere the main source of dust in Antarctica is South America and specifically, for Eastern Antarctica the region of Patagonia (Lunt and Valdes, 2001). At the glacial periods the concentrations dust in the atmosphere are raised significantly. Many factors could contribute to that, as the prevailing climate circumstances increase the atmospheric aridity which in turn intensifies surface dryness and therefore increases the extension of deserts and dry areas. Moreover the dust source areas increase further by erosion caused by glaciers. During the last glacial period the 120 m sea level decrease, exposed extensive continental self-areas that were added to the dust sources as well (Svensson et al., 2000). The amount of the mineral dust in the atmosphere is greatly affected by the climate conditions in the region of origin, and therefore dust records give information on wind speeds, cyclonic activity, vegetation cover and soil properties (Lunt and Valdes, 2001). The source of the greatest amount of nss Ca^{+2} in ice cores is continental dust and all of the non-sea salt part of Mg^{+2} , Na^+ , K^+ , SO_4^{-2} , NO_3^- , and Cl^- are correlated to minerals which originate from continents (Kreutz and Koffman, 2010). In the Figure

2.6, $\delta^{18}\text{O}$ and insoluble dust concentration profiles from GRIP are anticorrelated. The last glacial period was interrupted from warm episodes called Dansgaard-Oeschger events where the $\delta^{18}\text{O}$ signal increases and dust decreases. In the Last Glacial Maximum (LGM), the $\delta^{18}\text{O}$ signal reaches its minimum and dust its maximum. In the figure 2.7, the calcium profile for the firn core from NEEM site mentioned in the previous section is shown. There is a seasonal variation for calcium, which peaks during spring. The sea-salt concentrations are small and the main source for calcium is mineral dust (Kuramoto et al., 2011).

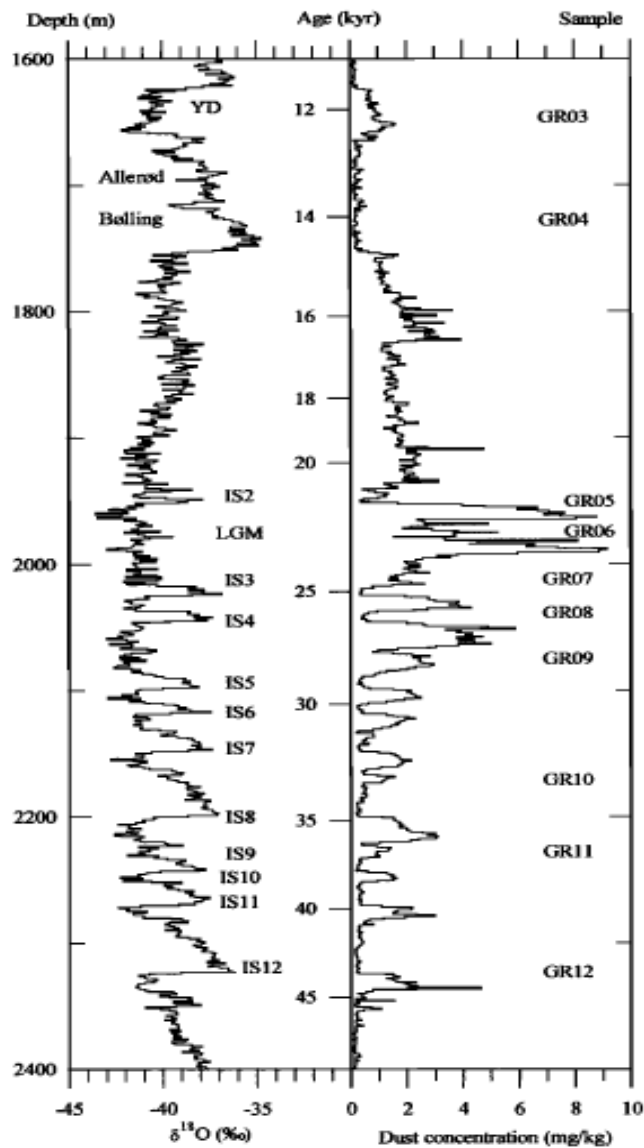


Fig 2.6 The $\delta^{18}\text{O}$ and insoluble dust concentration profile from GRIP; LCM, YD and Dansgaard-Oeschger events (IS) are indicated (Svensson and Biscaye, 2000).

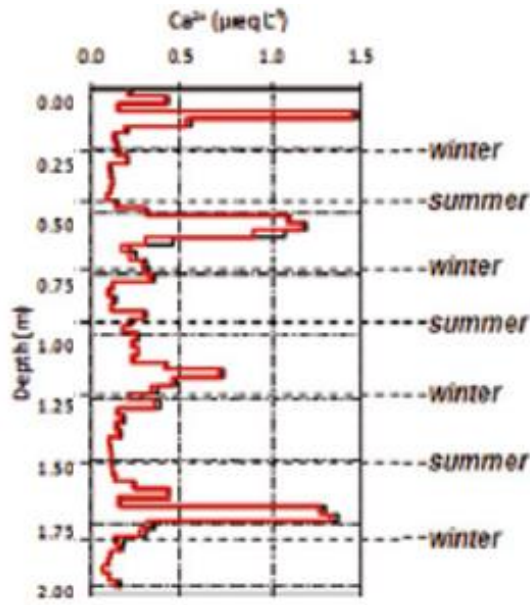


Figure 2.7: Depth profile for calcium, black and red curves indicate total concentrations and non-sea-salt concentrations respectively (Kuramoto et al., 2011).

2.2.3 Biogenic Emissions

Biogenic emissions have an important role in the atmospheric SO_4^{2-} cycle, as one of the major nss SO_4^{2-} sources is the oxidation of dimethylsulfide (DMS), a gas emitted from phytoplankton. (Kreutz and Koffman, 2010). Phytoplankton emits DMS, which by oxidation produces methanesulphonate acid (MSA) and SO_2 . This system has a potential effect on climate, as stratus clouds nucleate on H_2SO_4 aerosols. Thus, a rise in oceanic gas production might increase cloud coverage and reflection of the solar insolation (Cuffey and Patterson, 2010). Estimation of both in ice cores is necessary to distinguish sulfur biogenic sources from nonbiogenic sources, given that both exist as submicron aerosols and should have similar atmospheric transport and deposition processes. Such measurements from the Vostok ice core exhibit an increase of the oceanic productivity during the last LGM, possibly due to low temperatures. Moreover correlations have been found to the sea ice extent, indicating algal production within and on the top of the sea ice.

Another important secondary aerosol for paleoclimate research is ammonium NH_4^+ , which derives from the interaction of atmospheric sulfate with ammonia (Fuhrer et al., 1996). Ammonia emissions originate from several biogenic emissions such as deforestation, fires, agriculture, including animal husbandry and NH_3 -based fertilizer applications. Other sources of NH_3 include industrial processes, and volatilization from soils and oceans (Sailesh et al., 2013). In the high-latitude northern hemisphere, ice core NH_4^+ concentrations have been used to reconstruct boreal

forest fires; additionally, GISP2 NH_4^+ concentrations indicate that there is an orbital control of continental ammonium emission over the past 110ka (Figure 2.8) (Kreutz and Koffman, 2010).

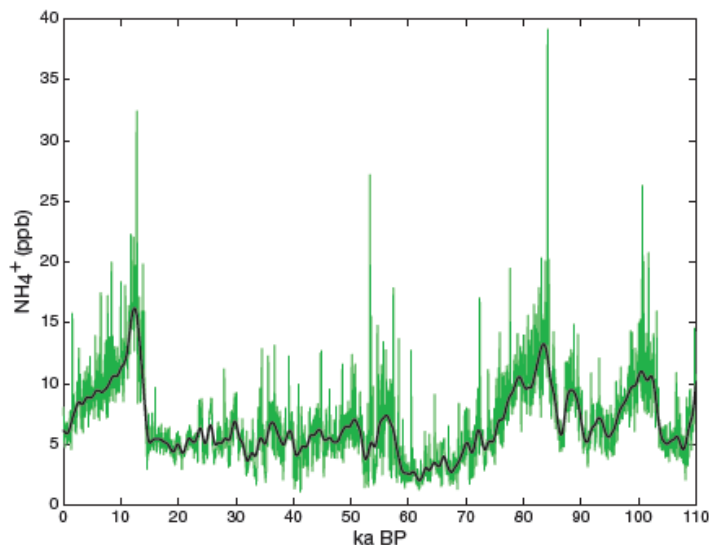


Figure 2.8 NH_4^+ concentration for the last 110ka from the GISP2 ice core (Mayewski et al., 1997).

NO_3^- is another important secondary aerosol, and its concentration has been estimated in ice cores as a proxy for past changes in atmospheric NO_x (NO and NO_2) concentrations (Kreutz and Koffman, 2010). It has several minor sources of production. In the higher atmosphere the main source of NO_3 is stratospheric oxidation of N_2O , ionospheric dissociation of N_2 and production by lightning (Bertler et al.; 2005). In the lower troposphere NO_3^- is produced mainly by biomass burning and biogenic soil emissions (Bertler, et al; 2005), which are suggested to be the main sources of summer peaks at NEEM and other sites in the Arctic, whereas winter-to-early spring peaks of NO_3^- at NEEM are suggested to be of anthropogenic origin (Kuramoto et al.; 2011).

Studies have shown that post depositional changes (temperature and accumulation rate) and changes in atmospheric chemistry (Kreutz and Koffman, 2010), and photochemical mechanisms can lead to NO_3^- decrease concentrations in ice cores, especially in the concentration of the first upper meters of the snowpack (Bertler et al.; 2005).

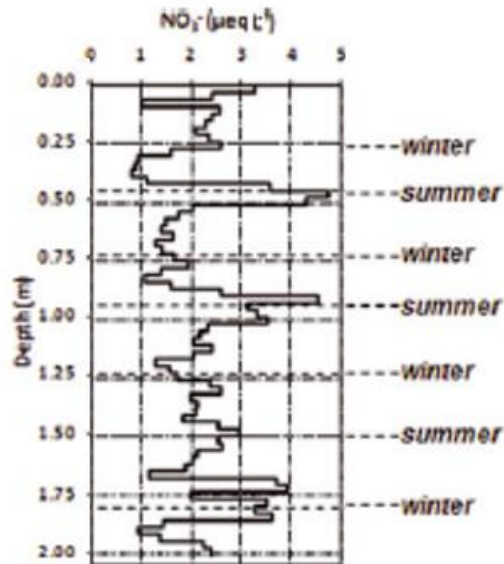


Figure 2.9 Depth profile for NO_3^- (Kuramoto et al., 2011).

2.2.4 Anthropogenic Emissions

The industrial revolution of the 19th century was a radical transition from hand production methods to machines, whose emissions added greenhouse gases and aerosols into the atmosphere.

Emissions of SO_2 and NO_x , originating from industrial processes and fossil fuel combustion, form a source for the secondary SO_4^{2-} and NO_3^- atmospheric aerosols. Their presence has been recorded in the ice core records from Greenland, the Canadian Arctic, Svalbard, and the European Alps (Kreutz and Koffman, 2010). So far, there is no strong proof for anthropogenic SO_4^{2-} or NO_3^- emissions in Antarctica (Kreutz and Koffman, 2010).

Specifically, NO_3^- has an annual variation that peaks from winter to spring and in summer, as recorded in NEEM and other ice cores from the Arctic. The source of the winter to spring peak appears to be anthropogenic from fossil fuel combustion, while the summer peak is primary of natural origin (Kuramoto et al., 2011). Similarly, SO_4^{2-} and also nssSO_4^{2-} peak in winter to spring has been recorded from ice cores in Greenland and the Canadian Arctic, whose origin appears to be anthropogenic air pollutants, although a winter to early spring peak of the aerosol in pre-industrial and modern snow at NEEM imply that in north Greenland SO_4^{2-} could have both natural and anthropogenic origin (Kuramoto et al., 2011).

Another aerosol whose concentration increased after the industrial revolution is black carbon. The black carbon absorbs the incoming solar radiation contributing to global warming and its

deposition changes the albedo of ice surfaces, thus accelerating their melting. Measurements between Vanillic acid, an indicator of the forest fires, and black carbon from ice cores in central Greenland propose that forest fires were the primary origin of BC in Greenland before 1850. After 1850, annual BC concentrations started a progressive increase (McConell et al.; 2007). According to air-mass back-trajectory modeling, most of the industrial BC deposited in central Greenland most likely came from North American emissions, while since 1951 Asia may be the primary source.

2.2.5 Volcanic Emissions

Volcanic eruptions inject various kinds of particles and gases into different heights of the atmosphere depending on the intensity of the eruption and the composition of the ejecta (Kreutz and Koffman, 2010). The fundamental constituent of a volcanic eruption is the magmatic material that either comes out as solid matter or when injected into the atmosphere turns into big solid particles called ash or tephra. The particles that are emitted into the troposphere, form a tropospheric aerosol cloud that regionally acts as an obstacle to the shortwave solar radiation, while emitting longwave infra-red (IR) radiation. This aerosol layer cools the surface during day and heats it during night, reducing the diurnal cycle. However the aerosols that form it fall to the surface fairly quickly, and thus the cloud is dispelled within few days.

Furthermore, the eruption emits important greenhouse gases like CO₂ and H₂O, which are already abundant in the atmosphere, and therefore the emission of a single volcanic eruption does not have an important long-term impact on the greenhouse effect; however if some SO₄²⁻ particles manage to reach the stratosphere, they can stay there from few months to 2-3 years resulting in a global impact on climate (Robock, 2000). The most important climate impact may be from gas emissions, mostly in the form of SO₂ and H₂S. Sulfur emissions react with OH⁻ and H₂O and form small H₂SO₄ aerosols. The aerosol cloud that they produce spreads out into the stratosphere according to the dominant stratospheric wind pattern (Robock, 2000). It is transferred from regional to global distances, and finally is deposited on the surface of the Earth including glaciers and ice sheets (Kreutz and Koffman, 2010). As the sulfate aerosol size is of the same order as visible solar radiation, and their single scatter albedo is of the order of 1, they strongly interact and scatter solar insolation. This reflecting effect decreases the amount of solar radiation that reaches the surface of the Earth (Robock, 2000). The aerosol cloud absorbs and emits solar radiation near the infrared (IR). The emission cools the cloud, whereas the absorption of radiation from above warms it up. The previously mentioned procedure dominates over the cooling inside the cloud. On the contrary, in the troposphere, the radiative influence of the cloud is minor as the extra IR radiation from the cloud offsets the decreased direct downward IR flux (Robock, 2000). Another possible outcome of the increased aerosol presence, is enhanced cirrus cloud formation.

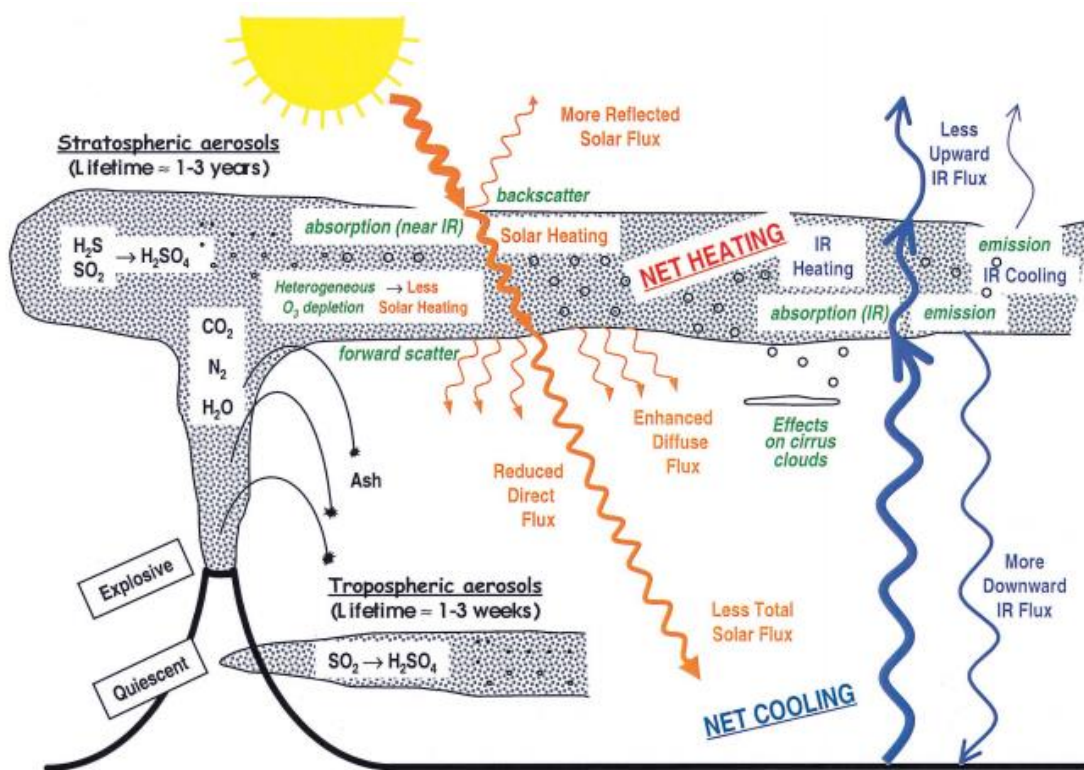


Figure 2.10 Volcanic inputs and their effects (Robock, 2000).

However, on the surface the net result of the cloud is net cooling, as the added downward diffuse shortwave flux and the additional downward IR cannot balance the big reduction in direct shortwave radiation (Robock, 2000). The duration of the stratospheric aerosol cloud is usually 1-3 years and the blockage of the incoming solar radiation moderates the summer in the tropics and in the midlatitudes, while warming up the NH winter over continents. The stratospheric heating is more intense in the tropics than in the poles, and this temperature gradient sets up advective effects that overwhelm the radiative; heating up the NH continental regions (Robock, 2000). Finally, the sulfur aerosols contribute to the depletion of the ozone layer as their presence facilitates chemical reactions on their surfaces that destroy ozone.

Tephra and sulfate aerosols are transferred regionally or globally, and deposited on glaciers and ice sheets which retain a proxy of the past volcanic activity of the planet. These records can be used to evaluate the atmospheric aerosol load coming from an eruption and the possible climate impact. The record of the volcanic activity, can be also used to estimate the amount of climate forcing in climate models and to date the ice cores (Abbot and Davies, 2012). These layers have an absolute age, if the calendar age of the eruption is known. Such eruptions include Tambora in Indonesia, 1815, and Laki in Iceland, 1783 and others (Abbot and Davies, 2012).

The Greenland ice sheet keeps a record of volcanic aerosols for the past 123ka, which can be interpreted by implementing methods such as ECM and the measurement of sulphate (SO_4^{2-}) concentrations in ice. The ECM (electrical conductivity method) signal responds to acidity ice, which depends on the deposition of the acidic volcanic aerosols on the ice sheet. Clear acidity peaks are connected to past volcanic eruptions.

Furthermore, volcanic eruptions can be detected through the measurement of the sulphate (SO_4^{2-}) concentrations in the ice, which is the component of the hydrogen sulphate (H_2SO_4) aerosols deposited on the ice sheet, and conductivity. A high resolution method for the detection of sulphate and other chemical species, and conductivity, is the continuous flow analysis (CFA) system (Sigg et al., 1994, Rothlisberger et al., 2000, Kaufmann et al., 2008). Both ECM and sulphate detection can be used to date ice core records (Rasmussen et al., 2013, Svensson et al., 2008).

2.2.6 Conductivity in Ice Cores

There are two theories that describe the electrical properties of the ice, the Jaccard theory and the Grain Boundary Conduction; however, none of them describes completely the electrical properties of the ice.

Jaccard Theory

Jaccard theory describes how conduction occurs in ice. The ice lattice possesses a regular crystalline structure. Any deviation from the periodical structure around a single lattice point is called a defect and occurs when atoms are displaced from their crystal structure sites. A displacement is caused by thermally activated processes, or by the presence of impurities. The defect point is a “vacancy” that moves through the crystal structure, taking the place of the adjacent atom that jumps into it.

In the ice lattice, there are two groups of point defects: ionic defects (H_3O^+ and OH^-) and L^- and D^- defects. The ionic defects are H_2O ionized molecules. The OH^- defects are believed to be uncommon in polar ice, and H_3O^+ defects are extrinsic defects of H^+ ions from dissociated acids. When a hydrogen bond has two or no H^+ connected with it, it is a D^- defect or a L^- defect respectively.

The conductivity σ_i caused by these defect types is the product of the defect's volumetric concentration n_i , of the effective charge e_i and of the mobility μ_i , which depends on temperature and concentration (Stillman et al., 2013):

$$\sigma_i = n_i \mu_i |e_i|$$

The subscript i refers to the type of defect. According to Jaccard theory L- defects and D-defects are the most important carriers for high frequencies and ionic defects for low frequencies (dc conductivity) (Wolff et al., 1997).

Grain Boundary Conduction

This theory suggests that conductivity takes place through a network of liquid veins connected in triple junctions on the grain boundaries (Wolff et al., 1997), and is based on observations of acid anions in triple junctions and veins. However the presence of cation acids was not clarified during these studies (Stillman et al., 2013). According to this theory, dc conductivity takes place at boundaries and high frequency conductivity is a grain boundary process as well (Wolff et.al., 1997).

The conductivity of an ice core is a measure of the total dissolved ionic content in a melted sample (Gow, 1968). Conductivity is measured continuously in the high resolution Continuous Flow Analysis system, along with other ionic species, such as sodium and calcium. As mentioned in the previous paragraphs, the concentration of these species exhibits annual cycles that can be detected through the high resolution analysis of the CFA system, which can typically analyze an ice core to centimeters (Svensson et al., 2013). These annual cycles can be used for annual layer counting, and therefore to date the ice core.

Furthermore, conductivity increases when acids typically deposited by volcanic eruptions are present in the melted ice sample. Therefore, volcanic eruptions can be identified by measuring and comparing conductivity with sulfate, and other methods of measuring conductivity on ice, such as ECM. The date of a volcanic eruption can be known from historical records and therefore the specific layer that included the signal can be matched with this date. Moreover, the annual layers between two volcanic eruptions can be counted based on other ionic constituents measured by the CFA system (Svensson et al., 2008, 2013, Andersen et al., 2006)

Chapter 3 Materials and Methods

3.1 Continuous Flow Analysis

Ice cores are paleoclimate archives including low concentration chemical impurities that signify the past climate of the period they were formed. The faint climatic signal requires careful handling of the cores, methods that minimize the risk of contamination, and methods of maintaining the trace-level (ppb, ppt) concentrations of impurities (Breton et al., 2012). Continuous flow analysis (CFA) systems give an important reduction of sample handling work in addition to very high spatial resolution, which is the fundamental advantage of the method in comparison with conventional methods (Sigg, et al., 1994). Continuous Flow Analysis systems were evolved by Sigg and others during the 1990s (Breton et al., 2012).

3.2 Essential Constituents of the CFA System

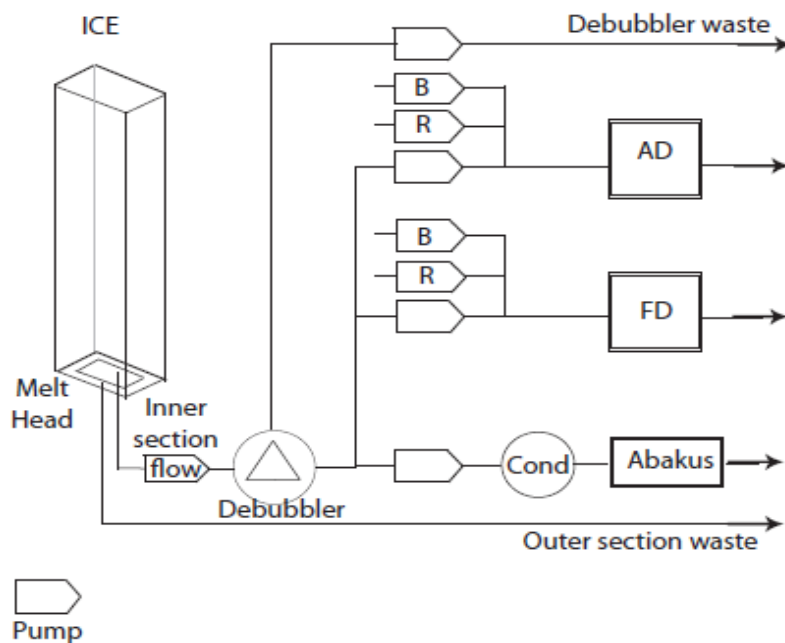


Figure 3.1 A schematic overview of the Continuous Flow Analysis system. The sample flow runs through the debubbler and then into the separate detection branches of absorption (AD), fluorescence (FD) detection and non-destructive methods of dust and conductivity detection. (Kjær, 2010)

The ice core, which is typically 55cm long, is placed vertically inside the melting unit, and over a heated melthead. A continuous and steady sample stream is maintained by continuous melting on a steady rate, of a subsection of the ice core, over the melting device (Bigler et al., 2011). A peristaltic pump drains off the flow and leads into the system the inner and uncontaminated part of it, while the outer and possibly contaminated flow is led to waste (Breton et al., 2012). The inner flow passes through the dedubbler, where ancient air trapped into the ice is removed from it. Then three different lines lead the sample through different detection methods of the system. For conductivity detection, one or more conductivity detection instruments are placed on a separate line. Fluorescence and absorption methods adapted from flow injection analysis (FIA), are mainly used for the detection of separate ion constituents and pH measurements of the flow (Bigler et al., 2011). There can be different types of instruments used in a CFA system, however we will focus on those used at the Copenhagen CFA System, which is the measurement system used for this thesis.

The melting unit, where the ice core is continuously melted, is placed inside the cold environment of a vertical freezer at a temperature of -20°C . The core sample is held by a removable rectangular plexiglass container that keeps it fixed above the melthead while its length is decreasing.

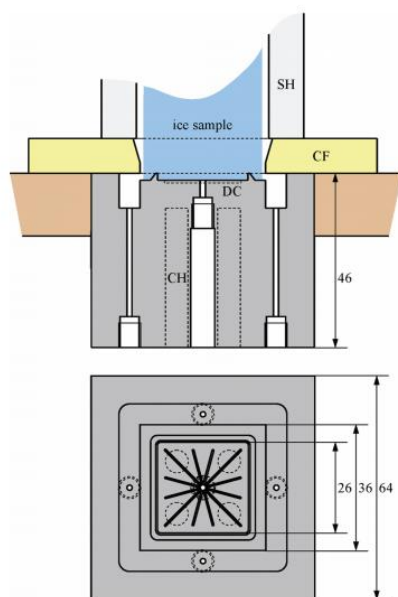


Figure 3.2 a) Cross section of the melting device, DC: melting device and holes, CH cartridge heaters, CH: centering frame, SH: removable plexiglass sample holder. b) The melting device seen from above - dimensions in mm (Bigler et al., 2011).

A stainless steel cylinder inside it, applies a constant downward force on the ice core sample, ensuring a stable melting rate. At the back of the holder and parallel to the sample, a draw wire position transducer records the depth during melting (Bigler et al., 2011).

The melthead is consisted of an inner and outer squared surfaces that are divided by a 2mm high triangular ridge. The drain channels inside the inner area guide the melted sample towards the

single central drainage point, and to the tube which lays underneath the melthead, and which leads it into the system for analysis. The ridge between the two surfaces separates the inner and uncontaminated part of the flow from the outer and possibly contaminated part, which is removed by four drainage points on the outer surface. The design of the melthead minimizes the mixing of the flow while its cooper body enhances the transfer of the heat produced by four heating cartridges. The temperature is kept stable at 30°C by a temperature regulator device. In this way the system ensures a constant melting rate.

At the surface of the melthead there is a thin layer of chemically inert gold, above a slightly thicker electroless nickel layer. Both layers provide a chemically inert surface with good thermal conductivity. The melting rate of the system is 9ml/min while only 8ml/min is pumped into the drainage point of the inner surface. The overflow from the inner to the outer part is created in order to prevent contamination between the two parts (Kaufmann et al., 2008, Bigler et al., 2011). The melt progress is registered by an optical encoder (Baumer Electric) connected to a weight lying upon the ice sample, which applies additional pressure to maintain a uniform melting speed also toward the end of a measurement (Kaufmann et al., 2008).

The sample meltwater is transferred through the system by a peristaltic pump at a rate adjusted to the melting speed (Kaufmann et al., 2008). Next in line comes an automated 6-port injection valve that determines whether sample meltwater, ultrapure blank water, or standard solutions flow through the measuring units. A supplementary is used to sustain pumping from the melthead when standards are imported into the system (Bigler et al., 2011). Next in series comes the debubbler that separates the air from inside the meltwater. The ice core sample naturally includes air bubbles that constitute approximately 10% of its volume.

The debubbler divides the air from the water flow, preventing it to enter into the system and cause inaccurate measurements (Kaufmann et al., 2008) The debubbler used for the experiments in this thesis consists of a closed triangular cell with one inlet and two outlets. It is made of PEEK and it is closed by a transparent FEP lid. The inlet is for the debubbled meltwater and the outlets are for the air separated from it and for the excess meltwater. The shape and dimensions of the cell are chosen for the best possible separation of the air and water sample. An overflow of approximately 2ml/min includes the air that we want to separate from the sample. A sample flow of approximately 8ml/min only 6ml/min is used for analysis through the system.

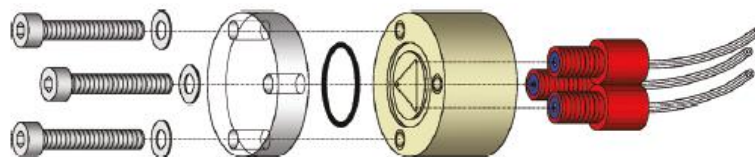


Figure 3.3: The debubbler with the characteristic triangular cell (Bigler et al., 2011).

3.3 Detection methods for CFA system

Following the separation of water and gas sample at the debubbler, the melted water is directed into various analytical systems and is split further into different lines for each measuring units, and different climate proxies get analyzed (Kjær, 2014). Fluorescence and absorption methods are widely used for detecting the various chemical species (ions) incorporated inside the water sample while dust and conductivity measurements are non-destructive methods that are used for measuring the dust content and the bulk of ions contained into the sample. Furthermore, recent developments allow measurements of water isotopes, methane, and carbon dioxide (Kjær, 2014).

Absorption Detection Method

The concentration of ion species such as Na^+ , Ca^{2+} , SO_4^{2-} , NO_3^- can be measured by the absorption detection method, where the unknown concentration of the chemical species is calculated by the absorption of light (Kjær, 2014). After the sample water is pumped through the detection line, it is mixed with the appropriate reagent and buffer and then is guided through the detection cell, inside a light path of length l , where it absorbs part of the emitted light.

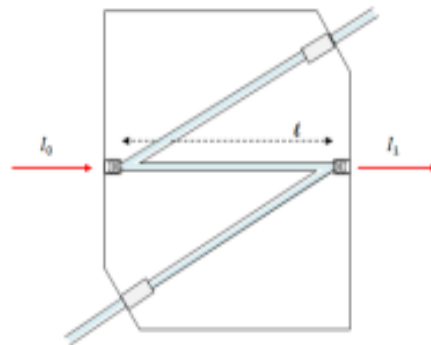


Figure 3.4 A beam of light of intensity I_0 goes through the flow cell of length l while the transmitted light has an intensity of I_1 (Nielsen, 2009).

The Beer-Lambert law connects the absorbance of light to the concentration of the absorbent substance.

$$A = \log_{10} \left(\frac{I_0}{I_1} \right) \epsilon l c \quad (3.1)$$

The law expresses the relation between the absorption of light through a substance (water sample), the absorptivity of the attenuator, ϵ , the concentration of the attenuating species, c , and the distance the light travels through the substance l . I_1 and I_0 are the intensity of the light before and after the absorption respectively, l is the path length, c is the molar concentration of the attenuating species and ϵ is the molar absorptivity of the attenuator. The absorption can be estimated as the difference between the detected light in a sample with the chemical species we want to define and a sample of ultrapure blank water, while the ϵl constituent can be calculated by standards of known concentration. The Beer Lambert law is linear and the relation collapses in high concentrations, above 0.01M (Kjær, 2014).

Fluorescence Detection Method

The concentration of ion species such as Ca^{2+} , NH_4^+ and H_2O_2 can be determined by the fluorescence detection method. The sample water passes through the fluorescence detection line, and initially, it is mixed with the proper reagent and buffer. Afterwards, it passes through the light path of the detection cell, where the photosensor elements are placed vertically to a LED light source. A molecule of the chemical species absorbs photons and it is excited into a higher energy state. Then the molecule emits photons of less or equal energy to the one absorbed, and decays to ground state. As the emitted photons have less or equal energy, light of a longer wave length than the excitation beam is emitted. The emission intensity is often recorded by an optical filter, and since the concentration behaves linearly in response to intensity, the higher concentration, the more photons will be emitted and therefore a greater intensity is measured.

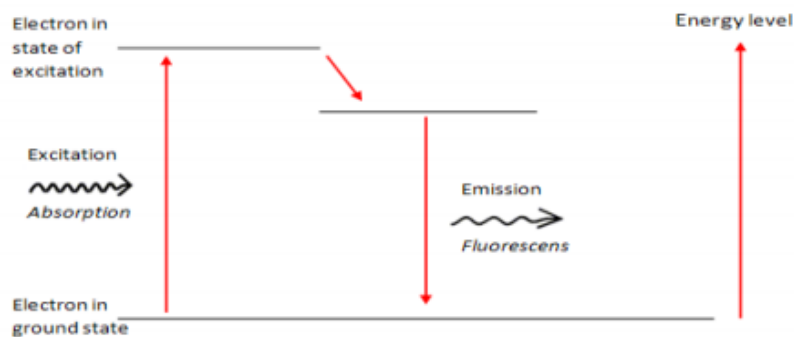


Figure 3.5 Excitation and decay of an electron (Nielsen, 2009).

Dust detector

In addition to measurements of chemical species, a particle detector (Abakus with sensor type LDS-23/25bs sensor, Klotz) is used for measuring insoluble dust particles and their magnitude.

The sample water passes through the detection cell, where a laser beam of 670nm wavelength falls on it. The particle attenuates the propagating light by shadowing and scattering, depending on its shape, volume, material and orientation. Thus the photo diode detector measures a negative peak. The peak is classified by height into 32 channels, which correspond to different size intervals (Ruth et al., 2002) The particle size channels can be calibrated with spherical latex particles, however, mineral dust particles come in all shapes, therefore only the total dust particle number can be calculated quantitatively (Lambert et al., 2012).

The lower particle detection limit is approximately $0.8\mu\text{m}$ of spherical equivalent diameter, however the lower limit of $1\mu\text{m}$ ensures particle detection above the detector noise level (Ruth et al., 2002). The upper measuring limit is customarily determined to $15\mu\text{m}$ (Lambert et al., 2012). Within this interval the number of particles is counted. The Abakus is functioning in series with a liquid flow meter (ASL-1600-20, Sensorion) that measures the flow rate (by conveying the results from particles/sec into particles/cm), particle size and concentrations.

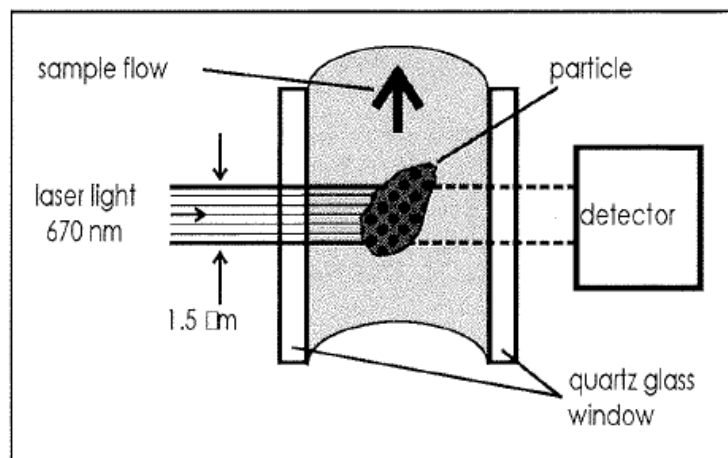


Figure 3.6 Dust detector: A particle goes through the cell and scatters the laser beam, shutting the signal to the detector (Ruth et al., 2002).

3.4 Conductivity in Solutions

The conductivity of a solution is a measure of its capacity to conduct electricity. The ions contained into such a solution, are formed when an electrolyte dissolves into the solvent of the solution. An electrolyte is a substance that ionizes when dissolved into an appropriate solvent such as water. Electrolytes include bases, acids, soluble salts, and specific gases like carbon dioxide, ammonia and hydrogen chloride (Gray, 2004). Water is the solvent in many electrolyte solutions, because water molecules are polarized. When an ionic or polar compound enters the water, the relatively small water molecules circle each molecule of the compound, and the positively charged part of the water dipole pulls the negatively charged ion of the compound; and conversely for the negatively charged ions. In that way the water molecules carry away into the solution the charged molecules of the solute and a solution that conducts electricity is produced (Bagotsky, 2005). Thus, the higher the dissolved ionic concentration, the higher the conductivity of the solution will be:

$$\sigma = \sum ne\mu$$

where σ is the conductivity, n is the number of ion carrier, e is electric charge, and μ is mobility of carrier ions (Ohmo, 2005).

The mobility of the ion carrier or electrophoretic mobility for a particular ion is a constant that specifies how it moves in a solution, when an external electric field is applied. Two forces are applied to a molecule of charge q , the electric force and the frictional force. At steady state they balance out, and for this state the electrophoretic mobility is defined as:

$$\mu = \frac{q}{6\pi\eta r v}$$

where η is the viscosity of the solution, r the radius of the ion (assumed to be spherical), and v the velocity of the ion. The charge to radius ratio (q/r) is constant for a certain ion species and characterizes how quickly it will move in a solution when an external electric field is applied. Ionic species with big charge to radius ratio move faster than ionic species with small charge to radius ratio (Stojkovic, 2013).

The conductivity of the solution also depends on the temperature and on the ionic concentration of the solute. The mobility of ions increases with the rise of temperature and so does the conductivity of the solution. Nevertheless, the change in conductivity with temperature is

determined by the concentration, type of the electrolyte and the range of conductivity in the solution (Gray, 2004).

The concentration of the dissolved ions of the solute, affects the conductivity of the solution as well. However, the connection is not always linear. For very dilute solutions with conductivity of $10\mu\text{S}/\text{cm}$ or less, the ions behave independently, and the conductivity of the solution is linearly dependent on their concentration. For solutions of greater conductivity, the ion-ion interactions become important. With increasing their concentration, the conductivity response of the solution deviates from linearity. For some electrolytes, there is even a saturation point of maximum conductivity, and if crossed, there is a decrease in conductivity with increasing the ionic concentration. Thus the determination of the solute concentration from measuring the conductivity cannot be accomplished knowing only the conductivity, especially in a concentrated solution with a mixture of electrolytes, whose total electric behavior is affected by their interactions and is different from the conductivity each one of them exhibits in a pure solution. To define concentration with a conductivity measurement, additional information about the solution must be obtained. Additionally, conductivity is not specific, meaning that measurements alone cannot define a specific type of electrolyte in the solution. As conductivity is a measure of the electric current that can be carried through the solution, and is only indicative of the presence of ions. Finally, solutions of non-electrolytes have no conductivity because they do not contain ions nor produce them when dissolved within a solvent (Gray, 2004, Bagotsky, 2005).

3.4.1 Measuring the Conductivity of a Solution

Since the conductivity of a solution is defined as its ability to conduct electricity, it may be measured by applying a voltage between two different points of the solution, via two electrodes which are separated by a constant distance. Throughout this procedure, the anions move towards the positive electrode while the cations move towards the negative electrode, and the solution acts as an electrical conductor.

According to Ohm's law an electrical current (i) that passes through two electrodes, is proportional to the potential difference (V) between the electrodes, and inversely proportional to the opposition that it meets during its movement (R), or resistance. The resistance of a material, is constant for a steady temperature.

$$i = \frac{V}{R}$$

The electrical conductance (G), is the reciprocal of electrical resistance. Thus it describes how easily the electric current passes between the two electrodes of the conductor.

$$G = \frac{1}{R}$$

The conductance (G) of the solution, depends on the geometry of the electrodes, and is proportional to their area (S) and inversely proportional to the distance (l) between the electrodes:

$$G = \sigma \frac{S}{l}$$

Where σ is the conductivity of the solution, which also measures, how easily an electric current passes through the conductor. It can be defined by measuring the resistance. It is a constant property of the material for a given temperature.

$$\sigma = \frac{l}{SR}$$

The ratio l/S describes the geometry of the electrodes, and it is also known as the cell constant of the detection instrument. The SI unit for conductivity is $S\text{cm}^{-1}$. However, it should be noticed that these formulas describe only qualitatively the system, as they assume a uniform electric current flow between the electrodes, something that cannot always be achieved, especially when the conductor is consisted of a variety of different ions. Moreover, they assume a DC voltage, while in conductivity detection of aquatic solutions an AC is generally applied. An alternating AC voltage is characterized by both amplitude and frequency and it also causes the skin effect; an effect that hinders the current flow near the center of the conductor altering the geometry of the system and thus, the resistance (Caloz, 2011, Alonso and Finn, 1969)

3.4.2 Conductivity Detection Methods Used in This Thesis

Additional to the previously mentioned CFA methods, there are two conductivity detectors included in the system, the EDAQ C4D and the Model 3082 Series. Both of them are connected in the same branch of the system, measuring the conductivity separately.

3.4.2.1 Capacitively Coupled Contactless Conductivity Detection

3.4.2.1.1 The Functioning Principle

The functioning principle of the method is based on the measurement of the electric current, produced when an alternating current (AC) voltage is applied to the detection cell. The detection cell is consisted of two electrodes that are divided by a gap of several mm. Among the electrodes, a capillary is placed that carries the sample solution to the detection cell. The two electrodes are placed cylindrically around the capillary wall and are thus isolated from the sample since there is no direct contact between them. The electric current is applied longitudinally, hence lengthwise the capillary (Zeeman, 2003). The applied to the electrodes voltage, causes an accumulation of ions near the electrode surfaces, and thus, a polarization resistance arises, which may lead to erroneous results, as it is a parasitic resistance of the circuit that alters the solution resistance. The polarization effects can be reduced by applying an alternating current. Then the ions will tend to flow through the circuit, and not to concentrate near the electrode surfaces, building the parasitic resistance.

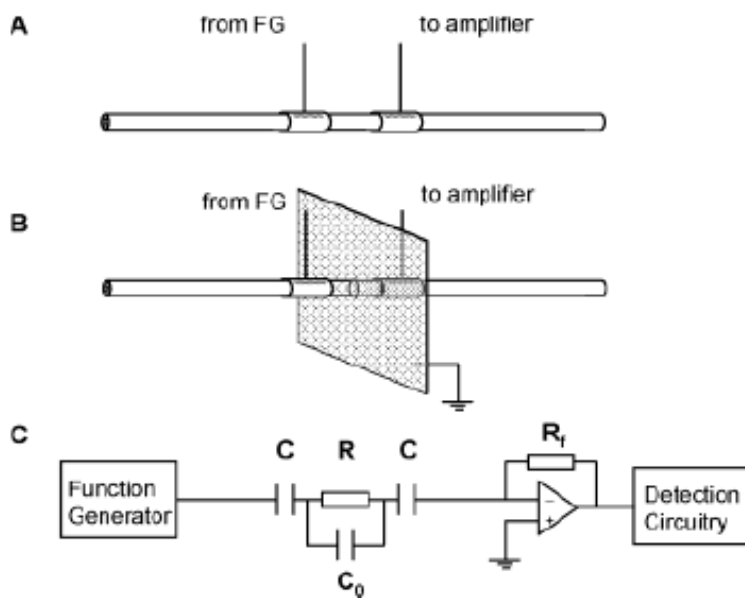


Figure 3.7 The functioning principle of the C4D system. A: a sketch of the C4D cell without shielding, B: a sketch of the C4D cell with shielding, and C: a simple equivalent circuitry representing the cell without the faradaic shield. FG: Function Generator, C: cell capacitance, R: cell resistance, C₀: stray capacitance and R_f: the feedback resistor on the amplifier (Kuban and Hauser, 2004).

The two electrodes are the excitation and detection electrode respectively. Whenever an AC voltage is imposed, a capacitive transition takes place between the electrodes and the inside of the capillary (the capillary wall with everything that includes), act as a capacitance, while the gap among the electrodes acts as a resistor. Hence, this system can be depicted as a series of a capacitor (C), a resistor (R), and another capacitor (C) (Zeeman, 2003). However, it should be noted that this plain model does not take into consideration that the sample solution inside the capillary exhibits some electrical resistivity as well (Baltusen et al., 2002). If a grounded shield is not applied, a stray capacitance C_0 emanates from the electrode coupling. In order to eliminate the capacitive coupling effect, a grounded shielding, regularly made of a thin metal sheet or foil, may be placed among the electrodes (Baltusen et al., 2002).

Whenever an AC voltage is implemented to the excitation electrode, the produced AC current (which is directly proportional to the conductance or inversely proportional to the resistance of the solution according to Ohm's law) runs through the cell, and is detected by the second electrode.

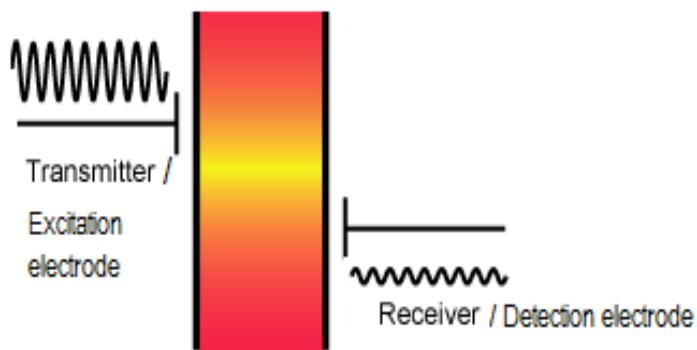


Figure 3.8: A sketch of the procedure between the excitation and receiver electrode, whenever an AC voltage is applied between them. The second electrode receives a corresponding attenuated AC signal (EDAQ website: <http://www.edaq.com/c4d-contactless-conductivity-introduction>).

The detected current is different than the one initially produced to the transmitter. The dissolved ions of the solution have different electrophoretic mobilities and thus, they pass through the detection region in a different rhythm, causing small changes in the local electric field of the flow (Alves et al., 2005), which are detected by the receiver electrode. Continuous recording of the electric current displays a series of peaks, which correspond to high ionic concentration and thus high conductivity values. Therefore, changes in the conductivity of the solution inside the capillary between the electrodes can be monitored and measured (EDAQ website: <http://www.edaq.com/c4d-contactless-conductivity-introduction>).

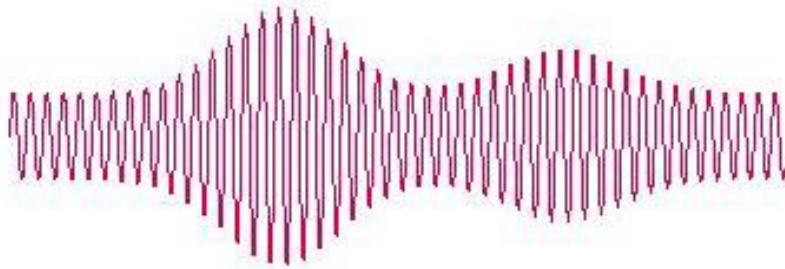


Figure 3.9: The amplitude of the detected signal is related to the conductivity of the sample. (EDAQ website: <http://www.edaq.com/c4d-contactless-conductivity-introduction>)

Then, the received current is transformed back to DC voltage into the amplifier, as stated in the equation (Kubán et al., 2004)

$$V_{out} = -iR_f \quad (3.2)$$

With V_{out} being the output voltage in V, R_f the feedback resistor value of the amplifier in Ω , and i the AC current in A (Kubán et al., 2004).

The current flowing through the detection cell for a given input voltage, is determined by the conductivity of the sample solution, which is the reverse of the sample resistance. In addition to sample the resistance (R), the capacitances (C, C_O) also determine the response of the system to an applied AC input voltage (V_{in}). The input AC voltage is characterized by an amplitude and frequency, and therefore all of these parameters will define the output voltage signal V_{out} (Baltusen et al., 2002, Handbook of EDAQ C4D:NBI Application Tech Note July 2012).

$$V_{out} = - \frac{V_{in}}{\frac{1+j2\pi fRC_O}{j2\pi f(C+C_O)\left[1+\frac{j2\pi fRCC_O}{C+C_O}\right]}} R_f \quad (3.3)$$

with V_{out} being the output voltage in V, V_{in} the input voltage in V, R_f the feedback resistor value of the amplifier in Ω , R the sample resistance in Ω , C_O and C the stray and cell capacitance respectively in F, f the input frequency in Hz, and j the imaginary unit (Kubán et al., 2004). The above expression relates the V_{out} response of the circuit with the impedance (Z) that it presents, when current i flows through it (Baltusen et al., 2002)

$$Z = \frac{1+j2\pi fRC_0}{j2\pi f(C+C_0)\left[1+\frac{j2\pi fRC_0}{C+C_0}\right]} \quad (3.4)$$



Figure 3.10: The amplifier deconvolutes and converts the AC voltage into a DC analog voltage signal, whose amplitude is determined by the conductivity of the sample solution (EDAQ website: <http://www.edaq.com/c4d-contactless-conductivity-introduction>).

3.4.2.1.2 The capacitively-coupled contactless conductivity detection system

The capacitively-coupled contactless conductivity detection system used for this thesis, is consisted of the ET125 Head Stage and the C4D 225 System (Model ER225). They have been properly adjusted to the Niels Bohr Institute application for a conductivity meter to measure the conductivity of the arctic melt water within the range of 100nS/cm to 10µS/cm (Handbook of EDAQ C4D: NBI Application Tech Note July 2012). The ET125 head stage connects to the C4D 225 System, and compose a contactless conductivity detector (C4D). For this special application a plain tube and not a capillary tube carries the sample to the head stage. The C4D 225 System produces the AC frequency voltage that through the excitation electrode produces a current that runs through the sample, which is picked up by the detection electrode. The amplitude of the received current is determined by the conductivity of the sample (EDAQ C4D website: http://www.edaq.com/product_sheets/transducers/ET125_General_Purpose_C4D_Headstage.pdf).

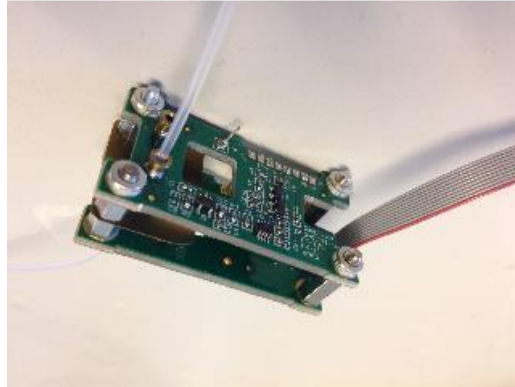


Figure 3.11: The internal and external part of the head stage with a tube passing through it. For this application the head stage is consisted of two measurement circuits, in which two solutions can be measured simultaneously. (EDAQ C4D website: http://www.edaq.com/product_sheets/transducers/ET125_General_Purpose_C4D_Headstage.pdf)

The head stage circuit, consists of a sample circuit and a reference circuit. The two circuits are alike and each one of them forms one arm of the bridge circuit. The two arms of the circuit bridge are driven by two balanced video amplifiers, and this configuration is chosen because it decreases the stray capacitance effects on the circuits. Each circuit consists of a tube that introduces the sample to the excitation electrode. The excitation electrode produces a current that goes through the sample resistor (R), and the current is finally picked up by the detector electrode. The electrode is of 5mm length and the electrode gap is 20mm. Between the excitation and detection electrodes exists the stray capacitance (C_o), which is decreased as much as possible by the bridge configuration and by the faradaic shield placed between each pair of transmitter/receiver electrodes. Each circuit can be used to measure the sample independently. If both of them measure the same sample solution simultaneously, then the two signals are cancelled out and the final output signal will be due to any variations in conductivity of the sample measured in the two circuits. This is expressed by the sample resistance $R+\Delta R$, where ΔR is a variation in resistance.

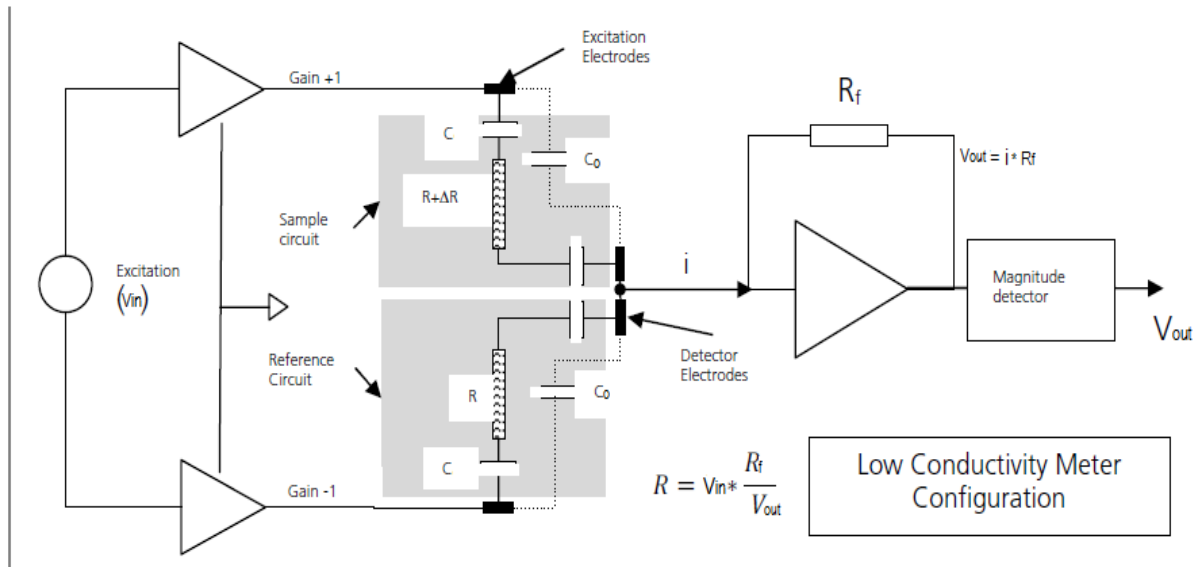


Figure 3.12: The head stage circuit configuration. (Handbook of EDAQ C4D: NBI Application Tech Note, 2012)

The excitation voltage (V_{in}) is 20Vpp. Although it can be modified from 1% to 100%, all the conductivity measurements were conducted at full 100% value of the 20Vpp. The frequency range of the voltage signal is from 2kHz to 2000kHz. R_f is the feedback resistor value of the current to voltage converter amplifier in Ω .

The current to voltage converter amplifier produces the output voltage (V_{out}), and it is related to the R_f according to equation (3.2). For this application, R_f is equal to 1000k Ω , and by changing it, the gain of the circuit changes. The output voltage (V_{out}) is a DC signal that has been rectified and filtered in the current to voltage converter. Its magnitude represents the magnitude of the current that is detected, and the detected current is proportional to the sample conductivity and inverse proportional to the sample resistance (Handbook of EDAQ C4D: NBI Application Tech Note, 2012).

As we may notice in equation (3.3) the output voltage depends on the input voltage amplitude (V_{in}) and frequency (f), on circuit resistance (R), on stray capacitance (C_0) and on cell capacitance (C). Change in the last three circuit components affect the response of the system for, as we may notice in the Figure (3.13) below.

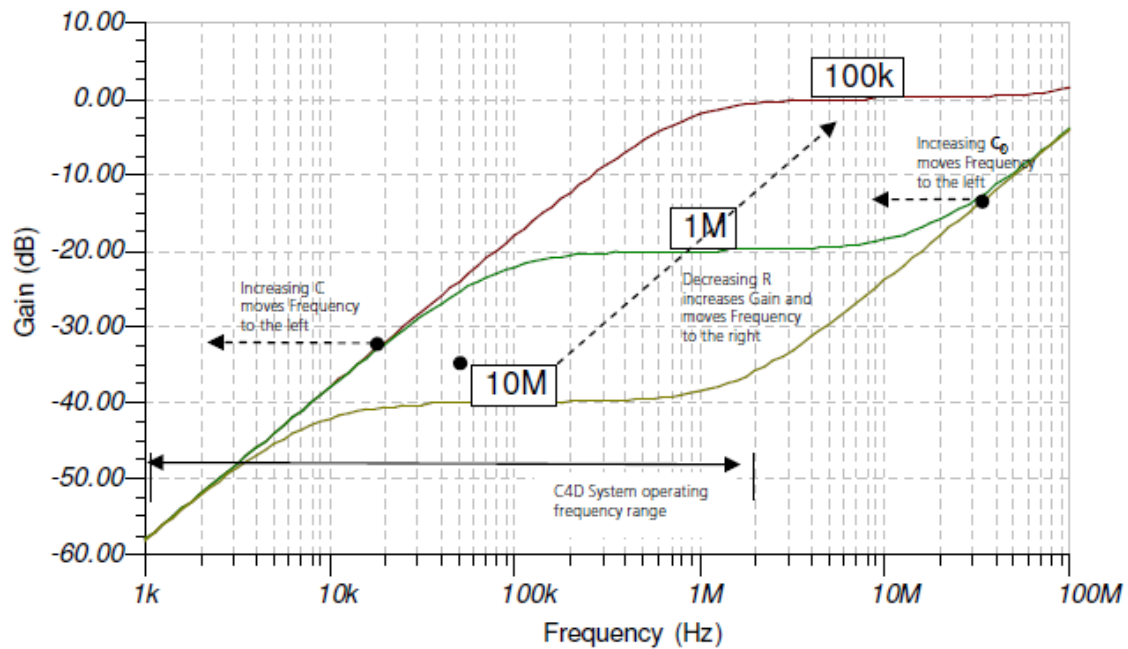


Figure 3.13: Frequency spectra shown the effect of C_o , C and R (NBI Application Tech Note, 2012).

The above figure is the frequency response curve of the video amplifier of the system and provides a picture of its performance for various frequencies. Specifically, in the section where the plot is flat or has the minimum slope, the amplifier has an equal response (gain) for every frequency within the band, and therefore exhibits the maximum stability to changes in the sample solution conductivity. The best possible situation is when the flat part of the plot is extended as much as possible. This can be succeeded by changing C_o , C and R components. C_o , C are fixed by the head stage and electrode geometry, and are properly chosen for this purpose. The resistance R depends on the conductivity of the solution and on the tubing length and cross-sectional area (Handbook of EDAQ C4D: NBI Application Tech Note, 2012).

3.4.2.1.3 The ER225 C4D Data System

The ER225 C4D Data System produces all the pulses send to the headstage for detection of the conductivity solution, records and displays the data acquired. It includes the ER280 Power Chrom Hardware, which is the data recording system. It also includes the C4D profiler, which

produces graphs that display the voltage response of the system to all frequencies, excitation voltages and head stage Gain settings (EDAQ C4D website: <http://www.edaq.com/ER225>)



Figure 3.14: The ER225 C4D Data System used for this thesis.

3.4.2.2 Conductivity Meter Model 3082 Series

The detection circuit of this instrument, is the 829 Micro Flow Cell, which is a traditional 2-pole cell, with two electrodes to apply an alternating AC voltage. It is characterized by the cell constant, (K) which is equal to 100cm^{-1} , and is the ratio of the distance (l) between the electrodes to the effective cross section of the conducting path (S). A tube contains the sample solution flow, and the electrodes are in contact with the sample. The AC voltage that is applied, is produced in the Model 3082 Series Multi-Function Conductivity Meter, and is within frequency in the range of 33 Hz to 31 KHz.

One of the main differences with the C4D method, is that here we cannot adjust the frequency of the incoming pulse. As ions of the sample solution pass through the first electrode, the impedance of the small gap between the two electrodes changes, and this change is received by the second electrode; and is afterwards transferred to a suitable electronic circuit in the Model 3082 Series; that modifies and displays the change to the conductivity value of the sample solution (Model 3082 Series Operational Manual). The Model 3082 Series is a multi-function meter composed for the measurement of Conductivity and Temperature of aqueous solutions. It has six ranges, each from 0 - 3300 counts. Additionally, it uses the conductivity measurements to calculate the resistivity, which is the reciprocal of the conductivity, and other properties of the solution, such as the salinity, and the total dissolved solids in the solution. Another characteristic of the 829 Micro Flow Cell is that it incorporates a thermistor for temperature measuring, so that temperature can be displayed simultaneously with conductivity. The temperature range is from 0°C to 70°C and is exhibited to the right of the conductivity or resistivity measurement. The Model 3082 Series is made to use a cell with a constant of 10cm^{-1} . The fact that the 829 Micro Flow Cell has a cell constant of 100cm^{-1} , means all displayed readings must be multiplied by 10 (Model 3082 Series Operational

Manual and website: <http://www.conductivity-meters.com/microflowCells.html>). Finally, the Model is supplied with a software program that monitors and records the data through a serial connection (Model 3082 Series Operational Manual).

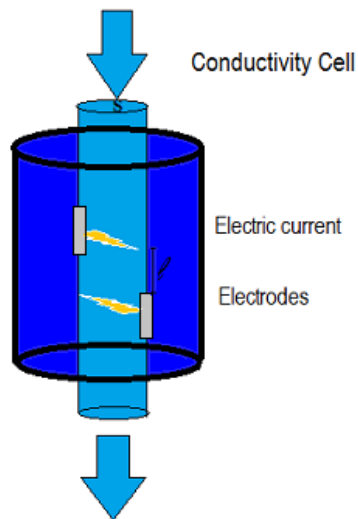
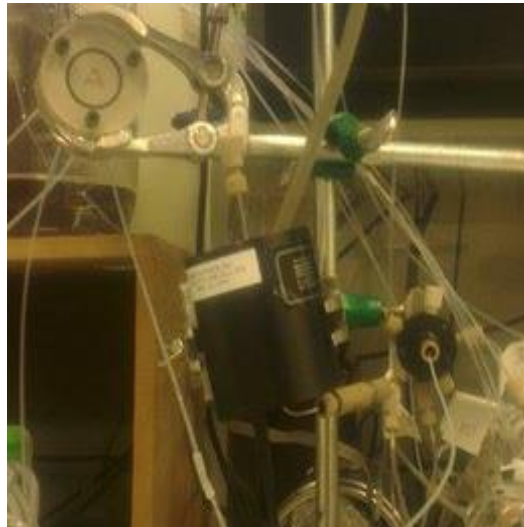


Figure 3.15 Up a picture of the 829 Micro Flow Cell in the CFA laboratory, and down a sketch of the cell, depicting its working principle.

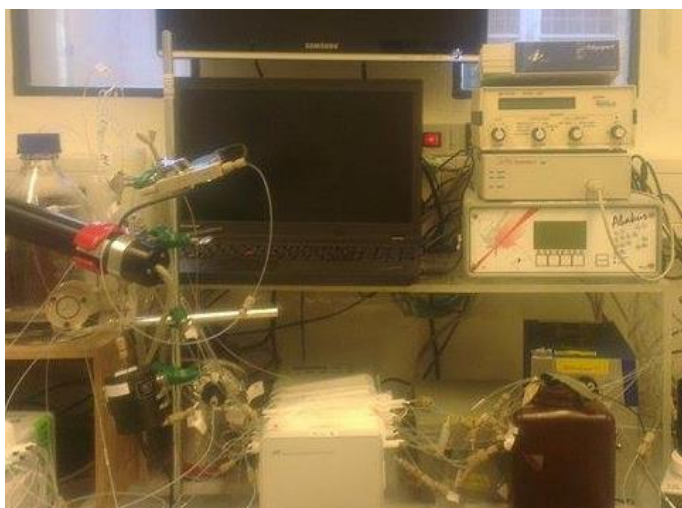


Figure 3.16: The ET125 Head Stage is kept inside a metal box to avoid interference with external electric fields. The ER225 C4D 225 Data System can be seen second to the bottom. The 829 Micro Flow Cell, in the front, and the Model 3082 is placed second to the top.

3.5 Testing the EDAQ C4D

Several experiments were performed in order to test the response of the new instrument (ET125 Head Stage and C4D ER225 System) in solutions of different conductivity, in melted ice samples, and also relatively to the Conductivity meter Model 3082 Series. Furthermore, the response of the two headstage circuits (sample and reference circuit) was tested, in same conductivity solutions, and also the response of the instrument to different type of tubes. For this purpose the Hanna instrument HI 7033 and HI 8033 Standard Conductivity Calibration Solutions were used. The first is an aqueous solution and the second is a water solution of sodium chloride: < 0.01%.

Each time an experiment was performed, new solutions were made in order to avoid contamination from carbon dioxide gas that dilutes into water solutions, and in order to avoid contamination due to the fact that glass bottles, that are used to make and store the solutions, possess hydrophilic properties, and thus are over time subjected to a corrosion process that contaminates the solutions and changes their conductivity (Tournié, 2008).

For this reason new conductivity standards were made each time, in order to have the same conductivity values.

Bottle	Conductivity($\mu\text{S}/\text{cm}$)
C ₁	75
C ₂	7.5
C ₃	4
C ₄	3
C ₅	2
C ₆	1

Table 1: Conductivity solutions

At the beginning, all the bottles along with all the laboratory equipment used to make the solutions, were carefully cleaned with Milli – Q ultrapure water. The solvents were added with the macropipette Calibra 832, and the solute with the 11C4842 Series dispensette. In each dilution, a volume of solute is added, according to the conductivity value we want the new solution to have. The conductivity values of the standards, were chosen because they are indicative of the conductivity range we expect to detect in an ice core.

Each solution was made separately, by diluting an amount of C₂ solution to a new bottle, and not from diluting each previously made dilution to a new one, in order to avoid the propagation of errors throughout the solutions.

During the experiments, the temperature of the environment remained practically constant, with minor variations that is which is not expected affect the conductivity value of the solution.

After having performed the calibration experiments, the best frequency range of the new instrument, for detecting conductivity in ice cores was set and the method was ready to be applied in the melted ice cores. More details about the results of the previously mentioned experiments, are present in the next chapter.

Response time

While the accuracy of the instruments is tested by calibration, the speed by which they detect any significant change in the value of the measuring parameter is defined by their response time. The response time is determined by exposing the instrument to a step function and measuring its response time from the output (Kalantar-zadeh, 2013). Therefore, an ideal opportunity for estimating the response time of the instrument is when standard solutions run in the CFA system.

3.6 Cutting the Ice Core

The ice core used for the conductivity measurements in this project, is a 45-m long, firn core, which was drilled at South Dome (63°32'N, 44°34'W), as part of a campaign aiming to study snow and firn in Southern Greenland (Freitag et al.; 2014). The location of the ice drill can be seen in the map below:



Figure 3.17 A view of Greenland with South Dome depicted as a star. (Google Maps, 2014, South Dome, 63° 32'N, 44 ° 34'W.)

After the ice core is cut, it was separated in bags of 0.55m, and a set of six consecutive bags make a “run”. The diameter for the ice core is 7.4cm. The ice core is cut parallel to its axis in 4 particular pieces, and each one is dedicated to specific set of measurements.

The central part of the core, piece 5, was analyzed for impurities in the CFA laboratory. Piece 1, is specially cleaned, and is used to measure the electric conductivity of ice (ECM). Pieces 2, 3, 4 are used for measurements of gas, stable isotopes, and physical properties of the ice. The ice core was transferred to the freezer of the Center for Ice and Climate in Copenhagen. The freezer has a mean temperature of -25°C and contains 15km of ice from Greenland and other drilling projects (Center for Ice and Climate, webpage: http://www.iceandclimate.nbi.ku.dk/research/drill_analysing/cutting_and_analysing_ice_cores/).

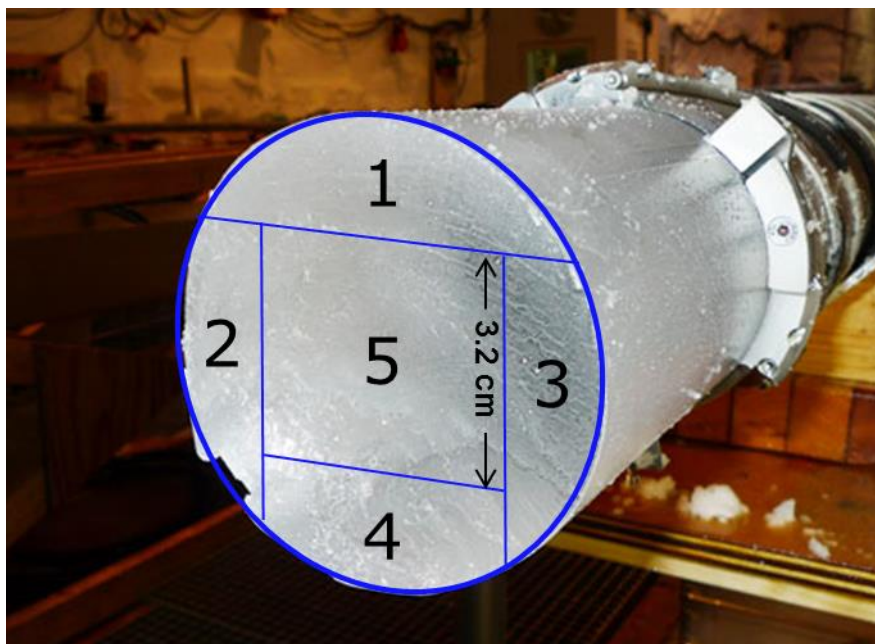


Figure 3.18 A sketch of the cutting plan for the shallow ice core (Weng, 2014).

Before melting the ice core, both of its edges and any break in between, are removed from it in order to avoid contamination. At the start and at the end of melting each run, a 10cm thick cube of frozen ultra-purified water is placed in the ice core to clean the system from any contamination caused by impurities enclosed to the previously melted ice. The first 45m of firm ice from the South Dome were melted at the 14th and 15th of May 2014. During the first day, 3 runs were melted, with each run corresponding to bags 3-8, 9-14, and 15-20 respectively. During the second day, 4 consecutive runs were melted, with each run corresponding to bags 21-26, 27-32, 33-38, and 39-

46 respectively. At the beginning and at the end of each day standard solutions of PH, calcium, sodium and sulfate were used to calibrate the instruments, in order to test their response to different contractions and adjust them properly, if needed.

Finally, 45m of ice were successfully melted and we were happily provided with a great amount of data to work with.

Chapter 4 Results

In this chapter the results of the experiments, which are performed in order to test the new instrument ET125 Head Stage and C4D ER225 System are presented, along with the results obtained from melting 45m of the South Dome ice core. The response of the instrument was tested by applying different conductivity solutions, by using different types of tubes, and by comparing the reference and the sample circuit; additionally the response time of the instrument is calculated and is compared with the Model 3082.

4.1 Testing the C4D ER225 System

4.1.1 The Voltage Response

At first the voltage response of the instrument was studied for different standard conductivity solutions. As mentioned in chapter 3, the Conductivity Calibration Solution HI 7033 was used. In bottle C₁, 50ml of it was poured, then a proper amount of it was transferred by the micropipette to bottles C₂, C₃, C₄, C₅ and C₆. Each was diluted by added a proper amount of ultrapurified MQ water with the dispensette, and finally each bottle contained a solution of known conductivity. Additionally, bottle C₇ was used to measure the response of the instrument to MQ water, indicating the background conductivity of the solutions. The measurements were performed starting from MQ water (bottle C₇) to the lowest conductivity solution (C=1 μ S/cm, bottle C₆) and all the way to the highest conductivity (C =7.5 μ S/cm, bottle C₂). The tube that was used was made of PFA with an internal diameter I.D. = 0.03”.

Figure 3.1 is shows the voltage response of the instrument for input voltage in the range of 2kHz to 2MHz and for different conductivity solutions. We may notice that there are two groups of curves, one for “High Gain On” and one for “High Gain Off”, and that for the latter group the voltage response is between 0.01-0.35V, while for the former group the voltage response of the instrument is much higher, within the range of 0.2-2.17V. When the instrument is set to “High Gain Off”, the amplifier is off, while when it is set to “High Gain On”, the amplifier is on and magnifies the signal.

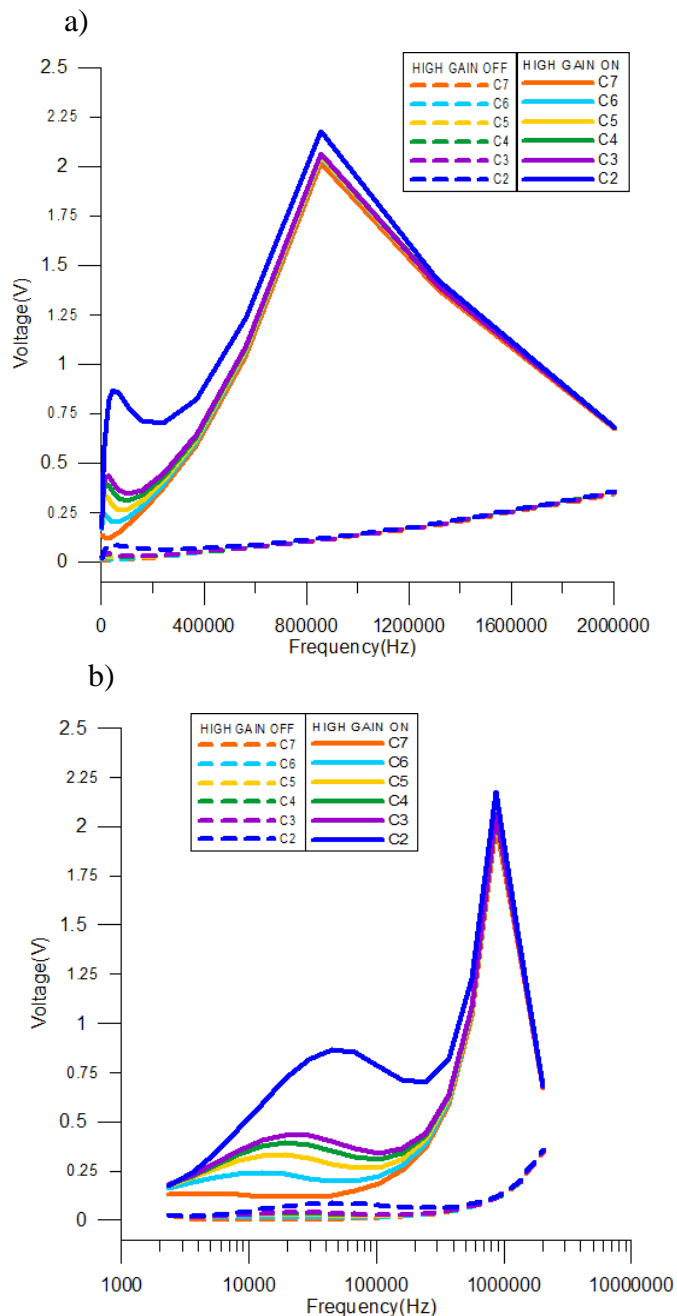


Figure 4.1 The voltage output of the instrument corresponding to the frequency range of the input voltage, for conductivity standards C₂ to C₆ and with C₇ being the MQ water; a) for linear frequency scale, and b) for log frequency scale.

Moreover, the frequency range of the input voltage is quite large and on a linear scale the small values of the voltage response are being compressed. Therefore, we change the frequency scale from linear to log and for High Gain On, we notice that the voltage response increases with the conductivity of the solution, and also that there are two dominant characteristics of the plot. The first is the maximum voltage response, which forms a high peak between 2.05V and 2.17V in the

859kHz frequency. The second characteristic is a wide maximum area that shifts from lower to higher frequencies as the conductivity of the solutions that are being measured increases. It lies between 0.24 and 0.87V, and is within the frequency range of 10 to 100 kHz. Additionally, for High Gain Off, we also notice these two characteristics but they are much smaller than they are for High Gain On and that they both are shifted to higher frequencies.

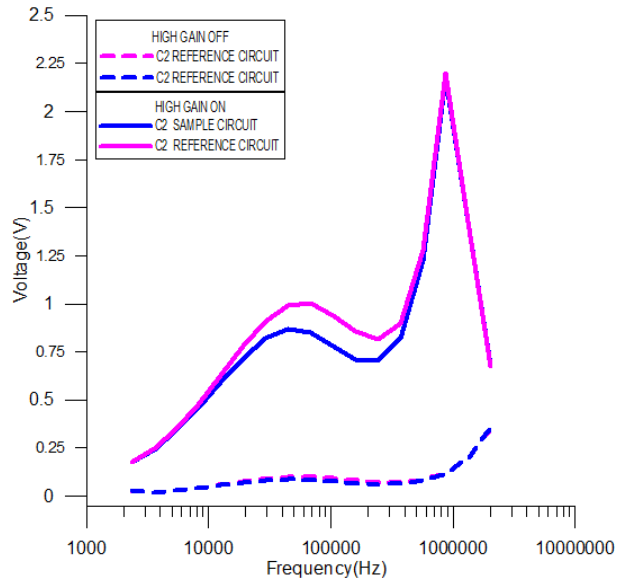
The two areas with maximum voltage responses are where the instrument has the highest sensitivity to measure conductivity. However, as the frequency of the input signal increases, so does the sensitivity of the instrument to detect noise. Therefore, the peak that corresponds to the 859kHz frequency encloses a peak detection of the instrument noise as well.

The wide maximum area lies in lower frequencies where the noise detection is smaller. Moreover, the maximum here is not a steep peak that increases and decreases abruptly within a small frequency range, but rather a broad maximum within a wider range of frequencies, which offers a stable voltage response of the instrument within this range. This area corresponds to the section of the frequency response curve of the video amplifier. It is flat or has a minimum slope, thus the amplifier has an equal response (gain) for every frequency within the band, and so it exhibits both the maximum stability and sensitivity to changes in conductivity.

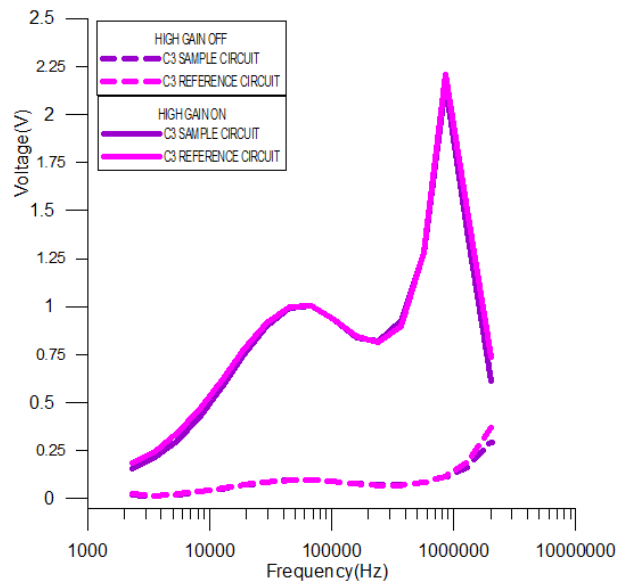
4.1.2 Sample and Reference Circuit

In this experiment, the response of each circuit of the headstage was tested for the same conductivity standards and tube that have been mentioned in the previous paragraph. As mentioned in Chapter 3, both circuits are capable of measuring the sample, and if both of them measure the same sample simultaneously, the final signal shows only the variation in conductivity of the sample, which is being measured in the two circuits. The purpose here was to compare the response of the circuits when measuring the same conductivity, and the results are depicted in Figure 4.2.

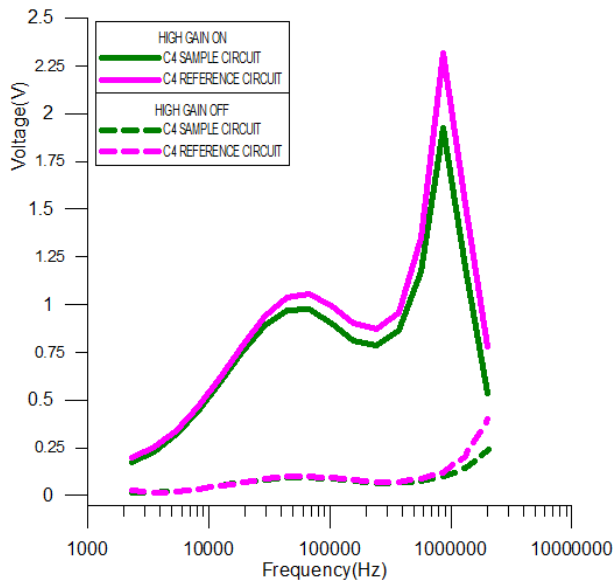
a)



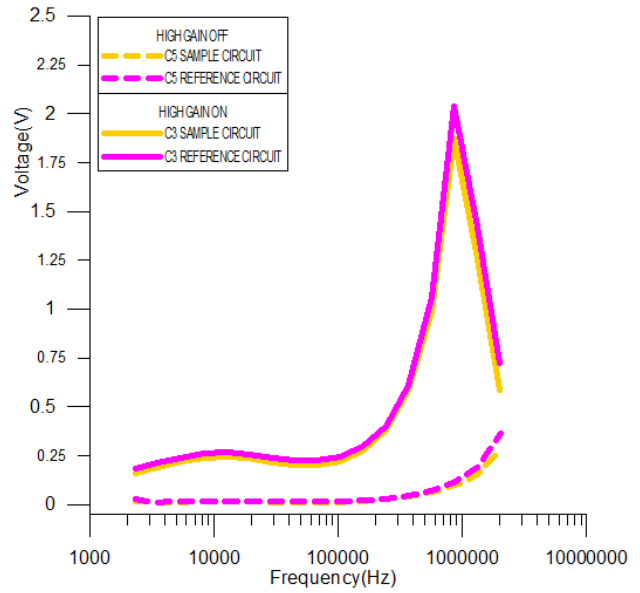
b)



c)



d)



e)

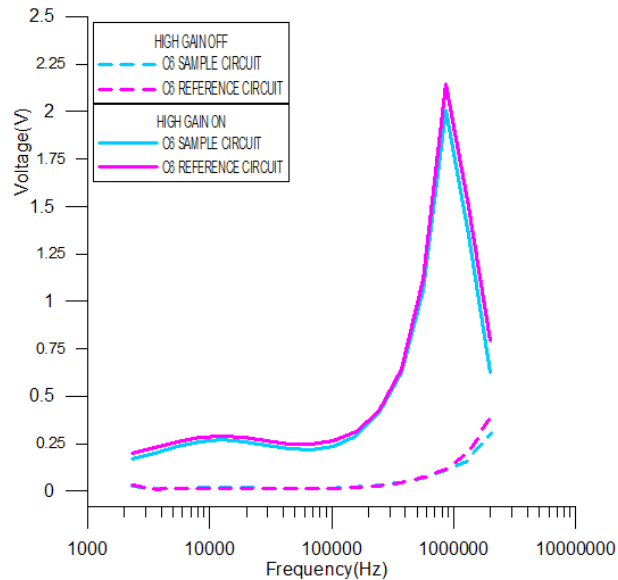


Figure 4.2: The voltage output of the instrument in respect to the frequency range of the input voltage, for the sample and reference circuit, and for conductivity standards a) C₂, b) C₃, c) C₄, d) C₅, and e) C₆.

The figure illustrates that the voltage response of the reference sample is larger or slightly bigger than the respective response of the sample circuit for High Gain On, and this difference gets bigger as the conductivity of the sample increases. For the High Gain Off mode, the response of the reference sample is equivalent to the respective response of the sample circuit or slightly larger, and this difference again, is illustrated in the high frequency range, where the noise level of the instrument rises. The maximum response lie in the frequency of 859 kHz and 2 MHz, for High Gain On and Off respectively; and they are stable for both circuits. The stable frequency range is within the range of 45-68 kHz for the conductivity solutions C₂ = 7.5 μS/cm, C₃ = 4 μS/cm, C₄ = 3 μS/cm, for both High Gain On and Off modes. For the low conductivity solutions C₅ = 2 μS/cm, C₆ = 1 μS/cm, the stable range shifts to smaller frequencies for both High Gain On and Off.

4.1.2 Testing Different Tubes

In this experiment, the response of the instrument was tested for the same conductivity standards but different types of tubes. The tubes were always placed on the sample circuit. The tubes have different sizes of internal diameters (I.D.), are made by different types of plastic (PEEK, PFA),

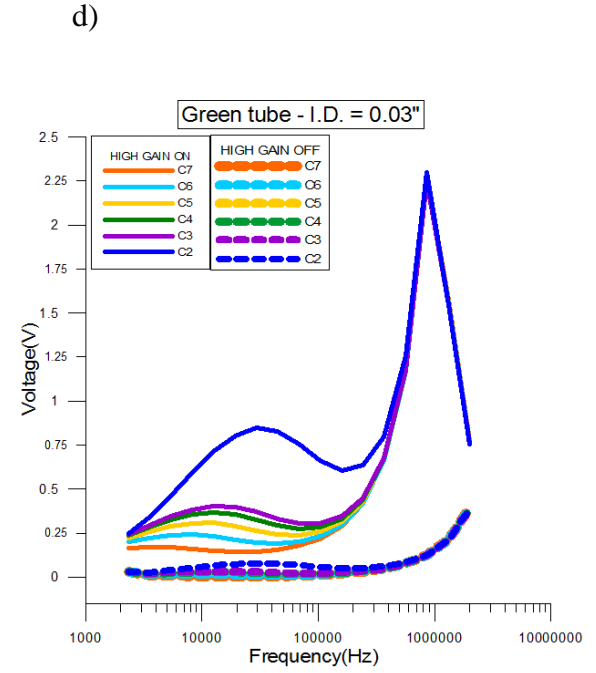
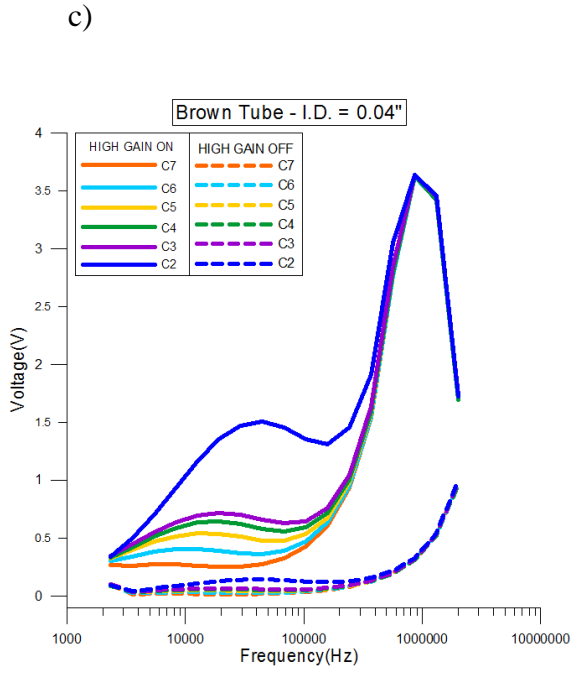
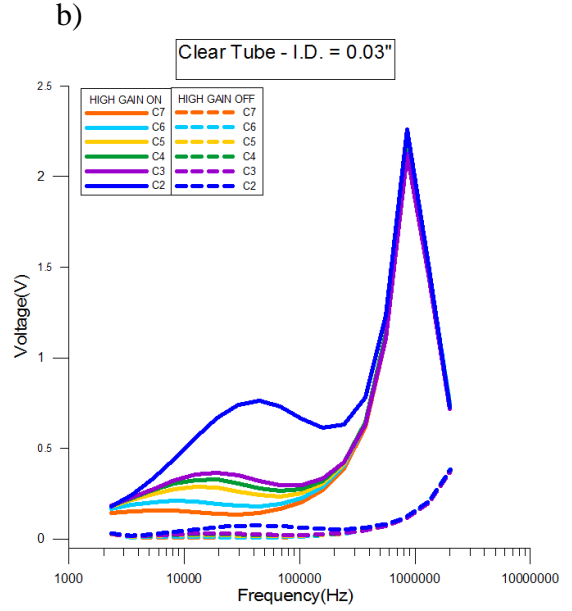
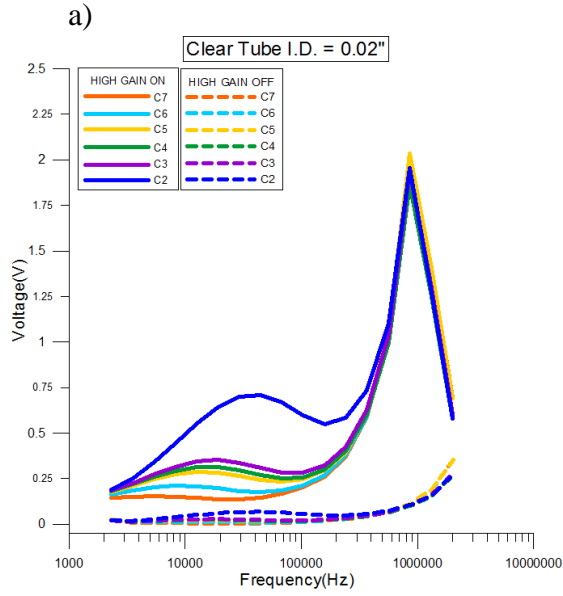
and have different colors (black, green, brown, and transparent-clear). They are presented in the Table 2.

Tube I.D.	PFA	PEEK
0.02''	Clear, Black	—
0.03''	Clear	Green
0.04''	—	Brown

Table 2: Types of different tubes used for testing EDAQ C4D.

These tubes are commonly used in the CFA lab and were chosen to assess if the size of the internal diameter and the type of material that the tube is made of, has an effect on the the response of the instrument. The different colors indicate differences in composition as well, since different metals are added in each case to provide a different color. The results are presented in Figure 4.3.

As it may be noticed, for the High Gain On mode, the response of the instrument gets higher as the size of the internal diameter increases. For the tube with the bigger internal diameter (PEEK, brown, I.D.= 0.04''), there is the highest voltage response recorded: $V_{out} = 3.64V$, corresponding to $f=860kHz$ and to the standard of the highest conductivity value C_2 . For the tubes with the medium, size of internal diameter, the maximum response is $V_{out} = 2.3V$, for the green tube (PEEK, green, I.D. = 0.03'') and $V_{out} = 2.26V$, for the clear tube (PFA, clear, I.D. = 0.03''). Both of them correspond to the frequency $f=860kHz$ and to the C_2 standard. Finally, the lowest voltage response is recorded for the tubes with the smallest internal diameter, $V_{out} = 1.96V$ and $V_{out} = 2.03V$ for the transparent (PFA, clear, I.D. = 0.02'') and black (PFA, black, I.D. = 0.02'') tubes respectively, again for the frequency $f=860kHz$. Interestinly, the maximum response for the clear tube, corresponds to one of the lowest conductivities, C_5 , while for the black tube it corresponds to the highest conductivity solution, C_2 .



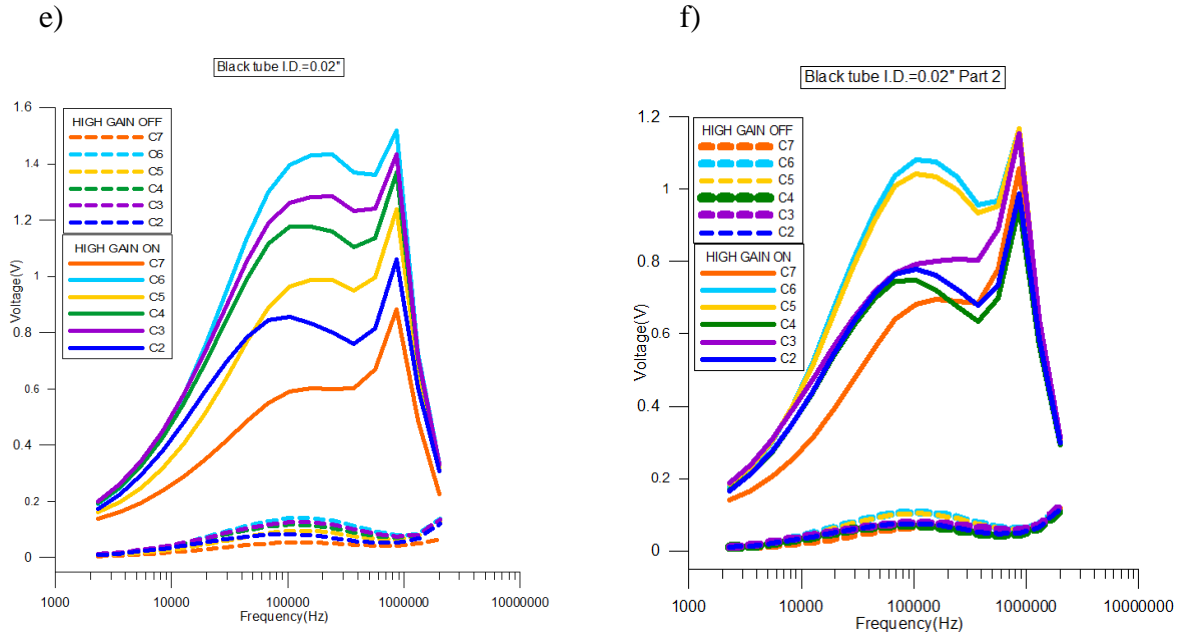


Figure 4.3: The voltage output of the instrument in respect to the frequency range of the input voltage, for the same conductivity standards and different types of tubes: a) Clear tube-PFA, I.D.=0.02'', b) Clear tube-PFA, I.D.=0.03'', c) Brown tube-PEEK, I.D.=0.04'', d) Green tube-PEEK, I.D.=0.03'', e) Black tube-PFA, I.D.=0.02'' part1, and f) Black tube-PFA, I.D.=0.02'' part2.

For the black tube, the measurements were performed twice, each to a different part of the tube, as in the first measurement, the voltage responses in C₂ and C₅ intersect. The same effect was for measuring a second part of the tube, the voltage responses C₂ and C₄ overlap with C₇. The maximum voltage response for this part of the tube is $V_{out} = 0.98V$. The maximum voltage response for the black tube is for the same frequency with the previously mentioned maximum responses of the instrument to the other tubes. Additionally, the response of the instrument is not in correspondence with the value of the conductivity. The maximum response is for the lowest conductivity solution, the minimum response is for the highest conductivity solution and the responses for the conductivity solutions between these two are not increasing or decreasing accordingly.

Moreover, the wide maximum amplitude seems to depend on the size of the I.D., and could be affected by the material as well. The respective frequency range, seems not to be affected.

Specifically, for the brown tube, the highest voltage response locates in C₂ solution, with the wide maximum amplitude being 1.47-1.51V in frequency range of 29-48kHz; and the lowest voltage response locates in C₆ solution, with 0.405-0.407V in frequency range of 8-13kHz.

For the green tube, the highest voltage response locates in C₂ solution, with the wide maximum amplitude being 0.85-0.83V in the frequency range of 29-48kHz; and the lowest voltage response locates in C₆ solution, with 0.237-0.241V in the frequency range of 5-8kHz.

For the clear tube with I.D. =0.03'', the highest voltage response locates in C₂ solution, with the wide maximum amplitude being 0.74-0.76V in the frequency range of 29-48kHz, and the lowest voltage response locates in C₆ solution, with 0.206-0.211V in the frequency range of 8-13kHz.

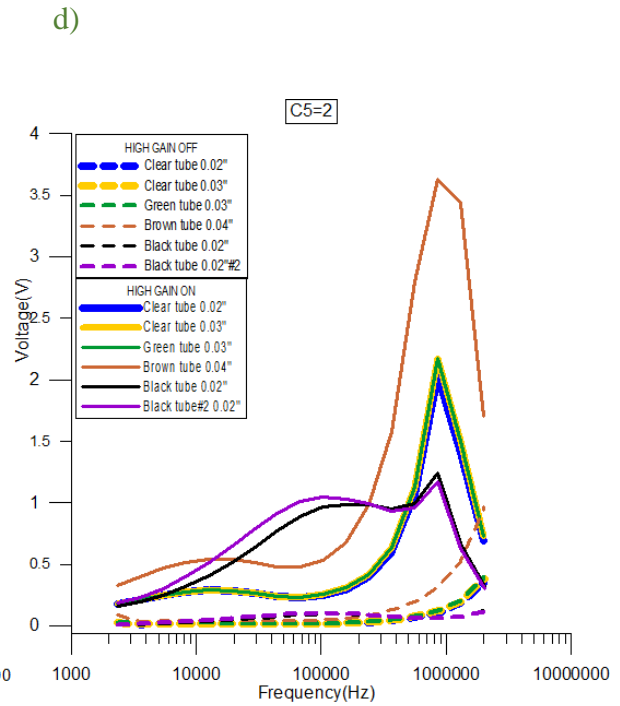
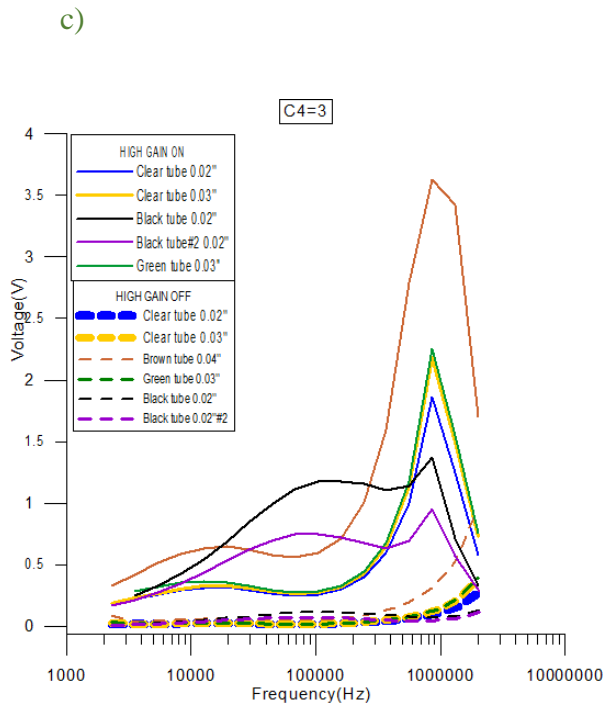
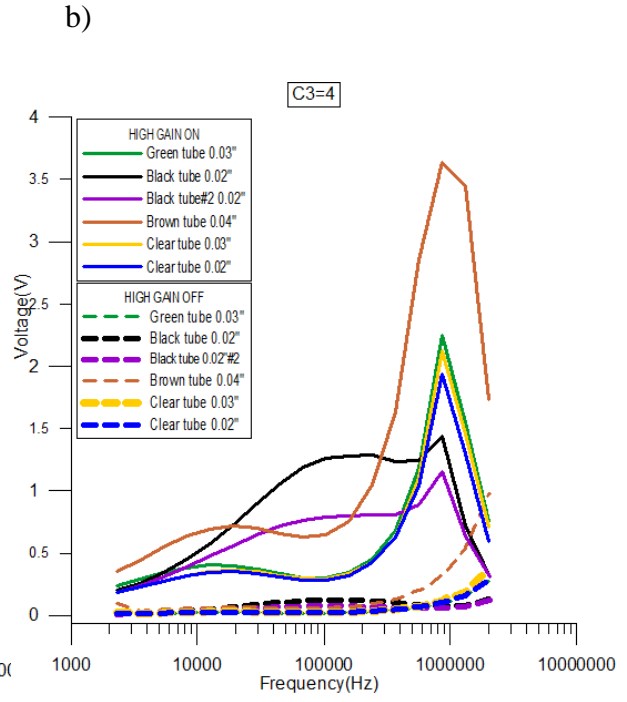
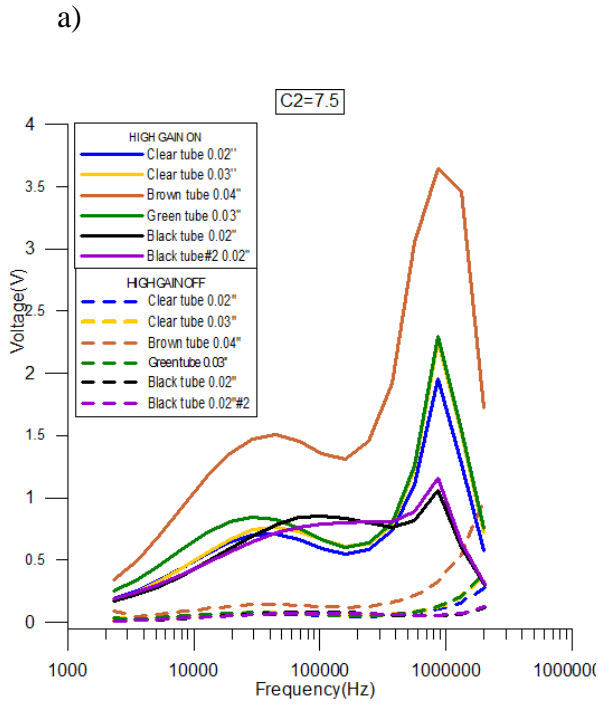
For the clear tube with I.D. =0.02'', the highest voltage response locates in C₂ solution, with the wide maximum amplitude being 0.7-0.71V in the frequency range of 159-242kHz; the lowest voltage response locates in C₆ solution, with 0.207-0.211V in the frequency range of 8-13kHz.

For the 1st part of the black tube, the highest voltage response locates in C₆ solution, with the wide maximum amplitude being 1.432-1.435V in the frequency range of 29-45kHz; and the lowest voltage response locates in C₂ solution, with 0.84-0.86V in the frequency range of 68-104kHz.

For the 2nd part of the black tube, the highest voltage response locates in C₆ solution, with the wide maximum amplitude being 1.076-1.082V in the frequency range of 104-159kHz; and the lowest voltage response locates in C₄ solution, with 0.745-0.749V in the frequency range of 68-104kHz.

Generally, the shape of the figures is the same for all tubes, except for black tube, where the instrument's response to the frequency, appears to be unique, and brown tube, where the shape of the curve is slightly different but not as different as it is for the black tube.

Another way to compare the response of the instrument to these tubes, is to plot for every conductivity solution the response of the instrument for each tube. You may see the result in Figure 4.4. The green tube has an internal diameter of 0.03'', and is made of PEEK, while the clear tube with I.D. = 0.03'' is made of PFA. Therefore we can directly compare if the material of the tube has an effect to the response. Furthermore the two clear tubes, are both made of PFA, but they have different I.D., thus the comparison of the instrument response to them for the same conductivity solution shows the effect of the size of the I.D. In Figure 4.4 a), we may notice that the green tube made of PEEK has a higher response than the clear tube of the same I.D., made of PFA, and that the latter has a higher response in comparison to the clear tube of I.D.= 0.02''.



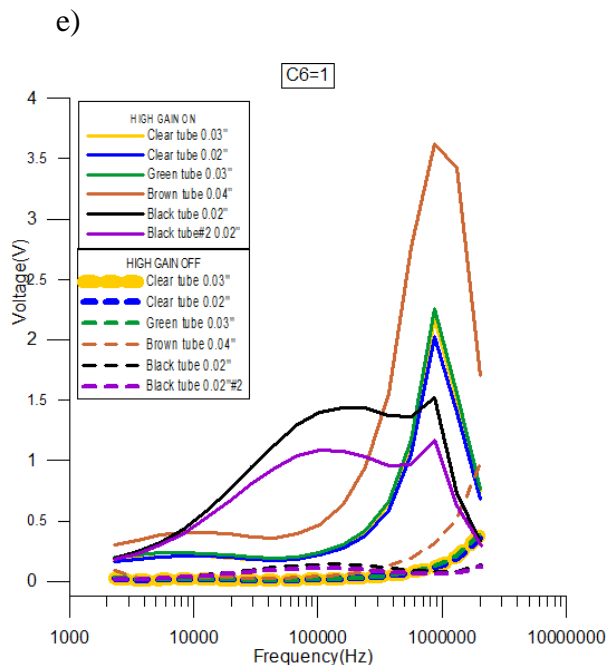


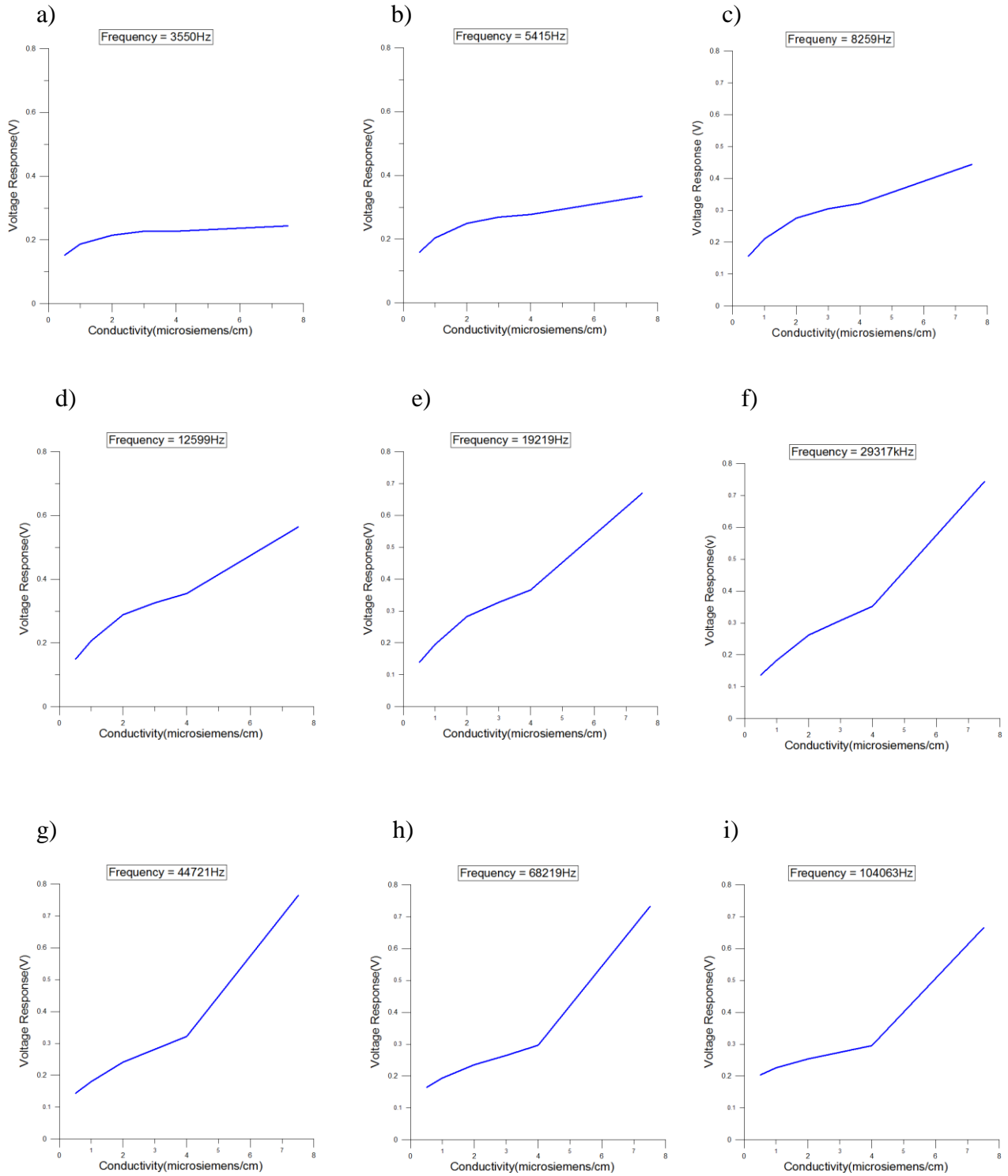
Figure 4.4: The voltage output of the instrument in respect to the frequency range of the input voltage, for each conductivity standard and for all the different types of the tested tubes, a) conductivity standard $C_2 = 7.5$, b) conductivity standard $C_3 = 4$, c) conductivity standard $C_4 = 3$, d) conductivity standard $C_5 = 2$, e) conductivity standard $C_6 = 1$.

However, the difference in the response between these three tubes becomes smaller (Figure 4.4 b) and c)), as the conductivity of the solution decreases, but they still have the difference in the order mentioned above: the higher response is for the green PEEK tube, I.D. = 0.03", then comes the clear PFA tube, I.D. = 0.03", and finally the clear PFA tube I.D. = 0.02". For the conductivity standards $C_5 = 2$ and $C_6 = 1$, the differences in the instrument's responses for these three are so small that the figures overlap, especially for frequencies smaller than 100kHz. The green and the brown tube, are made from the same material but have different I.D. We can see that the response of the brown tube, which has the largest I.D., is much higher for all the conductivity standards, though it follows the same pattern as the green tube.

4.1.3 Frequency Response

Another important factor to take into consideration is the instrument's response to measuring conductivity for a certain frequency. We would like to know the frequency or the frequencies of the input voltage that give a linear relationship between the output voltage and the conductivity;

therefore the voltage response of the instrument is plotted versus the conductivity standards for certain frequencies. This is shown in Figure 4.5.



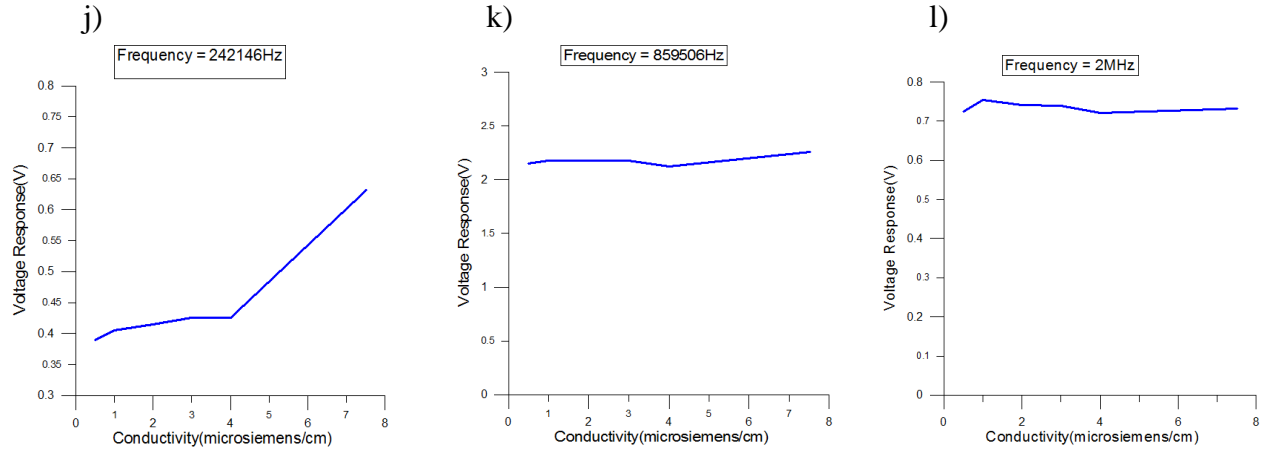


Figure 4.5: The voltage response of the instrument in respect to conductivity for the frequency: a) 3550Hz, b) 5415Hz, c) 8259Hz, d) 12599Hz, e) 19219Hz, f) 2931Hz, g) 44721Hz, h) 68219Hz, i) 104063Hz, j) 242146Hz, k) 589506Hz, l) 2MHz.

There is a wide range of frequencies of the voltage signal, but the frequencies corresponding to the wide maximum, or are close to it are the most important. Therefore we choose half of the frequencies from this range and mostly from 12kHz to 45kHz, where the wide maximum lies in most cases examined. Three frequencies are chosen under this range and three above it. For the frequencies 3550Hz and 5415Hz the voltage output is close to be stable, and consequently it does not seem to respond to changes in conductivity. For the frequency 8259Hz, there seems to be a very small change in response to conductivity variations, especially for 3-4 μ S/cm. For the frequencies 12599Hz, 19219Hz, and 29317Hz, the voltage output seems to respond to changes of conductivity, in a linear way which is not homogeneous, but consists of three different lines. For the frequencies 44721Hz, 68219Hz and 104063Hz, this seems to be the case as well, except that the response consists of two lines. Finally, for the high frequencies 242146Hz, 859506Hz and 2MHz, again the response of the instrument is constant or partly constant and therefore it cannot describe variations in conductivity. For the frequencies where the voltage response of the instrument is linear, the 19219Hz frequency, seems to approximate a more proper single linear relation between the voltage output and the conductivity change.

4.1.4 Time Resolution

Another interesting characteristic of the instrument is its response time. Response time is the time required for an instrument to respond to a sudden step change of the input, and it is defined as the time required for the signal of the step function to rise from 5% to 95% of the final output (Liptak,

1995). For the EDAQ C4D and Model 382 Series instruments, the step function is the shift from MQ water to a solution of a certain ionic concentration.

On Figure 4.6 the time response (time difference) is given for the respective change in conductivity and voltage for calcium, PH, and sodium standard solutions.

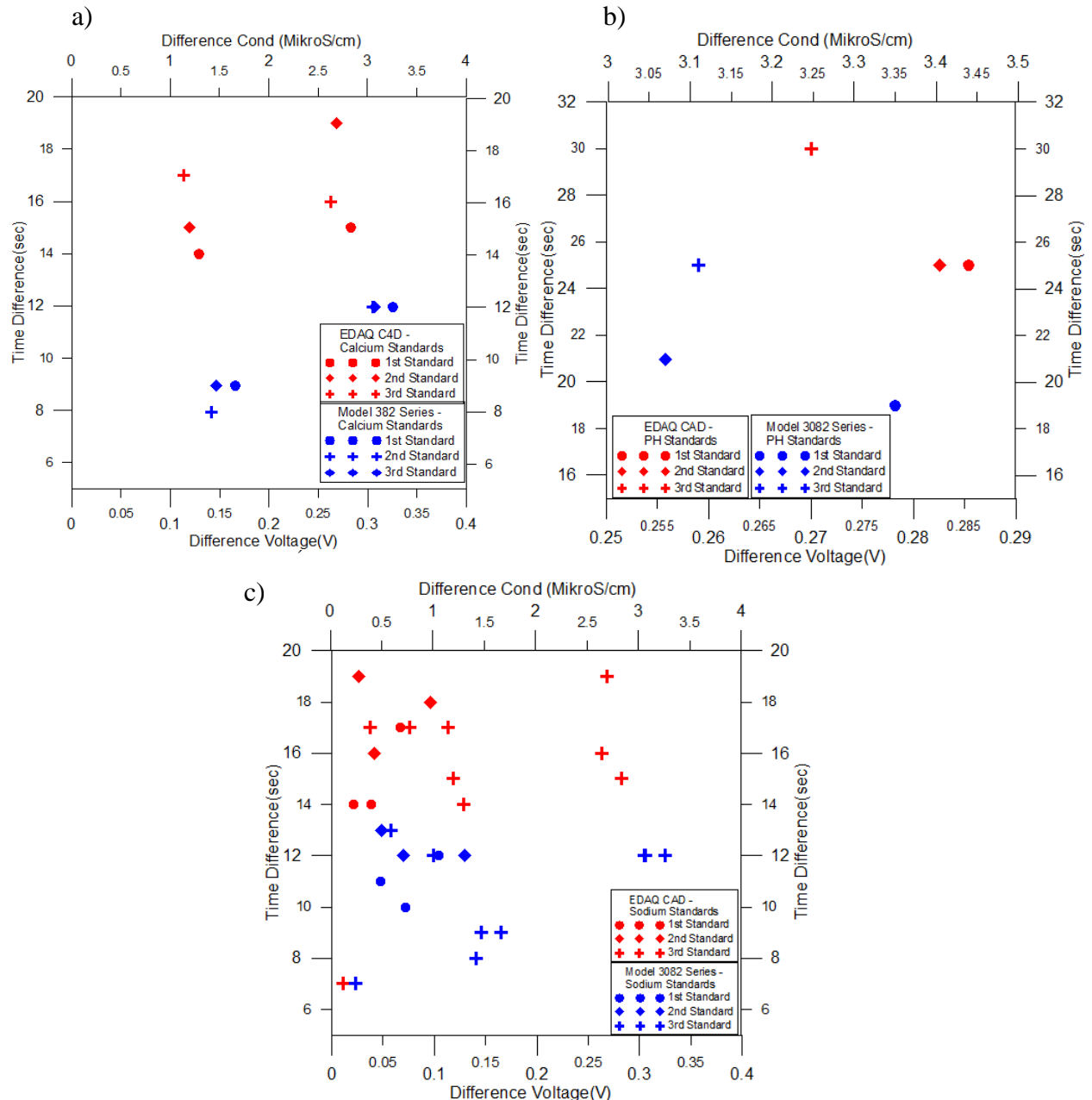
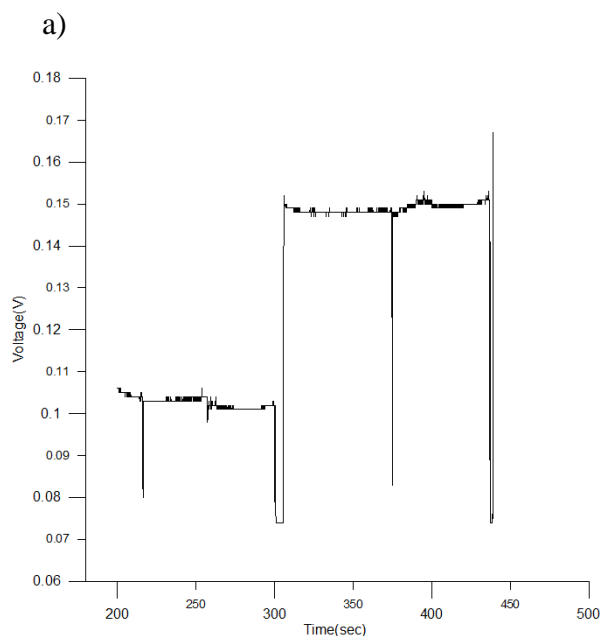


Figure 4.6: The time response when changing from MQ to standard solutions for EDAQ C4D and Model 382 Series instruments, for a) calcium b) PH and c) sodium standards.

For the calcium standard, two solutions were used to calculate the time difference, because between the first and the second solution, MQ was inserted into the CFA system. Likewise for sodium, except for sodium there are three solutions at each standard. For PH, only the time difference of the transition from MQ to the first peak was used, as PH standards are inserted into the system in continuous series.

From Figure 4.6, we may notice that, the Model 382 Series instrument has a smaller response time than the EDAQ C4D, and that the response time of both instruments is different for calcium, sodium and PH, with PH being the “slowest” and sodium the “fastest”. We may also notice that generally the bigger the difference between the conductivity baseline (MQ) and the conductivity signal of the standard, the bigger the response time of the instruments, especially for calcium. Moreover the time response of the Model 382 Series for the different standard solutions seems to be within a smaller range, than it is for the EDAQ C4D. In general it seems that the Model 382 Series is more consistent in time (less dispersion in y-axis) compared to the new instrument EDAQ C4D.

However, during the measurements the two instruments, were not placed close. There was a distance of about 1m between them. The Model 382 Series was first in line, and the EDAQ C4D second. Therefore, the EDAQ C4D measured a signal which had traveled a longer path, thus had been mixed more, than what it was measured from the first conductivity meter. Therefore, this signal was not the step function assumed at the start, but a more broad signal.



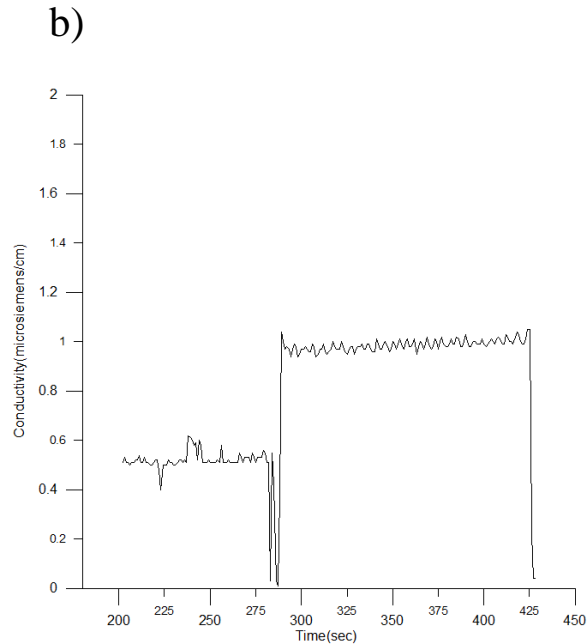


Figure 4.7: The time response when changing from MQ to conductivity standard solution $C = 1\mu\text{S/cm}$ for a) EDAQ C4D and b) Model 382 Series instruments

Another way to compare the resolution of the two instruments is to estimate their response for continuous measurements performed separately, when the two instruments are not connected in line. The step function in this case is the shift from MQ water to conductivity standard of $C = 1\mu\text{S/cm}$. For this case the time response of the EDAQ C4D is 3sec, and for the Model 382 Series 10sec. This estimation is more objective as the signal goes through the instruments separately. In Figure 4.7 we see shift between the MQ and the conductivity standard for the two instruments. The shift for EDAQ C4D is quicker and more direct.

4.2 Measuring Conductivity – South Dome Data

In this section, the results from measuring some of the impurities deposited in the South Dome ice core are presented. During the measurements, 45m of ice were melted in the melthead, and were driven into the CFA system via the peristaltic pump. In Figures 4.8, 4. 9, 4.10 the calcium, sodium, hydrogen cations, and conductivity aligned results are shown for different depths of the ice core. Each depth corresponds to a different time of deposition. The conductivity was measured in both

instruments, EDAQ C4D and Model 382 Series; for the first instrument, the output is voltage whereas for the second conductivity. The blue curve is calcium, the violet is sodium, the purple is dust, the green is hydrogen cations, the orange is conductivity and the red is conductivity measured by the new EDAQ C4D instrument.

One may notice that for all three figures, the calcium, sodium, dust and hydrogen cations measurements have some negative values. This of course is not a reasonable result, except for hydrogen cations, which indicates basic water. Such negative measurements in general emanate from the interference of air bubble with the measurements.

Below, the vertical black lines are to help us notice whether a peak in conductivity corresponds to a peak on any other component, and the light blue lines show the year of the deposition, indicating the annual layers of the ice core.

On Figure 4.8 we notice that in many cases a peak in conductivity and voltage corresponds to a peak hydrogen cations, and a peak in calcium corresponds to a peak in dust and sometimes sodium. However in depth 4.55m, dust also peaks with voltage, conductivity and hydrogen cations, and in 8.7m with calcium. On Figure 4.9 we may notice that at the 25.15m all constituents exhibit a peak, even though only a small one for sodium. Most black vertical lines here show some correlation between them. Specifically in 23.3m depth, all constituents peak, except for dust and sodium; and in 27.05m conductivity, voltage, hydrogen cations and calcium peak, even though the peak is small for hydrogen cations; and at depth 22.15m is an example where only one constituent, dust peaks. Finally, on Figure 4.10, at 29.5m and 32.6m, are two examples of simultaneously peaking of all the constituents, even though the peak for sodium in 29.5m is small; and for calcium and dust in 32.6m respectively. For the rest of black lines, we can see correlation between some of the species, for example in depth 28.8m, where calcium dust and sodium peak.

Na^+ is an index of sea salt and Ca^{2+} of dust. As was mentioned in Chapter 2, aerosols containing Ca^{2+} , Mg^{2+} , Na^+ , K^+ , SO_4^{2-} , Cl^- could originate from both sea and land, which could explain the simultaneous peaks of Na^+ and Ca^{2+} described above. The vertical light blue lines indicate time, and a consecutive pair of them is one year. In figures 4.8, 4.9, 4.10 we may notice that within a year, Na^+ and Ca^{2+} peak one or more times, but often there is only one peak that stands out. This peak is the maximum concentration of these species; and for sodium is in winter/early spring, while for calcium/dust is during spring/summer. We may notice that in most cases these high peaks do not coincide to the same depth, thus each signal's maximum concentration is for a different time of the year. In Greenland, sodium peaks in winter to early spring due to frequent advection of oceanic air masses above the ice sheet during winter (Legrand and Mayewski, 1997). Calcium peaks in spring and its main source is mineral dust coming from Asian deserts (Kuramoto et al., 2011). The concentration of hydrogen cations is indicative how acid or alcalic the ice is. As an important source of acids for the atmosphere is a volcanic eruption, a high peak in conductivity and hydrogen cations can be indicative of volcano eruptions (Taylor et al., 1992). In figures 4.8, 4.9 and 4.10 we see that sometimes conductivity and hydrogen cations peak simultaneously, marking a possible volcano eruption signal deposited at this specific depth. Finally, the annual

cycles of sodium and calcium, along with volcano reference horizons can be used to date the ice core (Kjær et al, 2013).

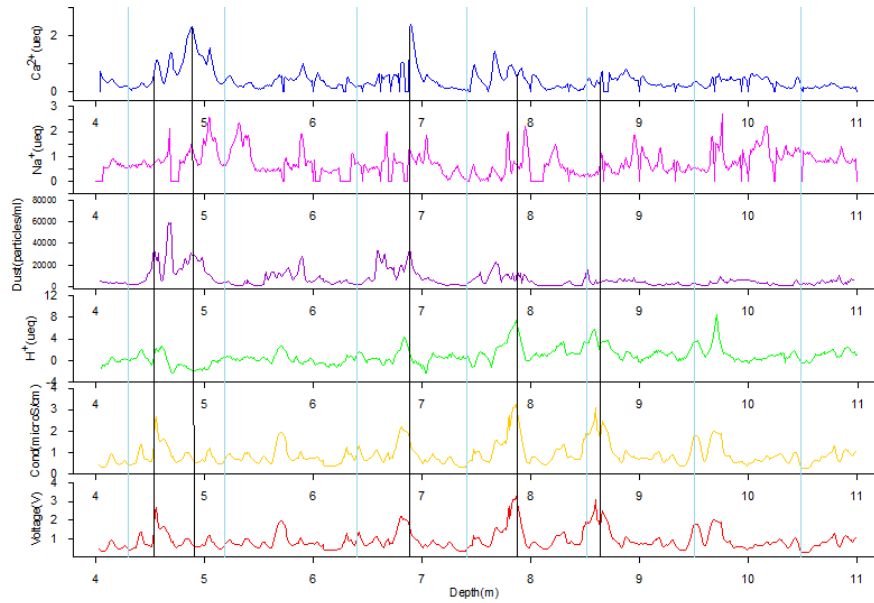


Figure 4.8: Calcium, sodium, hydrogen cations, conductivity and voltage versus depth for 4-11m, and time, with each pair of light blue lines representing a year, beginning from 2009 for 4.3m to 2003 for 10.5m with time step equal to one year.

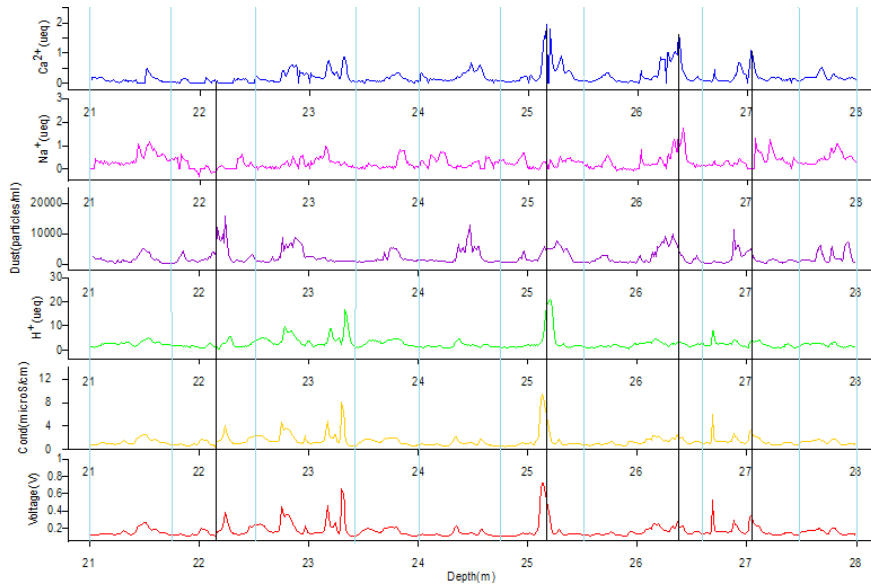


Figure 4.9: Calcium, sodium, hydrogen cations, conductivity and voltage versus depth for 21-28m, and time for 1991 matching with 21m to 1982 for 28m. Each pair of light blue lines represents consecutive years from 1991 to 1982.

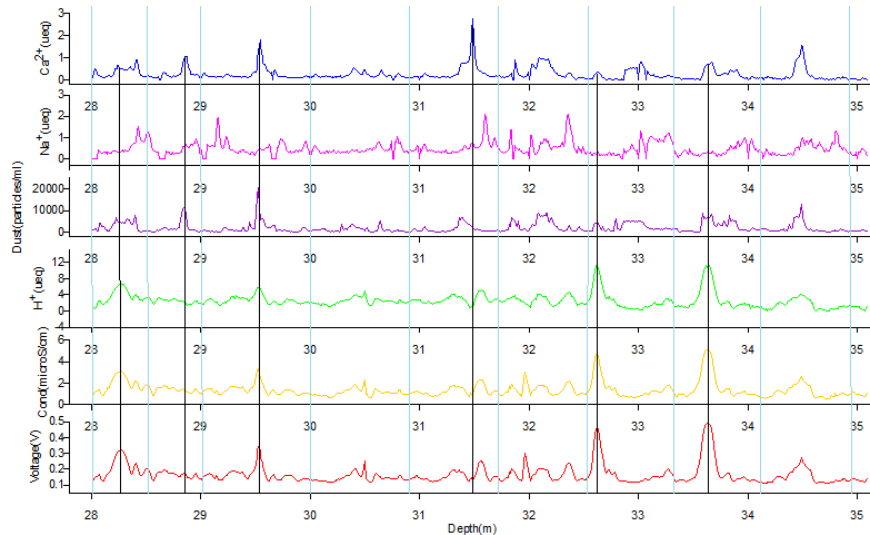


Figure 4.10: Calcium, sodium, hydrogen cations, conductivity and voltage versus depth for 28-35m, and for the years 1982 to 1972.

Furthermore, in Figure 4.11, we may notice the time of deposition for different depths of the ice core. The deeper we drill in the ice sheet, the older the ice we collect. The particular section of the South Dome ice core that we have measured, dates back to 1960, and in the figure appears to be a linear correlation between depth and time of deposition. However, ice cores hundreds of meters long, date back hundreds or thousands of years and in these depths, annual layers will be more compressed due to the pressure of annual layers lying above them. This pressure makes the thickness of the annual layers smaller as the depth increases, therefore a certain depth interval will correspond to a larger time step, and the correlation between depth and time becomes nonlinear for these depths (Divine et al., 2011)

Similarly in Figure 4.12, we see the annual layer thickness decreasing with depth. The upper deposited layers are the thickest. Further down, as the pressure increases the layer thickness decreases, as we can also see that from Figures 4.8, 4.9, 4.10. This decrease is not linear with depth, and is more intense in the upper layers of the core, which shows the densification process.

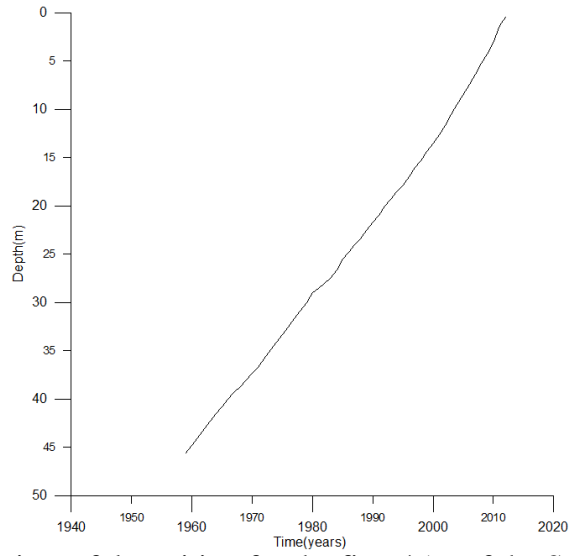


Figure 4.11: Depth versus time of deposition for the first 45m of the South Dome ice core.

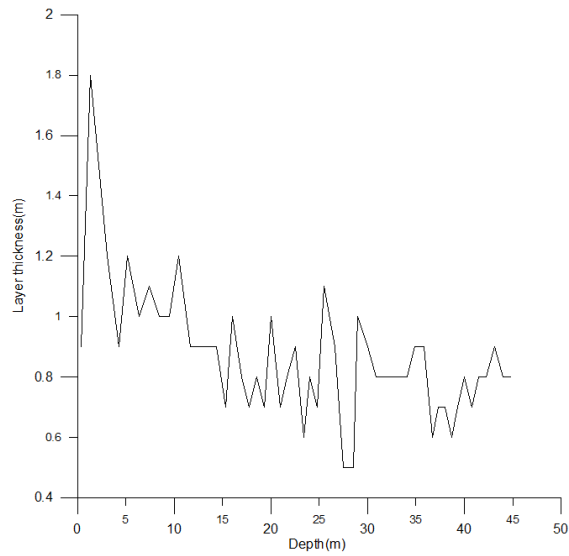


Figure 4.12: Annual layer thickness versus depth for the first 45m of the South Dome ice core.

Chapter 5 Discussion

In this chapter the results of the experiments described in Chapter 4 are discussed and furthermore the two conductivity instruments – “the old” Model 382 Series – and “the new” EDAQ C4D are compared. Additionally, the EDAQ C4D data is compared with data obtained by other detection methods of the CFA system. Furthermore the dust and conductivity data of the South Dome ice core are compared to dust and conductivity data from the NEGIS ice core.

5.1 Operation of the EDAQ C4D instrument

In the previous chapter, the results of experiments for testing the instrument were presented. In the first experiment the performance of the sample and reference circuits of the ET125 Headstage was shown in Figure 4.2 The response of the sample circuit when measuring the same conductivity standard solutions is similar to the response of the reference circuit in most cases shown in Figure 4.2 b), d) and e). In theory both outputs should be equal; the cause of the different response of two circuits could be that a different part of the tube was placed inside the circuit and between the electrodes to measure the conductivity of the solution. Whether the offset is due to different parts of the tube or due to some drift of the reference circuit is not clear, and further experiments should be performed to clarify this issue. However, for all the other experiments performed, only the sample circuit was used. Therefore, if there is any difference between the two circuits, it does not affect the results.

Moreover, the response of the sample circuit was tested for the same conductivity standards but for different tube types. The tubes are of two different types of plastic, PEEK and PFA, and of three different internal diameter sizes. As mentioned in Chapter 3, the response of the circuit depends on the cell and stray capacitances, C and C_o respectively, which are fixed by the manufacturer, and also on the circuit resistance R . The resistance depends on the conductivity of the solution and on tubing length and cross-sectional area. The length of the tube cannot have an important effect, as all tubes are long enough to go through the metal box where the headstage is placed, and also the length of the circuit is equal to the distance between the electrodes (20mm), which is constant and many times smaller than the length of the tubes. Finally, the tubing attribute left to affect the measurement is its cross sectional area, which depends on the tube diameter. The tubes are of the same outer diameter but of different internal diameters. As the internal diameter gets bigger, there is more space for the liquid to pass through, there is less pressure applied to it by the tube’s walls, and therefore the resistance of the sample decreases. The opposite occurs, as the internal diameter decreases. In Figure 4.3 we see that as the conductivity of the solution decreases, the response of the instrument decreases as well and that all the tubes have similar response patterns, except for the black tube, whose pattern is unique. The response of the

instrument gets higher as the internal diameter increases, which is reasonable because the resistance of the circuit decreases, causing the current and conductance of the sample to decrease.

In Figure 4.3 e) and f) we see the response of the black tube. For this tube the stable frequency range is wider than any other tubes. However, its responses for different conductivities overlap. That is why a second part of the tube was tested, with the hope that some internal deficiency of this single part caused this effect. But the second test showed overlapping as well, so this particular tube is not considered suitable to keep working with. Another thing to notice in this figure is that the difference in voltage response for the two parts of the same tube is big, and it can indeed have an effect on the response of the instrument.

In Figure 4.4, we see the response of the instrument to different tubes for a specific conductivity solution. The green tube of I.D. = 0.03'' is made of PEEK, while the clear tube of the same size I.D. is made of PFA, therefore, we can compare the material effect to the response. Furthermore, the two clear tubes are made of PFA but have different I.D.; thus by comparing them, we compare the effect of the I.D.'s size to the instrument's response. From Figure 4.4 a) and b), there is a difference in response between them as far as the amplitude of the output voltage is concerned. The amplitude is decreasing as the I.D. is decreasing, which is reasonable because the resistance of the sample is increasing. Moreover, between the tubes with I.D. = 0,03'', the green tube made of PFA, has a slightly bigger response from both. As it was mentioned in Chapter 4, the tube is made of PEEK plastic, with some metals added to it, in order to acquire its special green color. The slightly different response, could originate from the different materials.

When we compare the difference in the voltage response between the two clear tubes with different I.D. or between the green and brown tubes, which are made of the same type of plastic but have different I.D., we see that the importance of the I.D. of the tube. The difference between the 0.03'' and 0.04'' I.D. is larger than the difference in response between the 0.03'' and 0.02''. That is reasonable as the cross-sectional area of the circuit increases proportional to the square of the internal radius of the tube.

The wide maximum range of the voltage response starts in 29-48kHz for C_2 for all tubes, and is decreasing as conductivity is decreasing, to 13-19kHz for C_4 , C_3 and C_5 for all tubes (except for green, whose range is in the lower range of 8-13kHz), and finally for C_6 to 8-13 kHz (except for the brown tube which goes to 5-8kHz). Apparently, as the conductivity decreases, so does the wide maximum frequency range. It shifts to lower frequencies, which corresponds to the low conductivity signal being detected.

The wide maximum range described so far, is for discrete measurements. However, when the instrument is set to perform continuous measurements, it is necessary that we set the frequency of the measurement. For this reason we need to know the frequency that gives a linear response between the conductivity value of the sample and the voltage output of the instrument. According to Figure 4.5, a proper frequency is $f = 19219\text{Hz}$, and this specific result is related to the instrument's technical features.

The comparison of the time response between the EDAQ C4D and the Model 382 Series for sodium, calcium and PH standard solutions, showed that the former is 3-9 sec faster than the latter, but the comparison when both instruments were measuring conductivity independently, showed that the EDAQ C4D is faster.

During the experiments, the temperature of the environment was approximately stable to 19°C and therefore was assumed to be the temperature of the liquid solutions during the measurements. However, there was no control of the temperature for the solutions to see if their temperature during the measurements was indeed stable, thus to examine if any variation of the temperature can affect the measurements. Consequently for now, we cannot have more information about the temperature effect.

5.2 Comparison of the Two Instruments

In this section, we compare the measurements of the two instruments, EDAQ C4D and Model 382 Series for measuring the conductivity of the water from melting the 45m South Dome ice core. For this purpose, we plot the data acquired, by calculating the average and standard deviation of the voltage and conductivity output of the two instruments, for a space interval of 10cm. This space step is good enough to remove the instrumental noise, and at the same time to keep the signal of the measurement. In Figure 5.1 we see that the voltage measured from EDAQ C4D is linearly related to the conductivity measured from Model 382 Series, and that the bulk of data matches with this line.

Furthermore, we may notice that the linear fit corresponds to the majority of the data but there is some deviation from linearity for very low (below 0.1V) and very high (above 0.5V) conductivity values. Specifically, for the 0.1 to 0.5V and 0.8 to 5 μ S/cm interval, the connection between voltage and conductivity is linear. However, it deviates to the right, when it comes to higher conductivity values. Moreover, we see that below approximately 0.1V there is a deviation from linearity as well. Consequently, it seems that the new instrument EDAQ C4D performs linearly in the interval 0.1-0.5V. Nevertheless, for the majority of high and low conductivity values, their standard deviation coincides with the linear fit. This is similar to what we see for discrete measurements, for example in Figure 4.1 b), for voltage above 1V the response of the instrument does not distinguish between the different conductivity values. This means that there is an upper limit for the instrument to detect conductivity.

Another thing is that the large standard deviation of some of the measurements on both axis indicates a steep peak of the voltage/conductivity signals within a small depth interval. In Figure 5.2, we see voltage versus conductivity for depth range of 10m. We see that for all four cases the

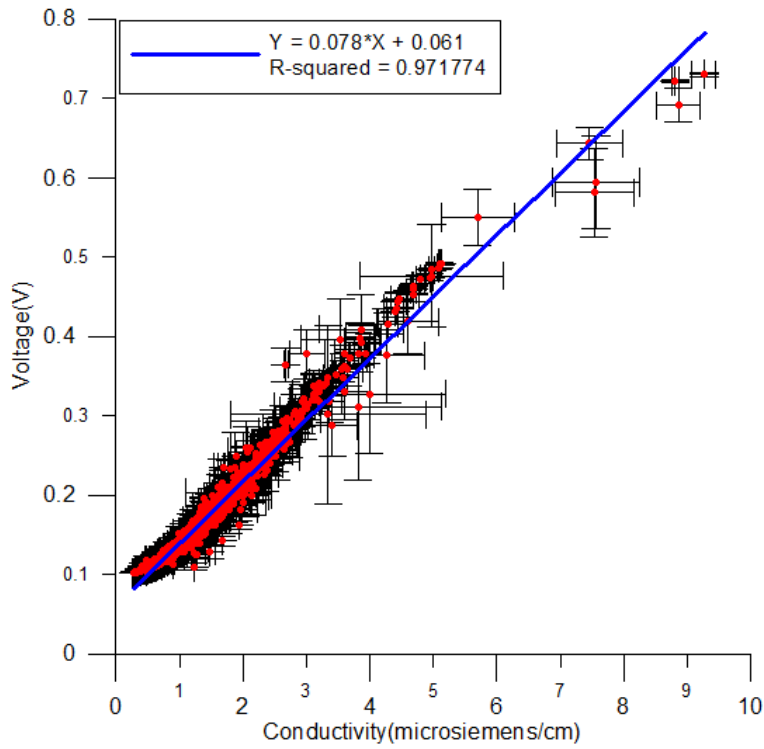
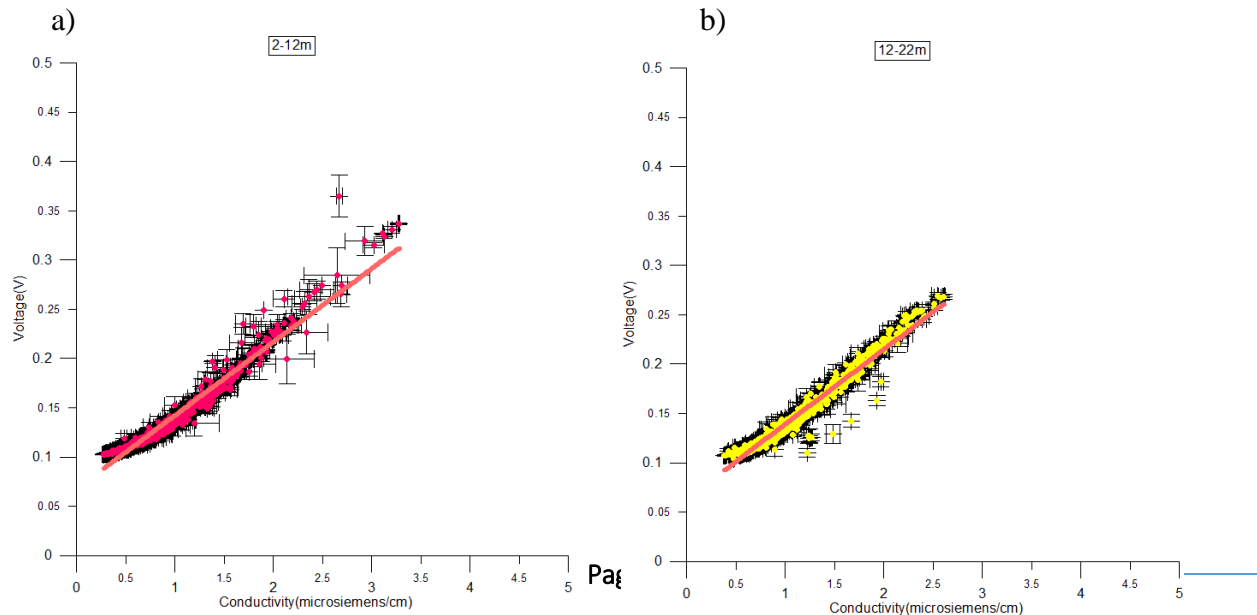


Figure 5.1: Voltage versus conductivity for the South Dome melted ice core and 10cm resolution; voltage measured from EDAQ C4D and conductivity measured from Model 382 Series.

majority of data lies between 0.1V and 0.4V and that for values above and beneath there is deviation from linearity.



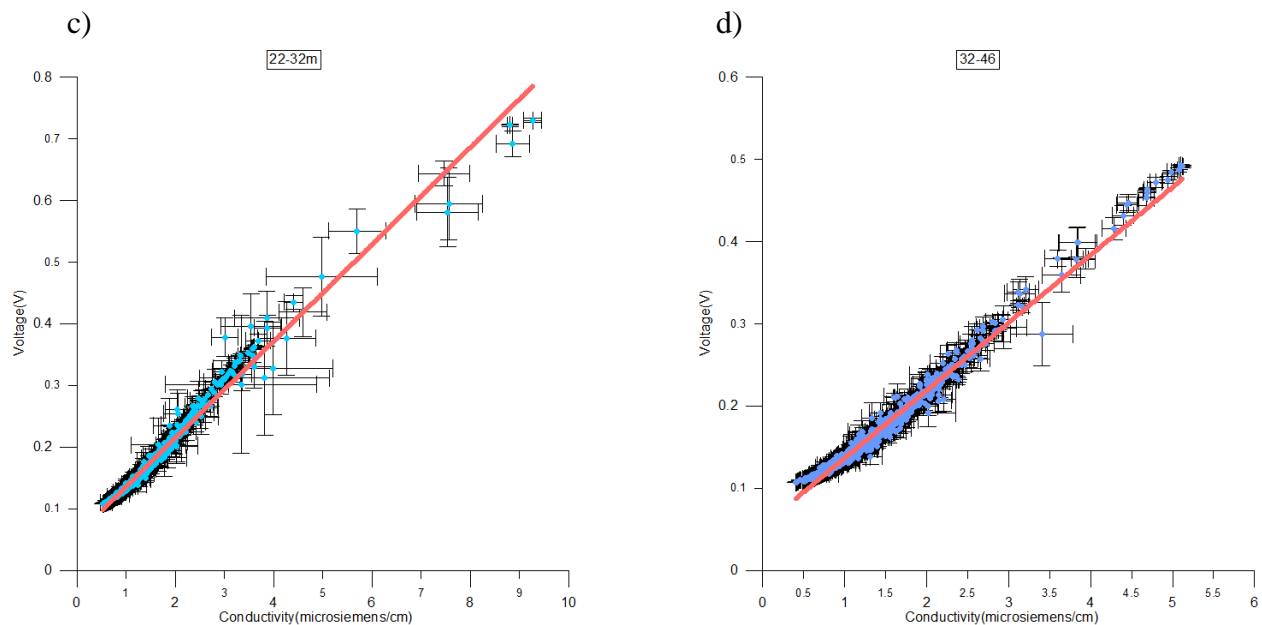


Figure 5.2: Voltage versus conductivity for the South Dome melted ice core for a)2-12m, b)12-22m, c)22-32m, and d)32-46m.

5.3 Comparison of the EDAQ C4D data with data of other detection methods of the CFA system

In this section we compare the voltage response of the instrument EDAQ C4D with the concentrations of some impurities found in the ice core. These are traditionally detected by other detection methods of the CFA system. The dust is detected in the Dust detector, calcium was detected by fluorescence, sodium and hydrogen cations were detected by the absorption detection method. In Figure 5.3, we show this comparison in 10cm resolution. In Figure 5.3 a) we have the voltage versus calcium concentration. We see that the response of the instrument to calcium is not linear, as the bulk of the data do not correspond with the linear fit. Therefore it is recommended that the instrument should not be used for measuring calcium. Similarly for 5.3 b) and c), the linear fits do not align with the majority of the data. Consequently, the instrument responds to the

presence of these ions (for dust is charged particles) but does not respond efficiently to changes in their concentration. Therefore it cannot distinguish between them.

Figure 5.3 d) shows the response of the instrument to hydrogen cations, whose concentration is indicative of the acidity of water. In this case, there is some correlation between voltage and the concentration of hydrogen cations. The value of the coefficient of determination – R^2 indicates that approximately half of the data points fit to the line. However, this is not a good enough correlation to consider using the instrument to measure hydrogen cations concentration.

Despite the fact that the last correlation mentioned is not good enough for linearity, it is many times larger than the correlation between calcium - voltage and sodium - voltage. This is due to the high electrophoretic mobility of the hydrogen cations, which is very high as the hydrogen cation has the smallest radius, and the charge to radius ratio gets large, thus hydrogen cations contribute more to conductivity than other ionic species (Kalantar-zadeh, 2013).

In Figure 5.4 is conductivity and all the other concentrations measured during the melting of the ice core are plotted versus voltage in pairs of two. The purpose of this figure is to compare the voltage ranges that correspond to these measurements, which refer to conductivity and concentration of different substances. Interestingly, the bulk of the measurements lies within the range 0.1-0.5V. This is the range of the linear relation between the conductivity and voltage. It seems that above this range the instrument gradually reaches a saturation level. Finally, in Figure 5.3 a), b), c) and d) and 5.4 a), b) and c) are some data in the x-axis of concentration that have negative values. Such negative values in concentration are caused by interference of air bubbles with the instrument of the measurement. However, their number is much smaller than the total amount of data, therefore they do not affect the result.

Finally, we investigate the case that the small deviation from linearity for conductivity and hydrogen cation measurements, emanates from interference of other ions. For this purpose we calculate the voltage value according to the equation of the linear regression in Figure 5.3 d), and we name this value $V_{\text{theoretical}}$, while the respective measured voltage is called V_{measured} . Their absolute difference and error are estimated for each V_{measured} and these differences are plot for each concentration measured. We can see the result in Figure 5.5. We may notice that the correlation between the voltage difference and the concentration of a) dust, b) calcium, c) sodium is very small and therefore none of these ions seem to contribute to the deviation from linearity.

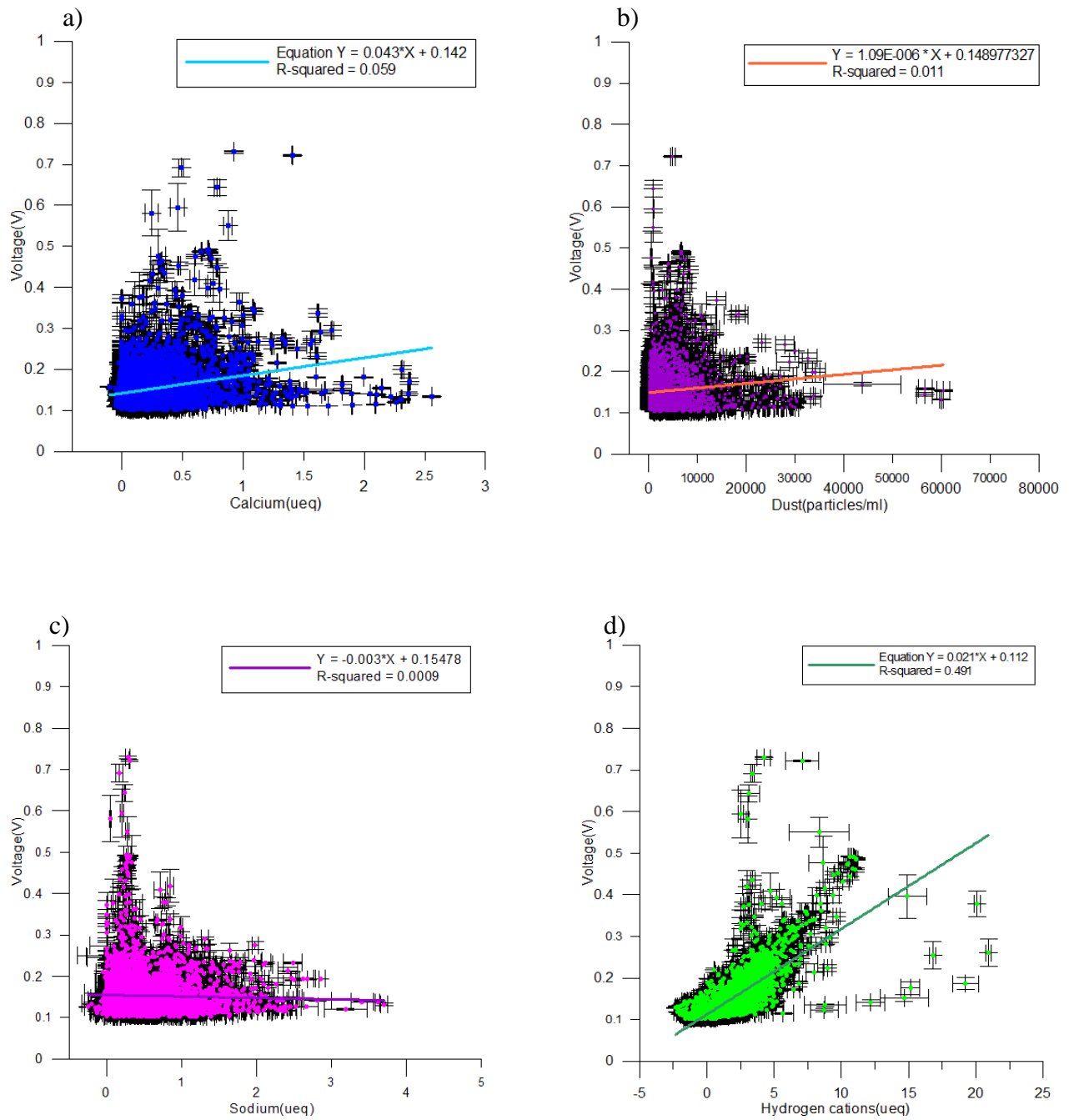


Figure 5.3: The voltage response of the instrument for different ions species and dust, incorporated into the ice core; a)calcium, b)dust, c) sodium, d) hydrogen cation.

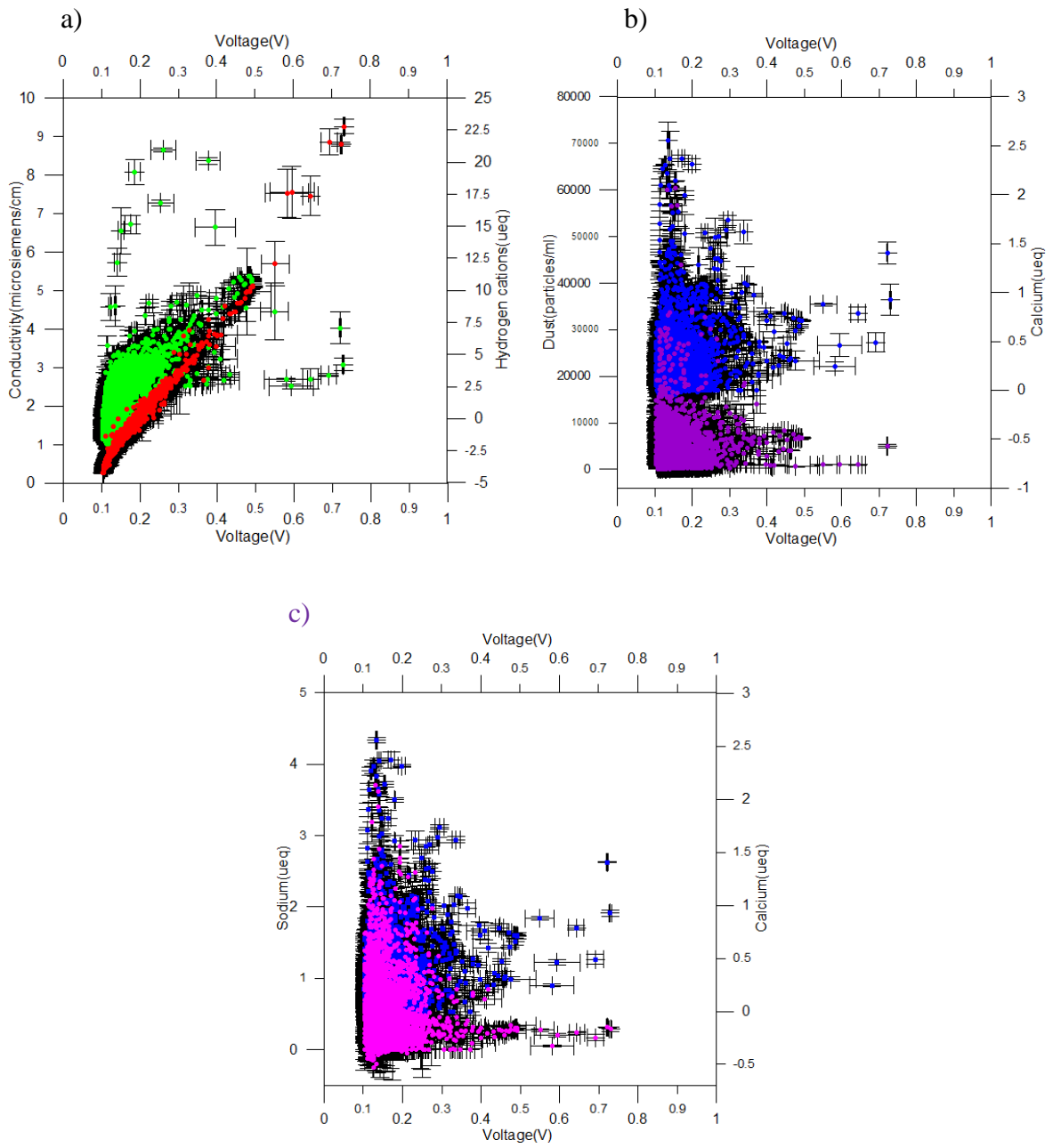


Figure 5.4 a)conductivity and hydrogen cation concentration versus the voltage response, b)dust and calcium concentration versus voltage, and c)sodium and calcium concentration versus voltage.

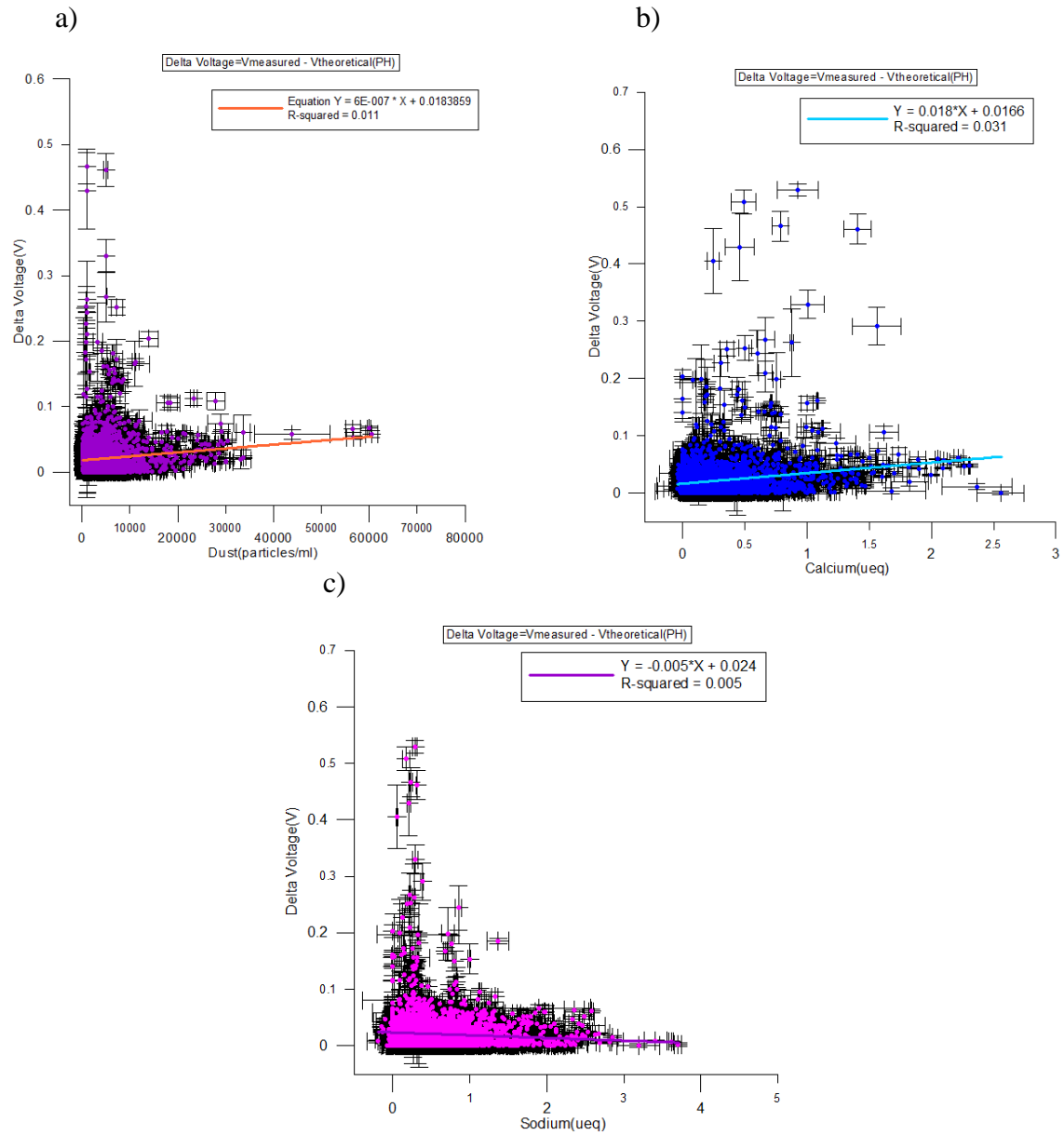


Figure 5.6: Voltage difference for hydrogen cations versus a) dust, b) calcium, c) sodium.

5.4 Comparison of the South Dome and NEGIS Shallow Ice Cores

In this section we refer to two shallow ice cores extracted from the Greenland Ice Sheet. The first is the 67-meter long NEGIS ice core, which was drilled at a site representative of the Northeast Greenland Ice Stream (NEGIS, 75°37.61'N, 35°56.49'W) (Vallelonga et al., 2014). The second is a 45-m long shallow core, which was drilled at South Dome (63°32'N, 44°34'W), as part of a campaign aiming to study snow and firn in Southern Greenland (Freitag et al., 2014).

In Figure 5.7, the profiles of phosphate, dust and conductivity are shown for the upper part of the NEGIS ice core, which covers the time interval 1930-2005yr AD, for 1cm resolution (Kjær et al., 2013). In Figure 5.8, the profiles for conductivity and dust, are shown for the South Dome ice core, which covers the time interval 1959-2010yr AD, for 1mm resolution.

We can see that for dust concentration the bulk of data lies within the range (0-10⁴) particles/ml, (the unit counts/ml is equal to particles/ml), in both ice cores. However, some dust peaks are more pronounced in the South Dome ice core, and others in the NEGIS. For example, the dust peak after the year 1990, is approximately 3 times higher in NEGIS than in South Dome. Conversely, shortly

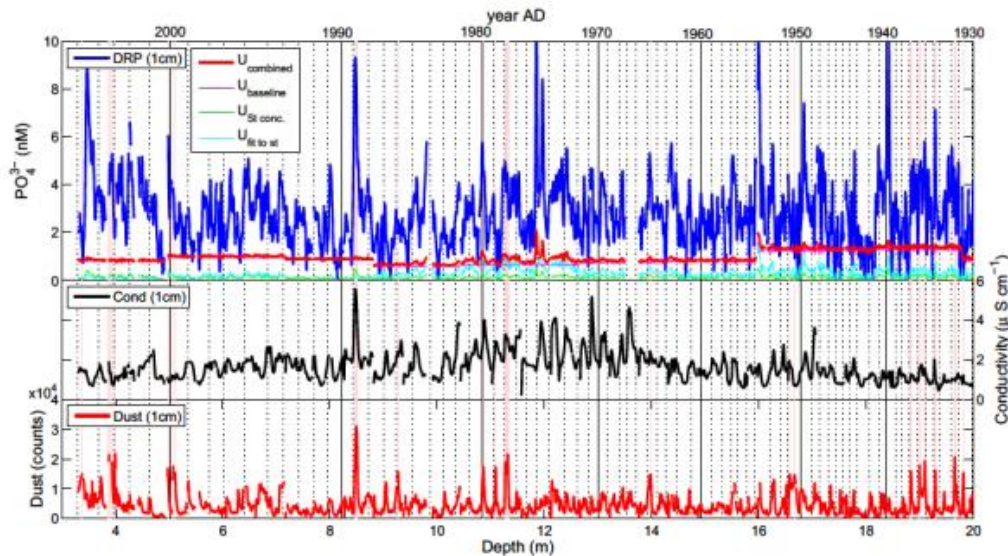


Figure 5.7: Phosphate, conductivity and dust profiles for the upper section of the NEGIS ice core (Kjær et al., 2013).

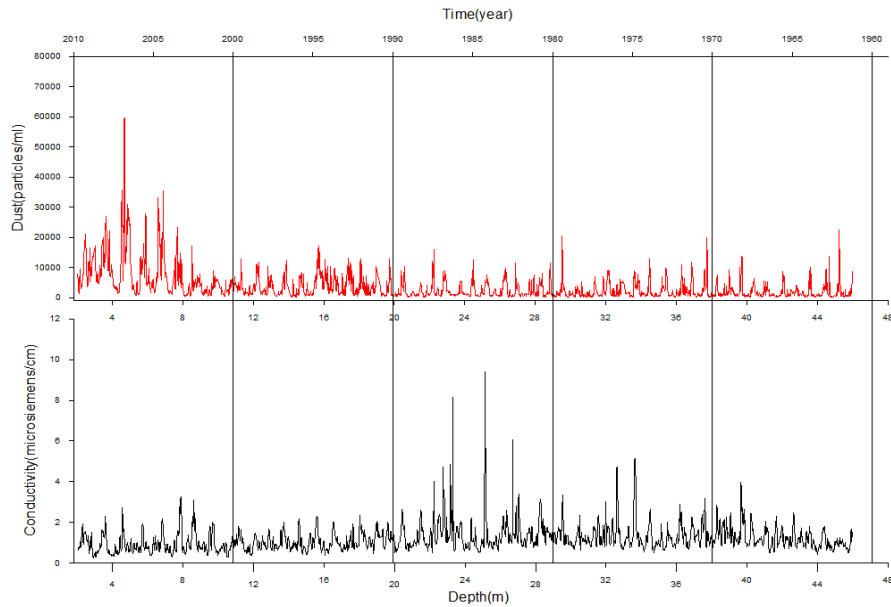


Figure 5.8 Dust and voltage profile for the South Dome ice core.

before year 1970, there is a dust spike in South Dome, approximately double in size of the dust spikes in NEGIS, for the same time interval. Similarly for conductivity, the bulk of measurements is within the range (0-2) μ S/cm, however there are some conductivity spikes that are more pronounced in one record. For example, in the 1980-1990 decade, there are some conductivity spikes that reach 8 μ S/cm for South Dome, while for NEGIS the corresponding peak is of half range.

These differences in dust concentration and conductivity, could be due to the different geographical areas of Greenland, that each of these ice cores originates. The NEGIS ice core was extracted from the northern part of Greenland, while the South Dome ice core, from the southeast. Precipitation in Greenland, is the result of interaction between cyclonic forcing, topography and onshore flow, thus the precipitation distribution over Greenland differs from place to place. Maximum precipitation falls on the southeast coast, while minimum precipitation falls on the central northern part of Greenland (Schuenemann et al., 2009). The deposition of aerosols to ice depends on the precipitation patterns, which are not the same over Greenland. These different precipitation patterns, can cause interannual variability between the species examined, in ice core records taken from different sites (Hutterli et al., 2007), and may have caused the differences on the concentration of dust and conductivity for certain years.

Another interesting thing to notice, is the different time intervals that each ice core covers. The NEGIS ice core covers a time interval of approximately 400 years, while the South Dome ice core, covers a time interval of about 50 years. This should result from the fact that they are composed of annual layers of different thicknesses. The mean annual layer thickness for NEGIS firm core is approximately 0.1m (Vallelonga et al., 2014), while for South Dome is approximately 0.9m

(Figure 4.12). Again, the annual layer thickness depends on the annual precipitation. In the northern part of Greenland, the precipitation rates are very low, of the order of 10cm (Schuenemann et al., 2009). The annual precipitation rate for the Southern part is above 165cm. Larger volumes of precipitation result in thicker annual layers of the ice sheet locally.

Another thing to notice relative to the conductivity of the South Dome ice core is the two outstanding peaks during the 1980-1990years. They are 4-5 times larger than the mean conductivity range of the majority of data. The conductivity is the sum of the ionic species that are contained in the ice, and expresses the deviation of the ice from being pure, without impurity content. Volcanic eruptions emit big amounts of gases and aerosols into the atmosphere, especially in the form of sulphuric acid, carbon dioxide and others. This big amount of impurities injected into the atmosphere are deposited onto the surface, producing a high conductivity signal on the surface of the ice sheet. The surface will gradually shift deeper into the ice sheet, as new annual layers will be added above it, on the longterm. This high conductivity signal may be compared with the sulphate signal of the ice core, along with the profile of the hydrogen cations, to confirm that the peak in conductivity is indeed a signal of volcanic eruption. Another method that can be applied independently or complementarily, is to compare the conductivity measurements of the melted water, with conductivity measurements performed directly on ice, for example via the ECM method. Volcanic eruptions are spectacular and can have a great impact on human's life. This is the reason why historic sources often refer to volcanic eruptions of their time. The historic records are very important for climate scientists. When the time of a volcano eruption is known, its signal on an ice core can be identified and become a reference horizon, which may be used to date the ice core, or even to synchronize different ice cores that contain the same volcanic signal (Svensson et al., 2013). In Figure 5.8, conductivity and hydrogen cations in 10cm resolution with respect to depth are plotted, the black lines indicate high peaks in conductivity and hydrogen cations that correspond to the same depth, thus belong to the same annual layer. It is possible that their source is volcanic eruptions, however this record should be compared with sulphate concentration and other conductivity measurements for further confirmation.

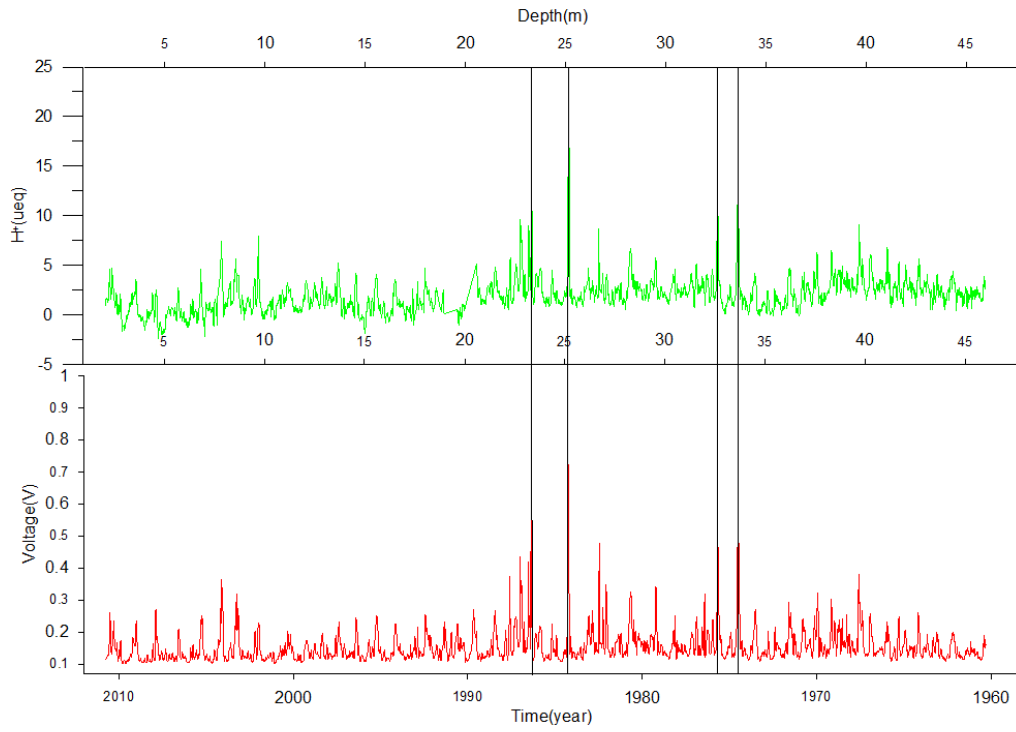


Figure 5.8 Dust and voltage profile for the South Dome ice core.

Chapter 6 Conclusions and Outlook

During this project, the contactless conductivity instrument EDAQ C4D was tested, and used to measure the conductivity in the first 45m of the South Dome Ice Core.

At first, the performance of the instrument was tested for discrete measurements of conductivity standards in the range of the conductivity values typically found in the ice cores. The response of the instrument revealed a high peak matching with the 859kHz frequency and a broad maximum, whose location depends on the value of conductivity measured, and the type of tube used. The wide range maximum lies in the interval 8-48kHz and shifts towards the lower frequencies as the value of conductivity decreases.

The sample and reference circuits were tested by comparing their response to the conductivity standards. In 3 out of 5 cases examined, their response is equal, as it is predicted from the theory, and in other 2 cases there is some offset. Although the experiments were performed under the same circumstances, it is possible that a different part of the same tube was used, which might have influenced the result.

The same conductivity standards and for 5 different types of tubes were tested. The tubes were different in the construction material: PEEK and PFA; and in three different sizes of the internal diameter: 0.02'', 0.03'', and 0.04''. The most important factor is the size of the internal diameter, as it directly affects the resistance and thus the current flowing in the circuit. When the internal diameter increases, the pressure applied to the sample liquid decreases and the resistance decreases, as there is more space for the water sample to pass through. Therefore, the response of the instrument gets higher as the internal diameter increases, and the difference in response between the 0.03'' and 0.04'' I.D. is larger than the difference between the 0.03'' and 0.02''. That is reasonable as the cross-sectional area of the circuit increases proportional to the square of the internal radius of the tube.

The wide maximum range lies between 29-48kHz for high conductivity values and 8-13 kHz for low conductivity values, for most cases examined. The frequencies within this range, are the ideal frequencies for the instrument to measure, in discrete measurements, as within this range, it exhibits the greater stability and sensitivity for conductivity detection.

For continuous measurements, it is necessary that we set the instrument to measure in the frequency where there is a linear response to voltage for conductivity, and according to Figure 4.5 a proper frequency is $f = 19219\text{Hz}$ for clear PFA tube of I.D. = 0.03''. Therefore, we set the EDAQ C4D to measure the conductivity of the South Dome ice core in this frequency, and with this tube.

The comparison of the time response between the EDAQ C4D and the Model 382 Series for sodium, calcium and PH standard solutions, shows that the former is 3-9 sec faster than the latter.

The comparison of the measurements of the two instruments, EDAQ C4D and Model 382 Series for measuring the conductivity of the water from melting 44m of the South Dome ice core, in a 10cm resolution, shows that for the majority of the data there is a linear relation of high correlation, which however seems to deviate above 0.5V. This upper limit is apparent in the discrete measurements too.

Furthermore, the comparison of the measurement to data obtained from other measuring techniques of the CFA system, shows that it corresponds to the presence of specific ions, but not in a linear way, and therefore it is not recommended to be used to measure their concentration.

Moreover, we investigate the case that the small deviation from linearity for hydrogen cations and voltage measurements, mentioned before, emanates from interference of other ions. The correlation estimated between the deviation from linearity and the concentration of the ions measured signifies that these ions do not cause any deviation from linearity. Therefore, it can be concluded that the deviation from linearity could be attributed to the highest electrophoretic mobility that each hydrogen ion exhibits.

Finally, the dust and conductivity data obtained from the shallow South Dome ice core are compared to the dust and conductivity data obtained from the upper part of the NEGIS shallow ice core. For dust and conductivity the bulk of data lies within a certain for both ice cores. However, some dust peaks are more pronounced in the South Dome ice core, and others in the NEGIS. Similarly for conductivity. These differences could be due attributed to the different geographical areas of origination of the ice cores. The NEGIS ice core was extracted from the northern part of Greenland, where the annual precipitation is low, while the South Dome ice core from the southeast, where the annual precipitation is high. These different precipitation patterns, can cause interannual variability between the species examined, in ice core records taken from different sites (Hutterli et al., 2007), and may have caused the differences on the concentration of dust and conductivity for certain years.

The conductivity of the South Dome ice core has two outstanding peaks during the 1980-1990years. They are 4-5 times larger than the mean conductivity range of the majority of data, which match to hydrogen cations peaks recorded for the same years. They are possible volcano signals, however, comparison with sulphate or other conductivity detection methods is recommended for further confirmation.

6.1 Future Work

It would be very interesting to study how changes in temperature of the sample affects the measurements of the instrument. From theory, we know that the conductivity of a solution depends on temperature, as the mobility of the ions intensifies when the temperature rises. It would be interesting to study how the temperature variations affect the response of the instrument, and whether they have any effect on its linear range.

Furthermore, it would be interesting to re-test the response of the sample and reference circuit, using the same part of the tube this time. That would allow us to investigate whether further the cause of the offset appeared in some study cases of this project.

Finally, it would also be interesting to compare the instrument with other ionic concentrations, such as sulfate, whose high concentrations are often connected to volcanic eruptions which are usually spotted as high values in conductivity as well.

References

Abbott, Peter M., Siwan M. Davies, Jørgen Peder Steffensen, Nicholas JG Pearce, Matthias Bigler, Sigfus J. Johnsen, Inger K. Seierstad, Anders Svensson, and Stefan Wastegård. "A detailed framework of Marine Isotope Stages 4 and 5 volcanic events recorded in two Greenland ice-cores." *Quaternary Science Reviews* 36 (2012): 59-77.

Alonso, Marcelo, and Edward J. Finn. *Fundamental university physics*. Reading, MA: Addison-Wesley, 1967.

Andersen, Katrine K., Anders Svensson, Sigfus J. Johnsen, Sune O. Rasmussen, Matthias Bigler, Regine Röthlisberger, Urs Ruth et al. "The Greenland ice core chronology 2005, 15–42ka. Part 1: constructing the time scale." *Quaternary Science Reviews* 25, no. 23 (2006): 3246-3257.

Bagotsky, Vladimir S., ed. *Fundamentals of electrochemistry*. Vol. 44. John Wiley & Sons, 2005.

Baltussen, Erik, Rosanne M. Guijt, Gert van der Steen, Frederic Laugere, Sander Baltussen, and Gijis WK Van Dedem. "Considerations on contactless conductivity detection in capillary electrophoresis." *Electrophoresis* 23, no. 17 (2002): 2888-2893.

Behera, Sailesh, N. Sharma, Mukesh Aneja, and Viney Balasubramanian. "Ammonia in the Atmosphere: A Review on Emission Sources, Atmospheric Chemistry and Deposition on Terrestrial Bodies." *Environmental Science and Pollution Research* 20, no. 11 (2013): 8092-131.

Bertler, Nancy, Paul Andrew Mayewski, Alberto Aristarain, P. Barrett, S. Becagli, R. Bernardo, S. Bo et al. "Snow chemistry across Antarctica." *Annals of Glaciology* 41, no. 1 (2005): 167-179.

Bigler, Matthias, Anders Svensson, Ernesto Kettner, Paul Vallelonga, Maibritt E. Nielsen, and Jørgen Peder Steffensen. "Optimization of high-resolution continuous flow analysis for transient climate signals in ice cores." *Environmental science & technology* 45, no. 10 (2011): 4483-4489.

Boutron, Claude F., Jean-Pierre Candelone, and Sungmin Hong. "Greenland snow and ice cores: unique archives of large-scale pollution of the troposphere of the Northern Hemisphere by lead and other heavy metals." *Science of the total environment* 160 (1995): 233-241.

Bradley, Raymond S. (2014). *Paleoclimatology: Reconstructing Climates of the Quaternary: Third Edition*. Elsevier.

Breton, Daniel J., Bess G. Koffman, Andrei V. Kurbatov, Karl J. Kreutz, and Gordon S. Hamilton. "Quantifying signal dispersion in a hybrid ice core melting system." *Environmental science & technology* 46, no. 21 (2012): 11922-11928.

Brito-Neto, José Geraldo Alves, José Alberto Fracassi da Silva, Lucas Blanes, and Claudimir Lucio do Lago. "Understanding capacitively coupled contactless conductivity detection in

capillary and microchip electrophoresis. Part 1. Fundamentals." *Electroanalysis* 17, no. 13 (2005): 1198-1206.

Caloz, Gabriel, Monique Dauge, Erwan Faou, and Victor Péron. "On the influence of the geometry on skin effect in electromagnetism." *Computer Methods in Applied Mechanics and Engineering* 200, no. 9 (2011): 1053-1068.

Dansgaard, Willi. "Stable isotopes in precipitation." *Tellus* 16, no. 4 (1964): 436-468.

Divine, Dmitry, Elisabeth Isaksson, Tonu Martma, Harro AJ Meijer, John Moore, Veijo Pohjola, Roderik SW van de Wal, and Fred Godtlibsen. "Thousand years of winter surface air temperature variations in Svalbard and northern Norway reconstructed from ice core data." *Polar Research* 30 (2011).

Fischer, Hubertus, Marie-Louise Siggaard-Andersen, Urs Ruth, Regine Röthlisberger, and Eric Wolff. "Glacial/interglacial changes in mineral dust and sea-salt records in polar ice cores: Sources, transport, and deposition." *Reviews of Geophysics* 45, no. 1 (2007).

Freitag, Johannes, Sepp Kipfstuhl, Sebastian Hoerz, Lukas Eling, Bo Vinther, and Trevor Popp. "Melt layer statistic of two firn cores recently drilled at Dye3 and South dome in the dry snow zone of Southern Greenland." In *EGU General Assembly Conference Abstracts*, vol. 16, p. 10770. 2014.

Fuhrer, Katrin, Albrecht Neftel, Martin Anklin, Thomas Staffelbach, and Michel Legrand. "High-resolution ammonium ice core record covering a complete glacial-interglacial cycle." *Journal of Geophysical Research: Atmospheres (1984–2012)* 101, no. D2 (1996): 4147-4164.

Genthon, C. "Simulations of desert dust and sea-salt aerosols in Antarctica with a general circulation model of the atmosphere." *Tellus B* 44, no. 4 (1992): 371-389.

Gow, Anthony J. "Electrolytic conductivity of snow and glacier ice from Antarctica and Greenland." *Journal of Geophysical Research* 73, no. 12 (1968): 3643-3649.

Gray, James R. "Conductivity analyzers and their application." *Environmental instrumentation and analysis handbook* (2005): 491-510.

Hutterli, Manuel A., T. Crueger, Hubertus Fischer, Katrine K. Andersen, C. C. Raible, Thomas F. Stocker, Marie-Louise Siggaard-Andersen, J. R. McConnell, R. C. Bales, and J. F. Burkhart. "The influence of regional circulation patterns on wet and dry mineral dust and sea salt deposition over Greenland." *Climate dynamics* 28, no. 6 (2007): 635-647.

IPCC 2013, Climate Change 2013: *The Physical Science Basis*, Chapter 5, Information from Paleoclimate Archives.

Kalantar-zadeh, K. (2013). *Sensors an introductory course*. New York: Springer.

Kaufmann, Patrik R., Urs Federer, Manuel A. Hutterli, Matthias Bigler, Simon Schüpbach, Urs Ruth, Jochen Schmitt, and Thomas F. Stocker. "An improved continuous flow analysis system for high-resolution field measurements on ice cores." *Environmental science & technology* 42, no. 21 (2008): 8044-8050.

Kreutz, K. J., and Koffman B. G. "Glaciochemistry" *The Encyclopedia of Quaternary Science*, no. 2(2013): 326-333.

Kjær Helle A. "Phosphate in Ice Cores-Finding a method for continuous detection of phosphate in ice cores." *Master thesis*, (2010), Center for Ice and Climate, University of Copenhagen.

Kjær Helle A. "Continuous chemistry in ice cores-Phosphorus, pH and the photolysis of humic like substances." *PhD Thesis*, (2014), Center for Ice and Climate, University of Copenhagen.

Kjær, Helle Astrid, Paul Vallelonga, Anders Svensson, Magnus Elleskov L. Kristensen, Catalin Tibuleac, and Matthias Bigler. "Continuous flow analysis method for determination of dissolved reactive phosphorus in ice cores." *Environmental science & technology* 47, no. 21 (2013): 12325-12332.

Kuramoto, Takayuki, Kumiko Goto-Azuma, Motohiro Hirabayashi, Takayuki Miyake, Hideaki Motoyama, Dorthe Dahl-Jensen, and Jørgen Peder Steffensen. "Seasonal variations of snow chemistry at NEEM, Greenland." *Annals of Glaciology* 52, no. 58 (2011): 193-200.

Kubáň, Pavel, and Peter C. Hauser. "Contactless conductivity detection in capillary electrophoresis: A review." *Electroanalysis* 16, no. 24 (2004): 2009-2021.

Lambert, Fabrice, Barbara Delmonte, Jean-Robert Petit, Matthias Bigler, Patrick R. Kaufmann, Manuel A. Hutterli, Thomas F. Stocker, Urs Ruth, Jørgen Peder Steffensen, and Valter Maggi. "Dust-climate couplings over the past 800,000 years from the EPICA Dome C ice core." *Nature* 452, no. 7187 (2008): 616-619.

Legrand, Michel, and Paul Mayewski. "Glaciochemistry of polar ice cores: a review." *Reviews of Geophysics* 35, no. 3 (1997): 219-243.

Lipták, Béla G., ed. *Instrument Engineers' Handbook, Volume Two: Process Control and Optimization*. Vol. 2. CRC press, 2005.

Lunt, Daniel J., and Paul J. Valdes. "Dust transport to Dome C, Antarctica, at the Last Glacial Maximum and present day." *Geophysical research letters* 28, no. 2 (2001): 295-298.

Mayewski, Paul A., Loren D. Meeker, Mark S. Twickler, Sallie Whitlow, Qinzhaoyang, W. Berry Lyons, and Michael Prentice. "Major features and forcing of high-latitude northern hemisphere atmospheric circulation using a 110,000-year-long glaciochemical series." *Journal of Geophysical Research: Oceans (1978–2012)* 102, no. C12 (1997): 26345-26366.

McConnell, Joseph R., Ross Edwards, Gregory L. Kok, Mark G. Flanner, Charles S. Zender, Eric S. Saltzman, J. Ryan Banta, Daniel R. Pasteris, Megan M. Carter, and Jonathan DW Kahl.

"20th-century industrial black carbon emissions altered arctic climate forcing." *Science* 317, no. 5843 (2007): 1381-1384.

Nielsen, Maibritt E., "Early Holocene and Eemian impurity profiles from the NGRIP ice core." *Master Thesis*, (2009), Center for Ice and Climate, University of Copenhagen.

Ohno, Hiroyuki, ed. *Electrochemical aspects of ionic liquids*. John Wiley & Sons, 2011.

Paterson, William Stanley Bryce, and Kurt M. Cuffey. *The physics of glaciers*. Vol. 3. Oxford: Pergamon, 1994.

Post, Austin, and Edward R. LaChapelle. *Glacier ice*. University of Toronto Press, 2000.

Rasmussen, Sune Olander, P. M. Abbott, Thomas Blunier, A. J. Bourne, E. Brook, Susanne Lilja Buchardt, C. Buizert et al. "A first chronology for the North Greenland Eemian Ice Drilling (NEEM) ice core." *Climate of the Past* 9, no. 6 (2013): 2713-2730.

Robock, Alan. "Volcanic eruptions and climate." *Reviews of Geophysics* 38, no. 2 (2000): 191-219.

Röthlisberger, Regine, Matthias Bigler, Manuel Hutterli, Stefan Sommer, Bernhard Stauffer, Hans G. Junghans, and Dietmar Wagenbach. "Technique for continuous high-resolution analysis of trace substances in firn and ice cores." *Environmental Science & Technology* 34, no. 2 (2000): 338-342.

Ruddiman, W. "Earth's climate, past and future." 2nd ed (2008). New York: *W.H. Freeman*.

Ruth, Urs, Dietmar Wagenbach, Matthias Bigler, Jørgen P. Steffensen, Regine Röthlisberger, and Heinz Miller. "High-resolution microparticle profiles at NorthGRIP, Greenland: case studies of the calcium-dust relationship." *Annals of Glaciology* 35, no. 1 (2002): 237-242.

Schuenemann, Keah C., John J. Cassano, and Joel Finnis. "Synoptic forcing of precipitation over Greenland: Climatology for 1961-99." *Journal of Hydrometeorology* 10, no. 1 (2009): 60-78.

Sigg, Andreas, and Albrecht Neftel. "Evidence for a 50% increase in H₂O₂ over the past 200 years from a Greenland ice core." (1991): 557-559.

Sigg, Andreas, Katrin Fuhrer, Martin Anklin, Thomas Staffelbach, and Daniel Zurmühle. "A continuous analysis technique for trace species in ice cores." *Environmental science & technology* 28, no. 2 (1994): 204-209.

Stillman, David E., Joseph A. MacGregor, and Robert E. Grimm. "The role of acids in electrical conduction through ice." *Journal of Geophysical Research: Earth Surface* 118, no. 1 (2013): 1-16.

Stojkovic, Marko. "Further development and applications of capillary electrophoresis with capacitively coupled contactless conductivity detection and sequential injection analysis in analytical chemistry." PhD diss., University of Basel, 2013.

- Svensson, Anders, Pierre E. Biscaye, and Francis E. Grousset. "Characterization of late glacial continental dust in the Greenland Ice Core Project ice core." *Journal of Geophysical Research: Atmospheres* (1984–2012)105, no. D4 (2000): 4637-4656.
- Svensson, Anders, Katrine Krogh Andersen, Matthias Bigler, Henrik Brink Clausen, Dorthe Dahl-Jensen, S. M. Davies, Sigfus Johann Johnsen et al. "A 60 000 year Greenland stratigraphic ice core chronology." *Climate of the Past*4, no. 1 (2008): 47-57.
- Svensson, Anders, Matthias Bigler, Thomas Blunier, Henrik Brink Clausen, Dorthe Dahl-Jensen, H. Fischer, S. Fujita et al. "Direct linking of Greenland and Antarctic ice cores at the Toba eruption (74 ka BP)." *Climate of the Past* 9, no. 2 (2013): 749-766.
- Taylor, Kenorick, Richard Alley, Joe Fiacco, Pieter Grootes, Gregg Lamorey, Paul Andrew Mayewski, and Mary Jo Spencer. "Ice-core dating and chemistry by direct-current electrical conductivity." *Journal of Glaciology* 38, no. 130 (1992): 325.
- Tournié, A., P. Ricciardi, and Ph Colombar. "Glass corrosion mechanisms: A multiscale analysis." *Solid State Ionics* 179, no. 38 (2008): 2142-2154.
- Vallelonga, P., K. Christianson, R. B. Alley, S. Anandakrishnan, J. E. M. Christian, D. Dahl-Jensen, V. Gkinis. "Initial results from geophysical surveys and shallow coring of the Northeast Greenland Ice Stream (NEGIS)." *The Cryosphere Discussions* 8 (2014): 691-719.
- Weng, Y., "Continuous Flow and Discrete Measurements of the Water Isotopes in an Firn Core from Greenland". Master thesis (2014). Niels Bohr Institute, University of Copenhagen.
- Wolff, Eric W., William D. Miners, John C. Moore, and Julian G. Paren. "Factors Controlling the Electrical Conductivity of Ice from the Polar Regions A Summary." *The Journal of Physical Chemistry B* 101, no. 32 (1997): 6090-6094.
- Zhang, Xiao-Ye, S. L. Gong, T. L. Zhao, R. Arimoto, Y. Q. Wang, and Z. J. Zhou. "Sources of Asian dust and role of climate change versus desertification in Asian dust emission." *Geophysical Research Letters* 30, no. 24 (2003).